Non-Neutron Transmutation of Spent Fuel

by

Charlotte I. Wickert

Submitted to the Department of Nuclear Science and Engineering
in partial fulfillment of the requirements for the degrees of

BACHELOR OF SCIENCE IN NUCLEAR SCIENCE AND ENGINEERING

and

MASTER OF SCIENCE IN NUCLEAR SCIENCE AND ENGINEERING

at the

MASSACHUSETTS INSTITUTE OF TECHNOLOGY

May 2024

Authored by: Charlotte I. Wickert
Department of Nuclear Science and Engineering
May 15, 2024

Certified by: Benoit Forget
KEPCO Professor of Nuclear Science and Engineering
Department Head, Thesis Supervisor

Accepted by: Ju Li
Professor of Nuclear Science and Engineering
Graduate Officer, Department of Nuclear Science and Engineering

Accepted by: Jacobo Buongiorno
Professor of Nuclear Science and Engineering
Undergraduate Officer, Department of Nuclear Science and Engineering

Non-Neutron Transmutation of Spent Fuel

by

Charlotte I. Wickert

Submitted to the Department of Nuclear Science and Engineering
on May 15, 2024 in partial fulfillment of the requirements for the degrees of

BACHELOR OF SCIENCE IN NUCLEAR SCIENCE AND ENGINEERING

and

MASTER OF SCIENCE IN NUCLEAR SCIENCE AND ENGINEERING

ABSTRACT

This thesis is a scoping study to assess the feasibility of utilizing non-neutron transmutation to target Long-Lived Fission Products (LLFPs), which account for 99% of the long-term radiotoxicity of spent nuclear fuel. With half-lives ranging from 100,000 to 10,000,000 years, LLFPs pose a significant obstacle to long-term high-level waste storage. Geologic repositories for nuclear waste must be functional for millions of years. This significant timescale contributes to the many technical and political challenges preventing the U.S. from closing the back end of the nuclear fuel cycle for High-Level Waste (HLW). The need for a geologic-time-scale repository could be reduced if the most active isotopes present in HLW could be identified and transmuted. While disposal would still be necessary, a smaller time scale could resolve some of the most significant concerns associated with the current million-year time scale.

Several computational methods, TALYS, TASMAN, PHITS, and FISPACT, are utilized to model the complete transport and transmutation process for proton irradiation to explore the potential of converting LLFP isotopes into stable or shorter-lived forms. TALYS is used to generate proton cross-sections for key LLFPs, as there are no differential cross section measurements in the energy range of interest (18-70 MeV). The uncertainty in the transmutation rate is calculated from the perturbed cross sections generated by TASMAN and TALYS in work supporting this thesis. The physics of the proton beam is modeled in supporting work using PHITS to provide a flux-energy spectrum and estimate the number of irradiated particles. Finally, FISPACT calculates the amount of depletion for each LLFP. A comparison of alpha and deuteron irradiation is performed using cross sections from the TENDL2021 library and SRIM to determine the penetration depth for each incident particle.

Preliminary findings indicate that longer irradiation times and higher beam energies enhance transmutation, resulting in a decreased long-term abundance of LLFPs compared to natural decay conditions. For commercial proton accelerators with a 10mA current operating continuously, the transmutation rates for LLFPs range from 0.59 +- 0.12 g/year to 7.51 +- 1.19 g/year. Most LLFPs are produced in a 1 GW (thermal) reactor on the order of 1kg/year. Therefore, the transmutation rates achievable with commercial accelerators are too low to make a significant impact. However, increasing the proton beam energy to take

advantage of proton spallation reactions may be successful, especially in the case of Selenium-79. 660g/year of Selenium-79 are produced in a 1 GW (thermal) reactor. Initial spallation estimates show that for Selenium-79, approximately 24 g/year could be transmuted with a single accelerator. Future work will focus on improving the spallation irradiation scheme and target design.

This work was supported by the DOE ARPA-E Project.

Thesis supervisor: Benoit Forget
Title: KEPCO Professor of Nuclear Science and Engineering
Department Head

Acknowledgments

First, I would like to thank my advisor, Professor Benoit Forget. I have been a Computational Reactor Physics Group member since my freshman fall, and I am so grateful for the experiences I've gained over the past five years under his guidance. I cannot wait to continue in the PhD program. Thank you to Dr. Amelia Trainer for being an incredible UROP mentor and inspiring me to pursue research.

Thank you to my friends in the NSE department for being such a supportive community. I cannot imagine MIT without you. Thank you to Heather and Brandy for always answering my questions and stocking the chateau with food and laughs; you truly make this department feel like a family.

Finally, I want to thank all my friends and family who supported me throughout this thesis process and in a million other ways. I will forever remember the cafe thesis work parties, late-night study sessions, spontaneous ice cream runs, rock climbing trips, competitive card games, movie nights, music jams, and so many other little moments that have made my time at MIT so incredible.

Contents

List of Figures

List of Tables

Chapter 1

Introduction

1.1 Motivation

There is currently no permanent operational solution to high-level waste (HLW) storage in the United States. This lack of a solution is a significant barrier to the wide-scale implementation of clean nuclear fission energy, as public opinion surrounding nuclear waste negatively affects nuclear power. Identification and substantial transmutation of the most significant fission products could reduce the disposal impacts of nuclear waste by eliminating the need for a geologic-time-scale repository in which nuclear waste must be stored for several hundred thousand to millions of years.

Work is currently being conducted to determine the optimal irradiation scheme to transmute Long-Lived Fission Products (LLFPs) using proton accelerators. LLFPs are byproducts of nuclear reactors that still pose radiotoxicity concerns after 1000 years. These include Selinium-79 (Se79), Zirconium-93 (Zr93), Technetium-99 (Tc99), Tin-126 (Sn126), Iodine-129 (I129), and Cesium-135 (Cs135). Contributions of each LLFP to the total radiotoxicity of spent fuel are shown in Table 1.1.

Table 1.1: Average Isotopic Contributions to Radiotoxicity after 1000 years in Each Evaluation Group Category[1].

	Tc-99	I-129	Sn-126	Zr-93	Cs-135	Se-79	Sum
Once-Through	42.6±15.0%	22.1±4.4%	14.1±9.4%	11.3±2.7%	7.9±4.9%	1.8±0.8%	99.7±0.3%
Limited-Recycle	46.3±4.7%	21.1±4.8%	11.9±4.7%	11.2±1.6%	7.3±3.5%	1.8±0.7%	99.6±0.2%
Continuous-Recycle	44.1±6.3%	22.8±2.1%	12.4±5.2%	9.2±2.1%	9.4±4.2%	1.6±0.7%	99.6±0.2%

Neutron irradiation of spent fuel in reactors has been considered in the past; however, using reactors to irradiate spent fuel creates more spent fuel in the process. Proton, deuteron, and alpha irradiation using proton cyclotrons are interesting options, as protons can be generated without harmful byproducts. Importantly, irradiating materials with protons produces neutrons, which could potentially provide secondary beneficial transmutation effects, offering a promising avenue for further exploration.

This thesis will consist of a computational evaluation of proton, deuteron , and alpha transmutation to determine the potential impact on a long-term nuclear repository.

1.2 Previous Work

After actinide recycling, 99% of long-term (>1000 years) radiotoxicity in a nuclear repository comes from Selinium-79, Zirconium-93, Technetium-99, Tin-126, Iodine-129, and Cesium-135. These Long-Lived Fission Products (LLFPs) were identified by analyzing fission products from the 40 comprehensive fuel cycle evaluation groups (EGs) in the multi-laboratory study "Nuclear Fuel Cycle Evaluation and Screening (E&S)" [1] funded by the DOE-NE's Fuel Cycle Options (FCO) Campaign. The six LLFPs have half-lives on the order of 100,000 years to 10,000,000 years (see Table 1.2).

Table 1.2: LLFP Half Lives

LLFP	Half-Life (Years)[2]
Se79	6.50×10^5
Zr93	1.53×10^6
Tc99	2.11×10^5
Sn126	1.00×10^5
I129	1.57×10^7
Cs135	2.30×10^6

Reducing the abundance of LLFPs through transmutation would significantly decrease the radiotoxicity of spent fuel repositories. Proton transmutation, in particular, may present an appealing solution. All the LLFPs produce stable or significantly shorter-lived isotopes when they capture protons. For example,

$$^{99}_{43}\mathrm{Tc}\,(\mathrm{p},\mathrm{n})\,^{99}_{44}\mathrm{Ru} \tag{1.1}$$

$$^{99}_{43}\mathrm{Tc}(\mathrm{p},2\mathrm{n})^{98}_{44}\mathrm{Ru}$$

produce stable isotopes of ruthenium (Eq. 1.1). Examples of additional favorable proton reactions are shown below in Table 1.3.

Previous transmutation work has primarily focused on the transmutation of fission products using neutrons[3]. Neutron-based transmutation systems for fission products require high neutron fluxes from fission reactions. Consequently, both the consumption and production of fission products happen simultaneously within this system, limiting the overall net transmutation rate of these fission products. Non-neutron methods could be more promising as they do not involve the production of additional fission products. Despite the potential, previous research into non-neutron transmutation has been scant due to limited facilities for generating high-energy non-neutron particles. However, recent advancements in photonics and ion accelerators make energetic non-neutron particles attainable at national lab user facilities or university accelerators. The effectiveness of these methods depends heavily on the energy and flux of incident particles, capture cross-sections, and the design of transmutation systems.

No experiments will be conducted as part of this thesis, but research is being conducted to evaluate the potential of eventually constructing a transmutation facility. The most

Table 1.3: Selected LLFP Proton Capture Reactions

Reaction	Half-Life of Results[2]
$^{79}_{34}$Se (p,n) $^{79}_{35}$Br	Stable
$^{93}_{40}$Zr (p,3n) $^{91}_{41}$Nb $\rightarrow$ $^{91}_{40}$Zr	680 Years, Stable
$^{99}_{43}$Tc (p,2n) $^{98}_{44}$Ru	Stable
$^{99}_{43}$Tc (p,n) $^{99}_{44}$Ru	Stable
$^{126}_{50}$Sn (p,4n) $^{123}_{51}$Sb	Stable
$^{129}_{53}$I (p,2n) $^{128}_{54}$Xe	Stable
$^{135}_{55}$Cs (p,2n) $^{134}_{56}$Ba	Stable

crucial aspect of this proposed facility is the method of producing protons. For this project, proton cyclotrons are being considered as they have the desired energy range and are already commercially available and, therefore, potentially cheaper. Cyclotrons produce protons with energies ranging from 9-70 MeV. Depending on the material, proton capture cross sections are significant, beginning around 9-18 MeV. Cyclotrons, therefore, produce protons at the most ideal energy for transmutation.

1.3 Objectives

Bound by the physical constraints of current commercial accelerator technologies, simulations of proton, alpha, and deuteron irradiation will be conducted at various energies, fluxes, and irradiation times to determine the optimal irradiation scheme for transmuting LLFPs. The effect of uncertainty in the cross sections on the eventual transmutation rate will also be quantified for the optimal scheme. This thesis will consider only nuclear reactions that contribute to transmutation. Future work will examine the impact of spallation reactions on LLFP transmutation rates.

1.4 Structure

The first section of this thesis will consist of an in-depth analysis of proton transmutation of the six LLFPs. For this analysis, extra care will be taken to ensure that the physics of the proton beam is captured correctly.

The second section will compare the transmutation potential of proton, alpha, and deuteron irradiation for each LLFP. For this analysis, only mono-energetic beams will be considered, and the penetration depth for each beam will be calculated separately.

Chapter 2

Background

2.1 Long Lived Fission Products (LLFPs)

The two components of high-level waste (HLW) produced in commercial reactors that contribute most to long-term radiotoxicity are actinides and LLFPs[4]. Assuming actinides are successfully separated from the spent fuel and recycling, LLFPs become the dominant source of radioactivity in HLW. All six LLFPs are water soluble[5] meaning if water were to reach the isotopes, they could travel through the ground. Separation and subsequent transmutation of these isotopes offers a method to decrease their impact on a geological repository.

Properties for each LLFP are shown in Table 2.1. The production reported in kg/GW·year is the amount of a given LLFP generated annually for every GW (thermal) of power generated in a light water reactor. Selinium-79 is the isotope produced in the lowest quantity while Zirconium-93 and Technetium-99 are produced in the largest quantities. Radiotoxicity, shown in (Sv/g), measures the internal dose due to inhalation or ingestion of the LLFP. Selinium-79 is the most toxic isotope, while Cesium-135 is the least.

Table 2.1: LLFP Properties

LLFP	Half-Life (Years)[2]	Production (kg/GW·yr)[6]	Radiotoxicity (Sv/g)[6]
Se79	6.50×10^5	0.066	8.259
Zr93	1.53×10^6	8.04	1.045
Tc99	2.11×10^5	8.54	0.6065
Sn126	1.00×10^5	0.30	6.306
I129	1.57×10^7	1.96	0.2696
Cs135	2.30×10^6	2.76	0.08532

Transmuting LLFPs is only beneficial if it significantly reduces a nuclear repository's overall radiotoxicity. A full transmutation facility will require significant economic and energy input, and each LLFP may require different irradiation methods to optimize transmutation. Therefore, it is beneficial to determine which LLFPs should be given the highest priority.

Selenium-79 is found in High-Level Liquid Waste (HLLW) and chemically behaves like

Table 2.2: Isotope Properties for Selenium

Isotope	Mass Fraction	Mol Weight (g/mol)	Number Density (atoms/cm^3)
Se77	0.0344	76.920	1.15805×10^{21}
Se78	0.0653	77.917	2.17015×10^{21}
Se79	0.1388	78.918	4.55431×10^{21}
Se80	0.2132	79.917	6.90808×10^{21}
Se82	0.5479	81.917	1.73195×10^{22}

a sulfate. It has the highest radiotoxicity of the six LLFPs (8.259 Sv/g); however, it is also produced in the lowest quantities (0.066 kg/GW·year). Separating Selenium-79 from HLLW may be challenging due to the small amount of Selenium-79 present compared to other sulfur compounds present[5]. Other isotopes of Selenium (Se-77, Se-78, Se-80, and Se-82) are also produced in spent fuel in mass fractions shown in Table 2.2.

Table 2.3: Isotope Properties for Zirconium

Isotope	Mass Fraction	Mol Weight (g/mol)	Number Density (atoms/cm^3)
Zr90	0.0173	89.905	7.5321×10^{20}
Zr91	0.1334	90.906	5.74404×10^{21}
Zr92	0.1622	91.22	6.96009×10^{21}
Zr93	0.2026	92.906	8.53591×10^{21}
Zr94	0.2197	93.906	9.15779×10^{21}
Zr96	0.2648	95.908	1.08073×10^{22}

Zirconium-93 is found in relatively large concentrations (8.04 kg/GW·year), comparable to Technetium-99, the most abundant LLFP. This large concentration and high radiotoxicity (1.045 Sv/g) make it an appealing candidate for transmutation. One potential challenge is the large amount of other Zirconium isotopes produced (Zr-90, Zr-91, Zr-92, Zr-94, and Zr-96) that will compete with Zirconium-93, decreasing transmutation efficiency[5]. The other isotopes are produced in mass fractions shown in Table 2.3.

Technetium-99 is found in metal and oxide form (TcO_2) as an insoluble residue and a soluble ion in HLLW. The insoluble form makes up the majority of Technetium-99 (80%) while the remaining (20%) is in soluble form. It has the highest production (8.54 kg/GW·year) but a relatively low radiotoxicity (0.6065 Sv/g). Both insoluble and soluble forms of Technetium-99 must be transmuted to significantly impact a repository's radiotoxicity. Extraction of insoluble Technetium-99 is more difficult than the soluble form which may pose challenges when reprocessing spent fuel[5]. There are no other isotopes of Technetium produced.

Like Technetium-99, Tin-126 is an insoluble residue and in a soluble form in HLLW. Tin-126 is produced in lower quantities (0.30 kg/GW·year) than other LLFPs except for Selenium-79 (the LLFP produced in the smallest quantities), but it has the second-highest radiotoxicity (6.306 Sv/g). Like Zirconium-93, many other isotopes of Tin (Sn-116, Sn-118, Sn-119, Sn-120, Sn-122, Sn-123, and Sn-124) are produced in spent fuel that will interfere

Table 2.4: Isotope Properties for Tin

Isotope	Mass Fraction	Mol Weight (g/mol)	Number Density (atoms/cm^3)
Sn115	0.0043	114.903	1.55499×10^{20}
Sn116	0.0557	115.902	1.99689×10^{21}
Sn117	0.0955	116.903	3.39444×10^{21}
Sn118	0.0976	117.902	3.43968×10^{21}
Sn119	0.0981	118.903	3.4282×10^{21}
Sn120	0.0978	119.902	3.38924×10^{21}
Sn122	0.1069	121.903	3.64379×10^{21}
Sn124	0.1482	123.905	4.96992×10^{21}
Sn126	0.2957	125.908	9.75861×10^{21}

with the transmutation of the target isotope (Sn-126), decreasing the overall efficiency[5]. Table 2.4 shows the proportion of each isotope produced.

Table 2.5: Isotope Properties for Iodine

Isotope	Mass Fraction	Mol Weight (g/mol)	Number Density (atoms/cm^3)
I127	0.27850	126.904	2.97354×10^{21}
I129	0.72150	128.905	7.58385×10^{21}

Iodine-129 in HLW is found in isolation and in CsI and ZrI_5 compounds. CsI is a soluble compound, and ZrI_4 is volatile. Iodine-129 is produced in relatively low quantities in reactors (1.96 kg/GW·year) and has a relatively low radiotoxicity (0.2696 Sv/g). However, of the six LLFPs, it is most likely to leak from a nuclear repository due to its high mobility in water. This high mobility makes it an important isotope to transmute. Iodine-127 is also produced in a smaller quantity, as shown in Table 2.5. For transmutation analysis, Iodine will be considered as part of a Cesium Iodine compound.

Table 2.6: Isotope Properties for Cesium

Isotope	Mass Fraction	Mol Weight (g/mol)	Number Density (atoms/cm^3)
Cs133	0.32870	132.905	3.35106×10^{21}
Cs134	0.00330	133.907	3.33913×10^{19}
Cs135	0.38060	134.906	3.82262×10^{21}
Cs137	0.28740	136.907	2.84436×10^{21}

Cesium-135 is produced in relatively high amounts (2.76 kg/GW·year) but has the lowest radiotoxicity (0.08532 Sv/g). For transmutation, Cesium must be separated from HLLW and will be considered as part of a Cesium Iodine compound. Other isotopes of Cesium (Cs-133, Cs-134, and Cs-137) are produced along with Cesium-135 in proportions shown in Table 2.6 and will interfere with transmutation.

2.2 Proton Accelerator Technology

Commercially available proton cyclotrons produce 9-70 MeV energy protons. Depending on the material, desirable proton reaction cross sections begin at 9-18 MeV. Therefore, proton cyclotrons are valuable tools for transmutation problems. Additionally, proton cyclotron technology exists commercially, which can decrease the overall cost of the complete transmutation process.

Figure 2.1 shows a simplified diagram of a proton cyclotron. A typical cyclotron is built from two hollow electrodes called "the dees" due to their "D"-like shape. An RF voltage is applied across these electrodes to generate an electric field and accelerate an ion between the electrodes. The presence of a magnetic field perpendicular to the direction of the electric field forces the ions to begin moving in circular orbits. As the ion is accelerated, moving back and forth between the electrodes, the orbit radius increases until the ion is at the desired energy. Once the ion reaches the maximum radius, it is extracted from the electrodes, forming the ion beam.

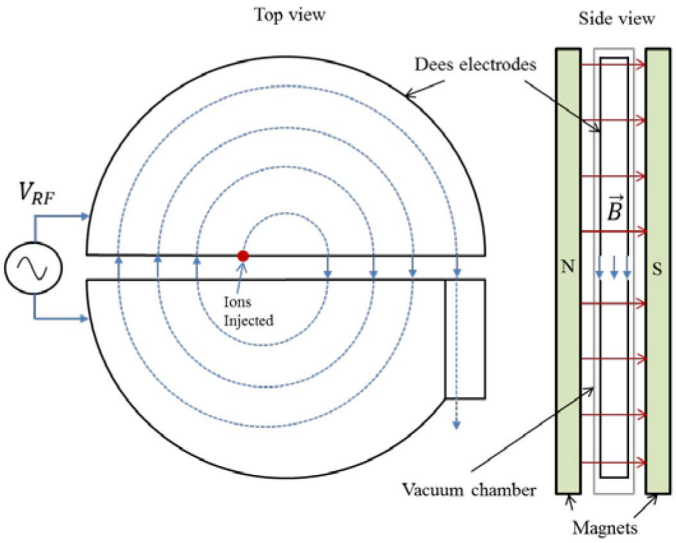

Figure 2.1: Simplified schematic of a proton cyclotron adapted from Ref. [7].

The flux of the proton beam is one of the major factors limiting the amount of transmutation possible. A higher proton beam flux will allow more transmutation in a shorter irradiation time. The flux of a beam is related to the amount of current produced. The larger the beam current, the larger the flux for a given radius. Proton accelerators can also produce proton beams of various energies. Energy flexibility is useful for optimizing the transmutation of each LLFP.

2.3 Transmutation

The eventual goal of this work is to design an irradiation facility capable of transmuting LLFPs. Figure 2.2 shows a sketch of the proposed irradiation model for a future facility.

The target will be a single LLFP or mix of LLFPs with higher proton reaction cross sections. Most of the reaction cross sections that result in transmutation produce secondary neutrons. Therefore, the target will be surrounded by other LLFPs with higher neutron cross sections. These blanket LLFPs will be irradiated by protons that escape the target material and the neutrons produced from the initial proton reactions in the target material. This thesis will not go into depth regarding the target design. However, this eventual transmutation scheme is the motivation driving subsequent analysis.

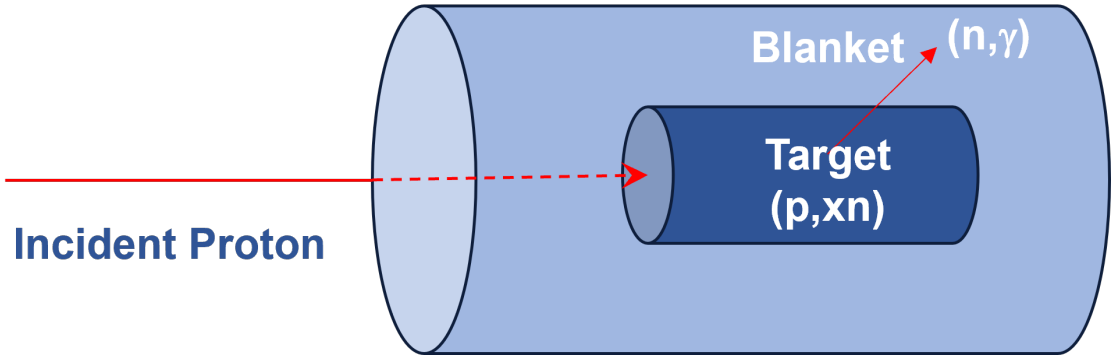

Figure 2.2: Target design for proposed irradiation scheme

Chapter 3

Methodology

3.1 Computational Methods

To accurately model the complete transmutation of the various LLFPs, the following codes will be employed: TALYS[8], TASMAN[9], FISPACT[10], the Particle and Heavy Ion Transport code System (PHITS)[11], and The Stopping and Range of Ions in Matter (SRIM)[12]. These codes are implemented in the following calculations to capture the complete irradiation process:

Proton Irradiation

1. Cross Section Generation: TALYS
2. Uncertainty Estimation: TALYS and TASMAN
3. Flux Spectrum: PHITS
4. Beam Penetration Distance: PHITS
5. Depletion Calculation: FISPACT

Proton, Alpha, and Deuteron Irradiation

1. Cross Section Library: TENDL2021
2. Beam Penetration Distance: SRIM
3. Depletion Calculation: FISPACT

3.1.1 Cross Section Generation

TALYS is a nuclear reaction model code that simulates neutron, photon, proton, deuteron, triton, ^{3}He, and alpha particle reactions up to 200 MeV. TALYS can generate and output reaction cross sections across a broad energy range from the internal nuclear reaction models. The reaction models in TALYS are meant to predict all reaction channels instead of providing a detailed description of only some reaction channels. TALYS has applications in nuclear fission reactor technology, fusion reactors, accelerator physics, homeland security, medical isotope production, radiotherapy, astrophysics, and more[8]. For this thesis, TALYS generated cross sections will be compared to the TENDL2021 repository. Due to the lack of

measured differential cross sections, data validation is difficult. The TENDL2021 repository will provide a reference point to compare the TALYS-generated cross sections to verify their quality.

The most straightforward TALYS calculations require only four input parameters: incoming particle type, incoming particle energy, target mass number, and target element. Additional keywords can be added to input files for more specific calculations, depending on the application desired by the user. Keywords necessary for computation that the user does not specify will be automatically added by the TALYS computation and included in the output file. The simplicity of TALYS input files allows the user to obtain cross sections quickly. However, it also means incorrect results that seem complete can be obtained. Therefore, the user must understand what keywords are necessary for their application.

In physics, nuclear reactions are usually categorized according to the time scale of the reaction or the number of intranuclear collisions involved. Reactions with short time scales and one or two collisions are considered direct reactions. Reactions with intermediate time scales and several collisions are pre-equilibrium reactions. In these reactions, the compound nucleus produced by the reactants never reaches statistical equilibrium. Reactions with long time scales and many intranuclear collisions are considered compound reactions, referring to the compound nucleus formed during the interaction. Reactions where the initial reactants are the same as the products are separately defined as elastic reactions. A flow chart detailing the process of each reaction type is shown in Figure 3.1.

Each reaction type also produces products with distinct resultant energies. Figure 3.2 shows each reaction type's energy regime and reaction time. Energy increases moving to the right on the x-axis, while reaction time increases moving to the left on the x-axis. The dashed line shows the full contribution of compound reactions to the total particle spectra.

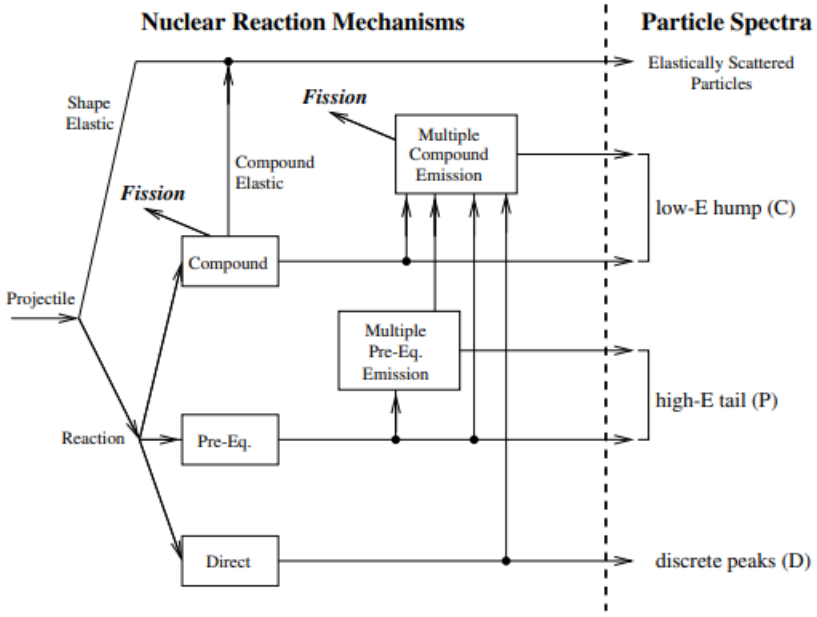

Figure 3.1: A flowchart of various nuclear reactions and their influence on the outgoing particle spectra of the products adapted from Ref. [8].

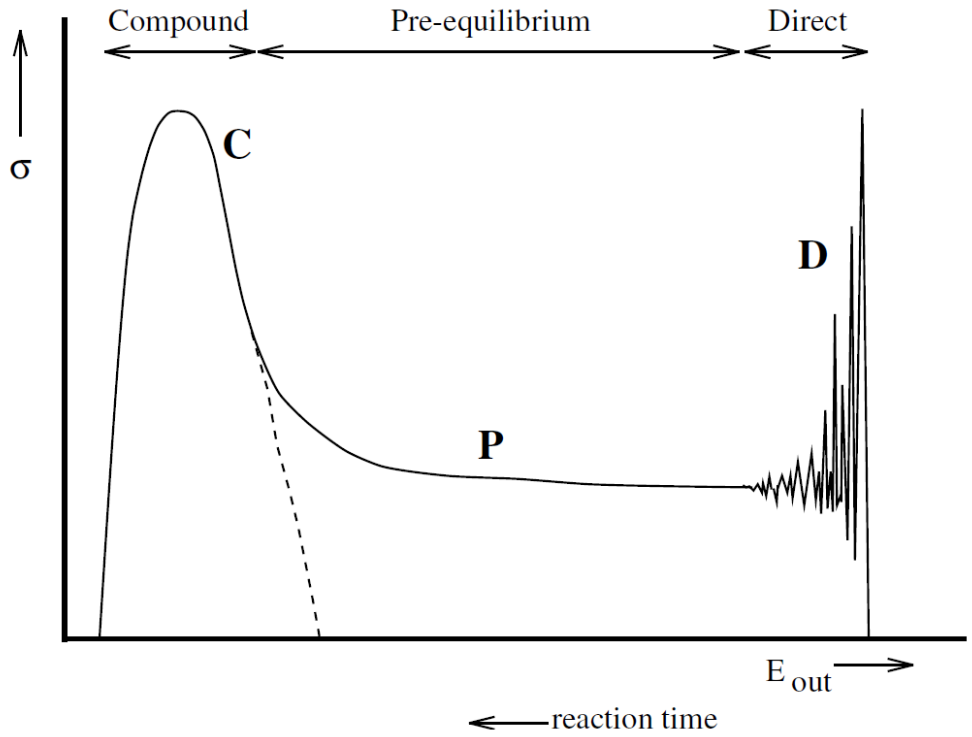

Figure 3.2: Direct(D), pre-equilibrium (P), and compound (C) reactions contribute to distinct parts of the product particle spectra adapted from Ref. [8].

However, a software package needs more than this framework for defining nuclear reactions. TALYS considers each reaction to be a binary reaction only involving two reactants and two products. The identity of the two products depends on the reaction type. TALYS considers all possible reaction channels available at the incident energy and tracks all additional reactions that follow the initial binary reaction to capture more complex reactions involving more than two products. Figure 3.3 shows the complete process TALYS uses to track a reaction between a neutron and target ${}^{A_C-1}_{Z_C}X_{N_C-1}$. Each box represents distinct nuclides defined relative to the number of protons Z_C and neutrons N_C in the compound nucleus. The energy levels of the nucleus are shown as lines within the boxes. The initial reaction forming a compound nucleus ${}^{A_C-1}_{Z_C}X_{N_C-1} + n \rightarrow {}^{A_C}_{Z_C}X_{N_C}$ is shown by the dashed line moving from the center nucleus to the upper right. Three of the many potential binary reaction channels are shown: neutron emission ${}^{A_C-1}_{Z_C}X_{N_C-1} + n \rightarrow {}^{A_C-1}_{Z_C}X_{N_C-1} + n$, proton emission ${}^{A_C-1}_{Z_C}X_{N_C-1} + n \rightarrow {}^{A_C-1}_{Z_C-1}X_{N_C} + p$, and deuteron emission ${}^{A_C-1}_{Z_C}X_{N_C-1} + n \rightarrow {}^{A_C-2}_{Z_C-1}X_{N_C-1} + d$. As shown in Figure 3.3, each residual nuclide may undergo additional decay processes. These additional reactions occur if the residual nuclide has more energy than the necessary separation energy for particle emission notated as S_i in the diagram, where i is the emitted particle. The reaction chain ceases once the nuclide energy is lower than the separation energies for any particle emission. The nuclide in the lower left corner of Figure 3.3 ends this specific reaction chain. TALYS can generate nuclear data for all available channels by tracking all possible reactions this way. TALYS outputs contain all relevant reaction data

the user requests. The package TEFAL[8] converts TALYS output files into the ENDF-6 format for use in PHITS and FISPACT calculations.

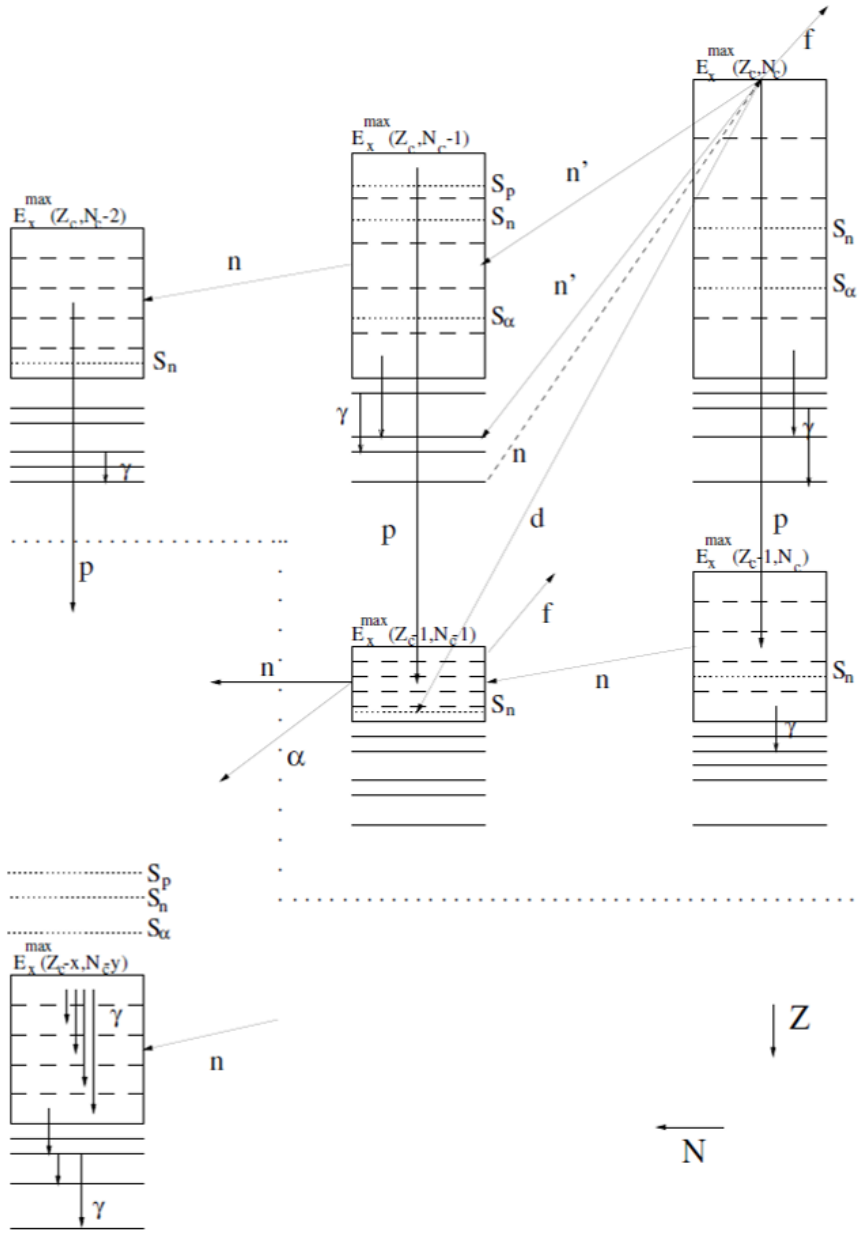

Figure 3.3: TALYS process for calculating an incident neutron reaction considering all possible reaction channels adapted from Ref. [8].

3.1.2 Uncertainty Estimation

In addition to generating proton reaction cross sections, TALYS will be used with the statistical software TASMAN to evaluate cross section uncertainties. TALYS computations only provide a single value for all calculations; they cannot directly handle uncertainty propagation or probability distributions. However, TASMAN can perturb the optical model

parameters TALYS employs to generate cross sections. These perturbations will produce a set of perturbed cross sections that will be used to estimate the uncertainty.

The optical model used in TALYS assumes that a complex mean-field potential can model interactions between an incident particle and the target nucleus. This potential divides the reaction flux into a part containing elastic scattering information and a part describing all non-elastic channels. The Schrödinger equation is then solved numerically using the potential function. This process returns information about the elastic angular distribution and polarisation, the reaction and total cross section, the s and p-wave strength functions, and the potential scattering radius R'.

TALYS uses the local and global parameterization developed by Koning and Delaroche[13] to describe optical model potentials. The potential used in TALYS, $\mathcal{U}(r, E)$, is defined as:

$$\begin{aligned}\mathcal{U}(r,E) = &-\mathcal{V}_V(r,E) - i\mathcal{W}_V(r,E) - i\mathcal{W}_D(r,E) \\ &+ \mathcal{V}_{SO}(r,E).\mathbf{1}.\boldsymbol{\sigma} + i\mathcal{W}_{SO}(r,E).\mathbf{1}.\boldsymbol{\sigma} + \mathcal{V}_C(r)\end{aligned} \tag{3.1}$$

where $\mathcal{V}_{V,SO}$ and $\mathcal{W}_{V,D,SO}$ are the real and imaginary parts of the volume (V), surface (D), spin-orbit (SO), and Coulomb (C) potentials. E is the energy of the incident particle in the lab frame and r is the radial position.

Each position-dependent potential function is further separated into a radial and energy-dependent component:

$$\begin{aligned}\mathcal{V}_V(r,E) &= V_V(E) f(r, R_V, a_V) \\ \mathcal{W}_V(r,E) &= W_V(E) f(r, R_V, a_V) \\ \mathcal{W}_D(r,E) &= -4a_D W_D(E) \frac{d}{dr} f(r, R_D, a_D) \\ \mathcal{V}_{SO}(r,E) &= V_{SO}(E) \left(\frac{\hbar}{m_\pi c}\right)^2 \frac{1}{r}\frac{d}{dr} f(r, R_{SO}, a_{SO}) \\ \mathcal{W}_{SO}(r,E) &= W_{SO}(E) \left(\frac{\hbar}{m_\pi c}\right)^2 \frac{1}{r}\frac{d}{dr} f(r, R_{SO}, a_{SO})\end{aligned} \tag{3.2}$$

where $R_i = r_i A^{1/3}$ is the radius, a_i is the diffuseness parameter, and f is the form factor described by a Woods-Saxon shape.

$$f(r, R_i, a_i) = (1 + \exp\left(\frac{r - R_i}{a_i}\right))^{-1} \tag{3.3}$$

V_C is the Coulomb potential defined as:

$$\begin{aligned}\mathcal{V}_C(r) &= \frac{Zze^2}{2R_C}\left(3 - \frac{r^2}{R_C^2}\right) \quad \text{for} \quad r \leq R_C \\ &= \frac{Zze^2}{r} \quad \text{for} \quad r > R_C\end{aligned} \tag{3.4}$$

where Z is the charge of the target, z is the charge of the incident particle, and R_C is the Coulomb radius.

The full parameterization of the optical model potential is:

$$\begin{aligned}
V_V(E) &= v_1\left(1 - v_2(E-E_f) + v_3(E-E_f)^2 - v_4(E-E_f)^3\right) \\
W_V(E) &= w_1\frac{(E-E_f)^2}{(E-E_f)^2 + w_2^2} \\
r_V &= \text{constant} \\
a_V &= \text{constant} \\
W_D(E) &= d_1\frac{(E-E_f)^2}{(E-E_f)^2 + d_3^2}\exp(-d_2(E-E_f)) \\
r_D &= \text{constant} \\
a_D &= \text{constant} \\
V_{SO}(E) &= v_{so1}exp(-v_{so2}(E-E_f) \\
W_{SO}(E) &= w_{so1}\frac{(E-E_f)^2}{(E-E_f)^2 + w_{so2}^2} \\
r_{SO} &= \text{constant} \\
a_{SO} &= \text{constant} \\
r_C &= \text{constant}
\end{aligned} \tag{3.5}$$

where E_f is the Fermi energy defined as the energy halfway between the nucleus's last occupied and first unoccupied shell.

The parameters: v_1, v_2, v_3, v_4, w_1, w_2, d_1, d_2, d_3, v_{so1}, v_{so2}, w_{so1}, w_{so2}, and E_f are the terms perturbed by the TASMAN software to obtain an estimate of the uncertainty.

3.1.3 Proton Flux Spectrum

The depletion calculation performed in this thesis requires information about the flux spectrum of the incident beam and the number of nuclides irradiated by the beam. These quantities were calculated separately in the work supporting this thesis using PHITS.

PHITS is a Monte Carlo code system that models and tracks the transport of particles with energies of up to 1 TeV. PHITS computations require users to supply the geometrical layout for their simulation and nuclear data. The user can create the geometry design in PHITS or construct it from imported CAD files created in a separate program. The TALYS generated cross sections previously discussed provide the nuclear data. PHITS allows tallies to be input into the geometry to obtain a flux-energy spectrum throughout this material. This flux-energy spectrum will be used directly for the depletion calculation. The point where the flux of the beam goes to essentially zero will be used to determine the penetration depth of the beam and, therefore, the number of nuclides irradiated by the beam.

3.1.4 Penetration Distance

SRIM is an additional software package that models the transport of ions in materials. It is typically used to calculate ion stopping power, ion range, ion implantation, sputtering, and more. SRIM can model the transport of protons, alphas, and deuterons. The number of irradiated particles in a target can be estimated from the SRIM-calculated penetration depth in a less computationally expensive way than with PHITS.

The physics employed by SRIM for energetic light ions (H, He, and Li above 1 MeV/u) is described by the Bethe-Bloch equation[14]. Assuming that the incident ion is moving much faster than the target electrons and is fully stripped, is much heavier than the target electrons, and only loses energy through Coulomb interactions, the Bethe-Bloch stopping power equation is expressed as:

$$S(E) = \frac{4\pi z^2 n_0}{m_0 \beta^2 c^2} \left(\frac{e^2}{4\pi\epsilon_0^2}\right)^2 \left[\ln(\frac{2m_0\beta^2c^2}{P} - \ln(1-\beta^2) - \beta^2\right] \tag{3.6}$$

where z is in the charge number, n_0 is the electron number density in [atoms $\cdot$ cm^{-3}], m_0 is the electron rest mass, c is the speed of light, e is the electron charge, ϵ_0 is the permittivity of free space, and P is the ionization potential in [MeV].

β^2 is a function of the incident kinetic energy (E) expressed as,

$$\beta^2 = 1 - \left(\frac{mc^2}{E + mc^2}\right) \tag{3.7}$$

where m is the projectile mass and E is the projectile kinetic energy expressed in [eV].

Stopping power calculated with the Bethe-Bloch equation matches experimental values within 3%[14], providing an accurate model for light ions traveling through a material.

3.1.5 Depletion Calculations

Once the LLFP nuclear data is obtained, FISPACT will perform depletion calculations. FISPACT is an inventory code that models neutron, proton, alpha, deuteron, or gamma particle activation, transmutation, and depletion maintained by the UK Atomic Energy Authority. FISPACT takes a beam flux, irradiation time, target, and projectile particle and returns detailed information about the isotopes produced, including decay heat, activity, dose, nuclide abundance, gamma-spectra, and more. However, FISPACT does not consider the geometry of the target when completing the inventory calculation, so PHITS will be used to complement the FISPACT calculations.

FISPACT produces results by solving the set of rate equations for an infinite, homogeneous, and infinitely dilute material[15]:

$$\frac{dN_i}{dt} = \sum_j (\lambda_i^j + \sigma_i^j \phi^{int}(t)) N_j \tag{3.8}$$

where N_i is the number of nuclide i at time t and ϕ^{int} is the projectile flux in units of [cm$^{-2}\cdot$s^{-1}]. When $j \neq i$ λ_i^j is the decay constant [s^{-1}] for nuclide j decaying into nuclide i and σ_i^j is the reaction cross section [cm^2] for nuclide j reactions that produce nuclide i.

When $j = i$ $-\lambda_j^j$ is the total decay constant [s^{-1}] for nuclide j and $-\sigma_j^j$ is the total reaction cross section [cm^2] for nuclide j.

Cross section data generated from TALYS and flux data from PHITS initially depend on energy. However, Equation 3.8 requires both to be energy independent. Therefore, in the first step of a FISPACT calculation, the cross section and flux data are collapsed and condensed to obtain flux averaged cross sections for each reaction:

$$\sigma_i^j = \frac{\sum_k \tilde{\sigma}_i^j(E_k)\phi(E_k)}{\sum_k \phi(E_k)} \tag{3.9}$$

where $\tilde{\sigma}_i^j(E_k)$ is the original cross section value and $\phi(E_k)$ is the original flux value energy group k. Values are summed over all k energy groups.

Removing energy dependence along with the assumption that the flux is not modified by interactions with the target material allows Equation 3.8 to be expressed as a matrix-vector expression:

$$\frac{d\vec{\mathrm{N}}}{dt} = \mathbf{A}\vec{\mathrm{N}} \tag{3.10}$$

where matrix $\mathbf{A}$ containing decay, cross section, and flux information is independent of vector $\vec{\mathrm{N}}$ describing the number of nuclides of each type present in the system. Although matrix A is large, it is also sparse, which allows FISPACT's ODE solver to take advantage of numerical methods to improve calculation efficiency.

3.2 Proton Transmutation

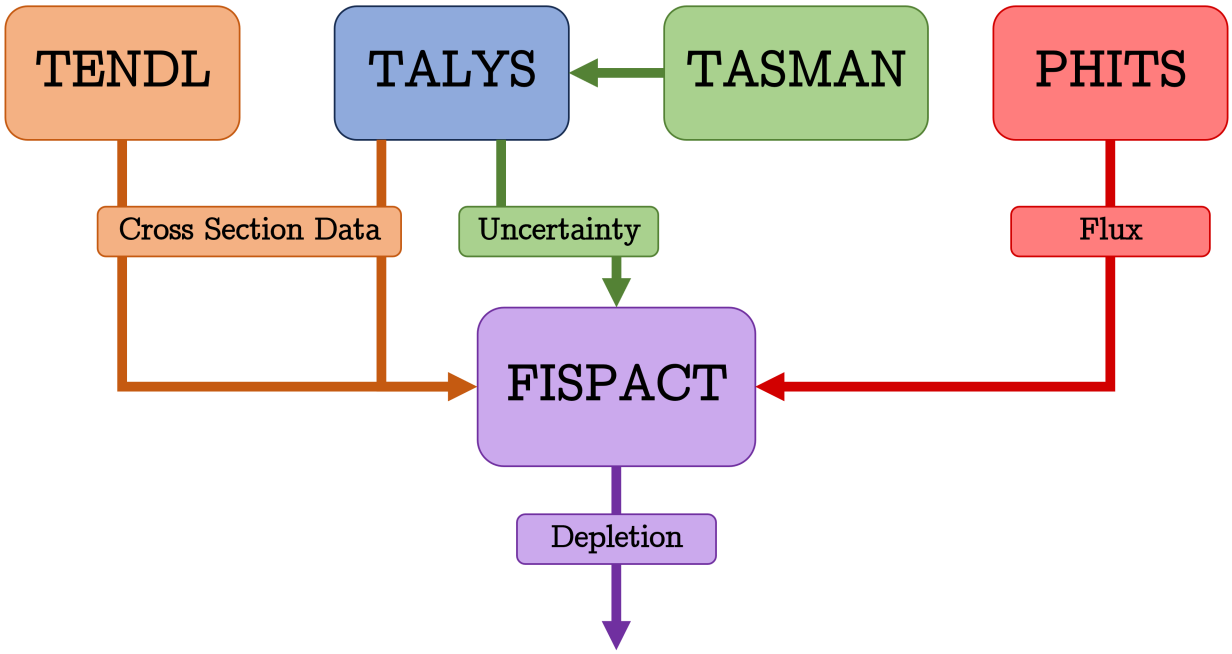

Figure 3.4: Computational workflow for the proton transmutation section with cross section data from the TENDL data library and TALYS, uncertainty calculations from TEFAL with TALYS, and proton flux data from PHITS.

For proton transmutation, an estimation of the number of nuclides transmuted for a given LLFP will be calculated using TALYS, TASMAN, FISPACT, and PHITS as shown in Figure 3.4.

As experimental data is unavailable, TALYS will generate the proton cross sections. The TENDL[16] nuclear data library is a repository developed using the TALYS code that will be compared to the TALYS-generated cross sections to provide a reference point. A perfect match between TALYS generated and TENDL cross section files is unlikely as the TALYS input files for the data libraries are not provided with the TENDL library. However, any significant discrepancies may indicate that the new TALYS-generated cross sections are not representing the data correctly.

The range of achievable transmutation rates will heavily depend on the uncertainty of the proton cross sections. Therefore, TASMAN will be used to provide an estimate of this uncertainty. The random cross sections generated from TALYS and TASMAN will be propagated through the rest of the computational flow to estimate the downstream uncertainty.

FISPACT will be used to perform the transmutation calculations for a proton beam and target material using the cross sections generated from TALYS. However, FISPACT does not consider target geometry, so PHITS will be used to model the change in the beam flux spectrum as it travels through the target and determine the penetration depth of the beam. The penetration depth will be used to calculate the number of atoms irradiated by the proton beam, which will be input into FISPACT.

3.3 Proton, Alpha, and Deuteron Comparison

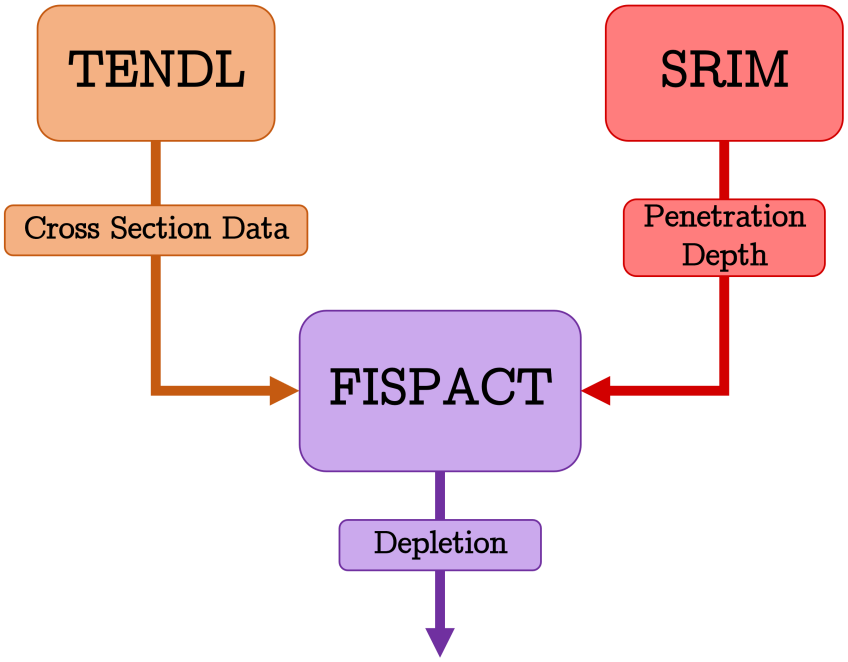

Figure 3.5: Computational workflow for the proton, alpha, and deuteron section with nuclear data sourced from the TENDL2021 data library and penetration depth calculations performed with SRIM.

The workflow will be simpler for comparing proton, alpha, and deuteron irradiation than the in-depth proton analysis. This analysis will utilize the TENDL2021 data library, SRIM, and FISPACT, as shown in Figure 3.5.

Instead of generating cross sections with TALYS for all three particle types, pre-generated cross sections from the TENDL2021 data repository described above will be used for all three particles. In the previous section, it was necessary to have the ability to fine-tune the cross sections and estimate uncertainty to determine the optimal irradiation scheme. This section aims to determine the difference between proton, alpha, and deuteron irradiation so the same level of precision is not required.

The penetration depth, which can be used to calculate the number of particles seen by the beam, will be calculated using SRIM. As discussed in a previous section, SRIM calculates the penetration depth of the beam in a less computationally expensive way than PHITS. For the proton, alpha, and deuteron comparison, the same level of precision as the proton-only analysis is not required.

The final transmutation calculation will be performed using FISPACT in the same way as the previous section.

Chapter 4

Results and Discussion

4.1 Proton Transmutation

4.1.1 Cross Section Generation

Figures 4.1-4.6 show the TALYS-generated cross section data[17] for all 6 LLFPs for the following reaction channels: (p,anything), (p,n), (p,2n), (p,3n), (p,na), (p,np), (p,4n), (p,p), (p,d), (p,t), (p,He3), and (p,a). "n" is a neutron, "p" is a proton, "a" is an alpha particle, "d" is a deuteron, "t" is a triton, and "He3" is a Helium-3 nucleus. (p,anything) reactions represent any inelastic reaction not captured by the channels mentioned previously. TALYS is capable of modeling reactions from 0-200 MeV. However, the commercial accelerators considered in this thesis do not generate protons above 70 MeV. Therefore, the plots shown below only show reaction data below 70 MeV.

FISPACT requires input cross section data to be in the ENDF-6[18] format. TALYS generated cross sections are stored in the ENDF MF=3 file according to the CCFE-162 group structure. Cross section values in the energy of interest (18-70 MeV) range from 10^{-6} to 1 barn. All reaction channels have similar cross section behavior. For each reaction type, there is an activation energy; once the energy of the incoming proton is greater than that activation energy, the value of the cross section increases significantly. Then, as energy increases, the cross section for the reaction drops as other reaction channels dominate. As energy increases, more and more reaction types become available. The cross sections between isotopes also have similar behaviors and shapes between reaction types, while isotopes with smaller atomic masses have their cross sections shifted lower in energy.

Figure 4.1: TALYS generated proton cross sections for all LLFPs from 2-70 MeV, the rough energy range of commercial proton cyclotrons.

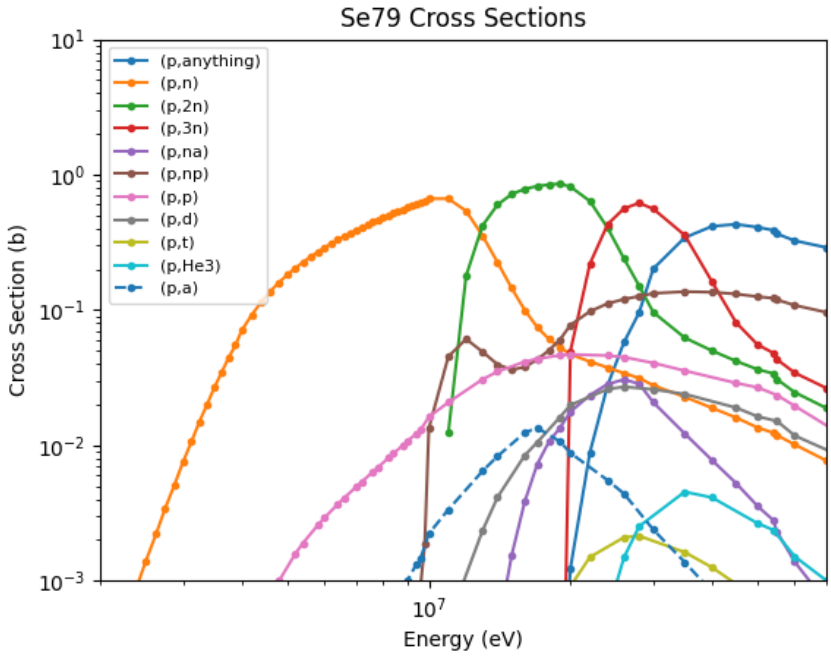

Figure 4.2: Zirconium-93 TALYS generated proton cross sections from 2-70 MeV, the rough energy range of commercial proton cyclotrons.

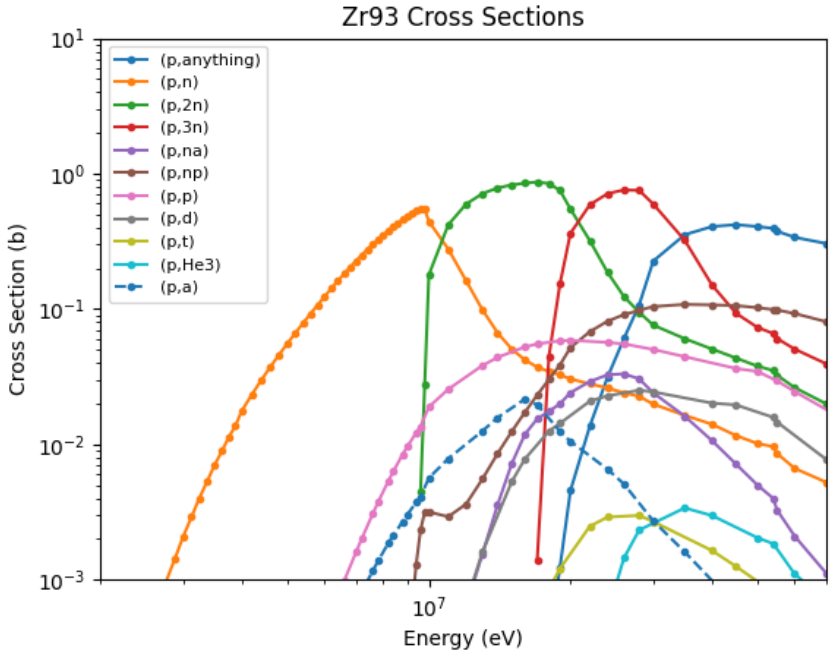

Figure 4.3: Technetium-99 TALYS generated proton cross sections from 2-70 MeV, the rough energy range of commercial proton cyclotrons.

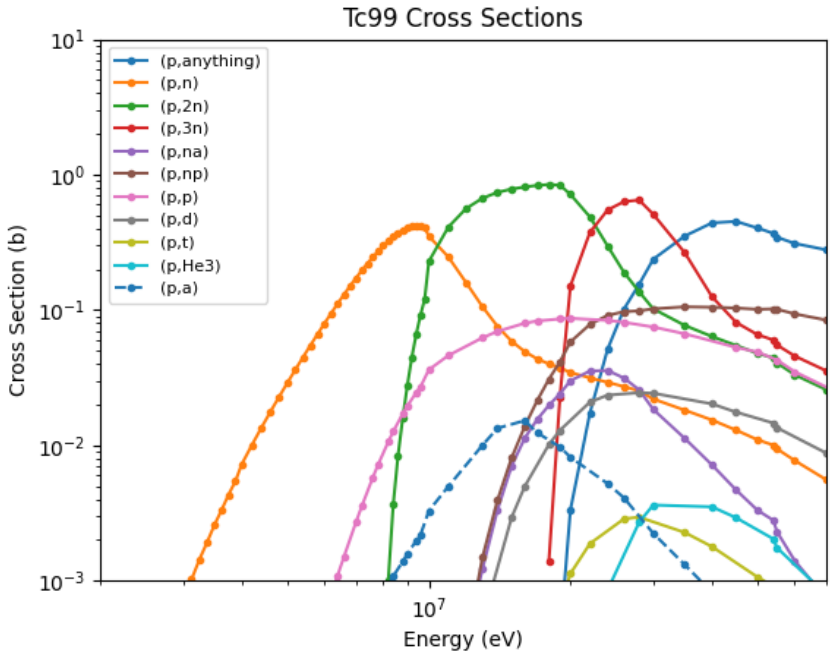

Figure 4.4: Tin-126 TALYS generated proton cross sections from 2-70 MeV, the rough energy range of commercial proton cyclotrons.

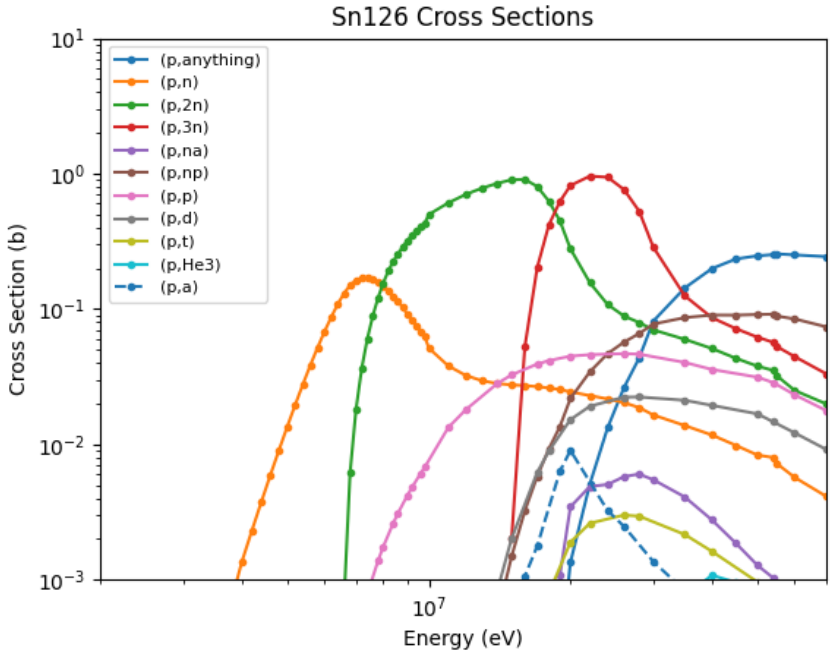

Figure 4.5: Iodine-129 TALYS generated proton cross sections from 2-70 MeV, the rough energy range of commercial proton cyclotrons.

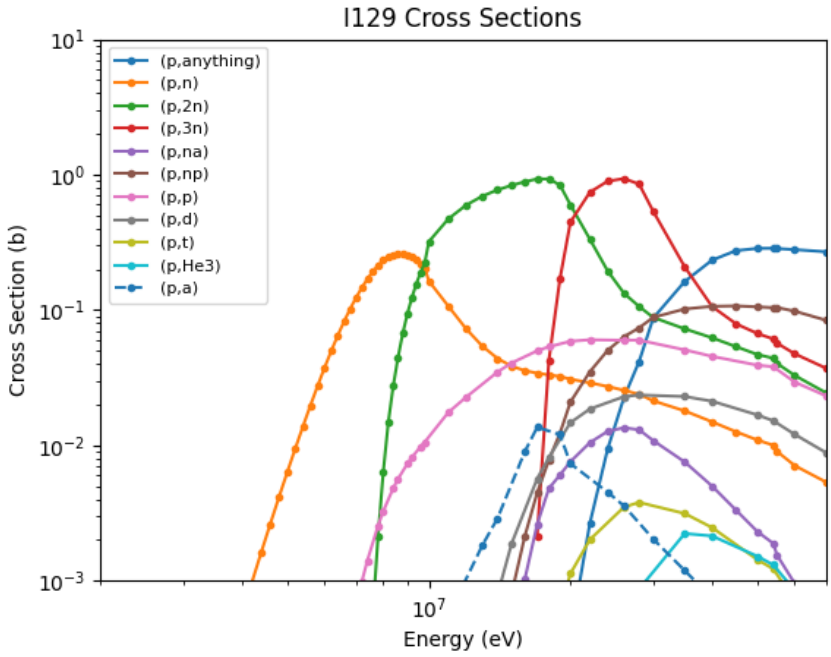

Figure 4.6: Cesium-135 TALYS generated proton cross sections from 2-70 MeV, the rough energy range of commercial proton cyclotrons.

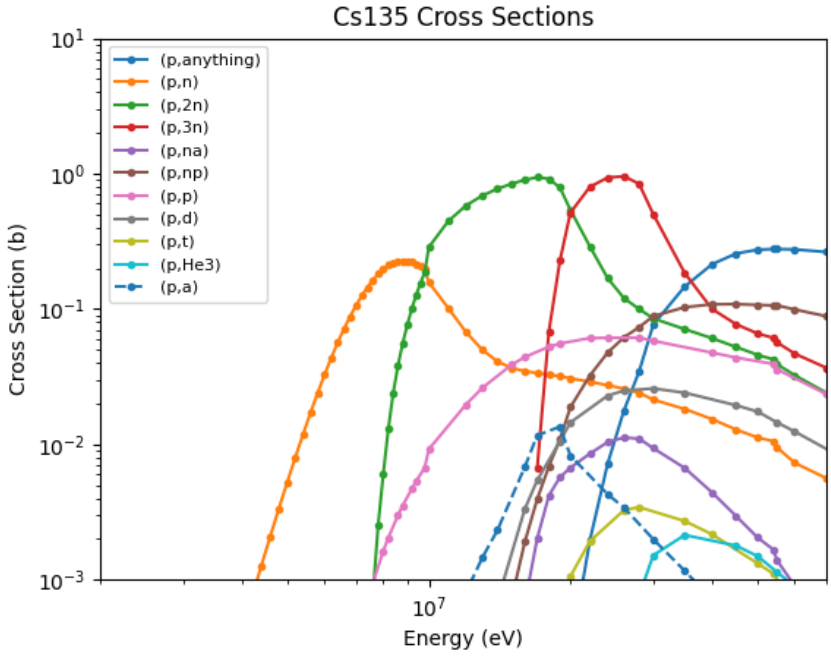

Figures 4.7-4.12 show the proton cross sections in the TENDL2021 library below 70 MeV. In the TENDL2021 library, explicit reaction channels in file 3 (MF=3) are only included up to 30 MeV. Above this energy cutoff, the total inelastic cross section is stored in section 5 (MT=5) of file 3 which corresponds to the (p,anything) reaction. Information about specific inelastic reaction channels is stored in files 6 and 10 (MF=6, MF=10). These files store energy-angle distributions for emitted particles and cross sections for radioactive nuclide production.

Besides the difference in the (p,anything) cross section, the TENDL2021 and TALYS-generated cross sections are very similar, suggesting no significant issues with the TALYS cross sections generation process.

Figure 4.7: TENDL2021 Selenium-79 cross sections from 2-70 MeV, the rough energy range of commercial proton cyclotrons.

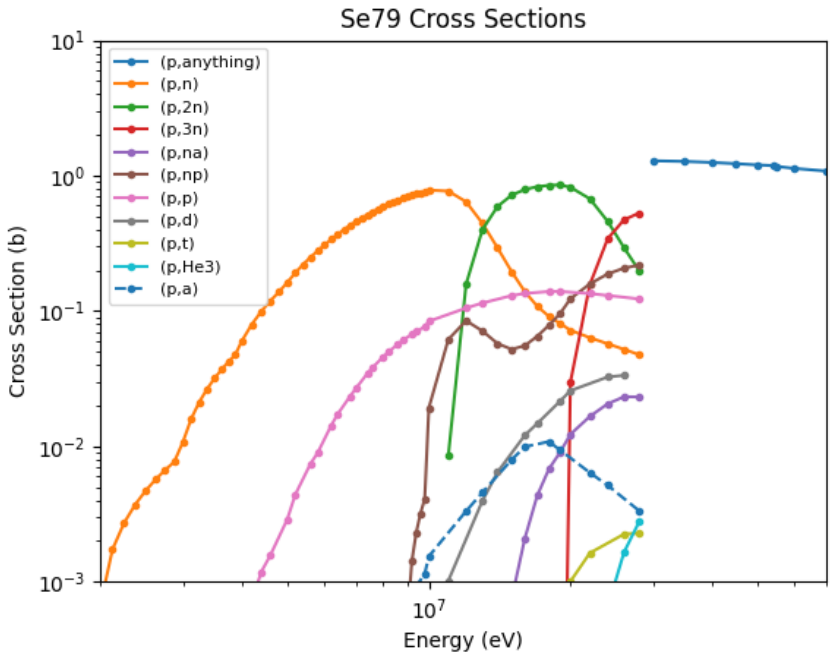

Figure 4.8: TENDL2021 Zirconium-93 cross sections from 2-70 MeV, the rough energy range of commercial proton cyclotrons.

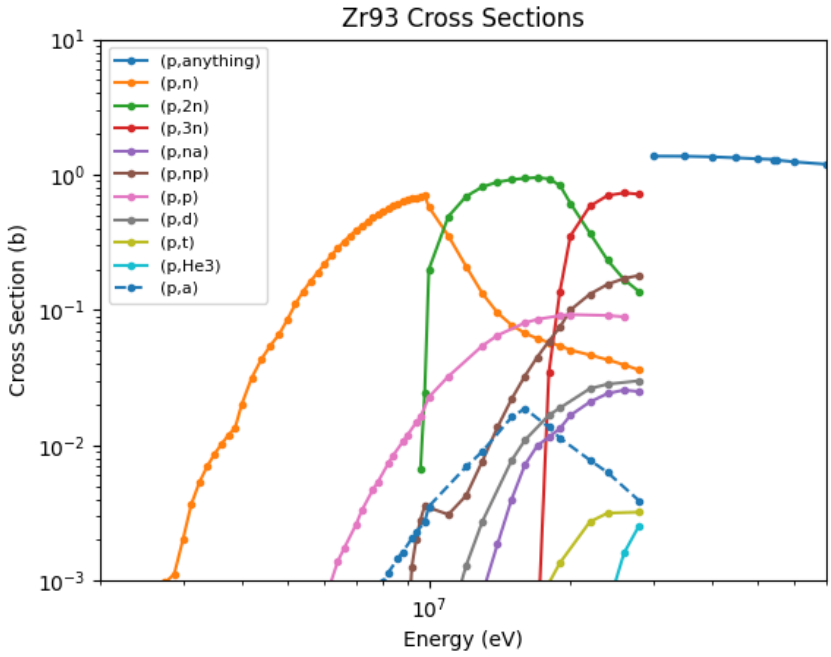

Figure 4.9: TENDL2021 Technetium-99 cross sections from 2-70 MeV, the rough energy range of commercial proton cyclotrons.

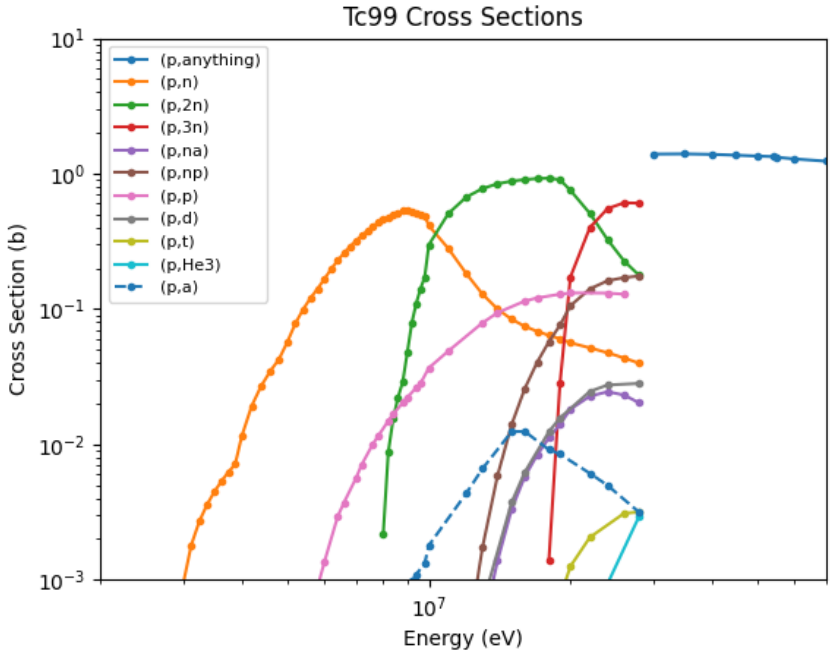

Figure 4.10: TENDL2021 Tin-126 cross sections from 2-70 MeV, the rough energy range of commercial proton cyclotrons.

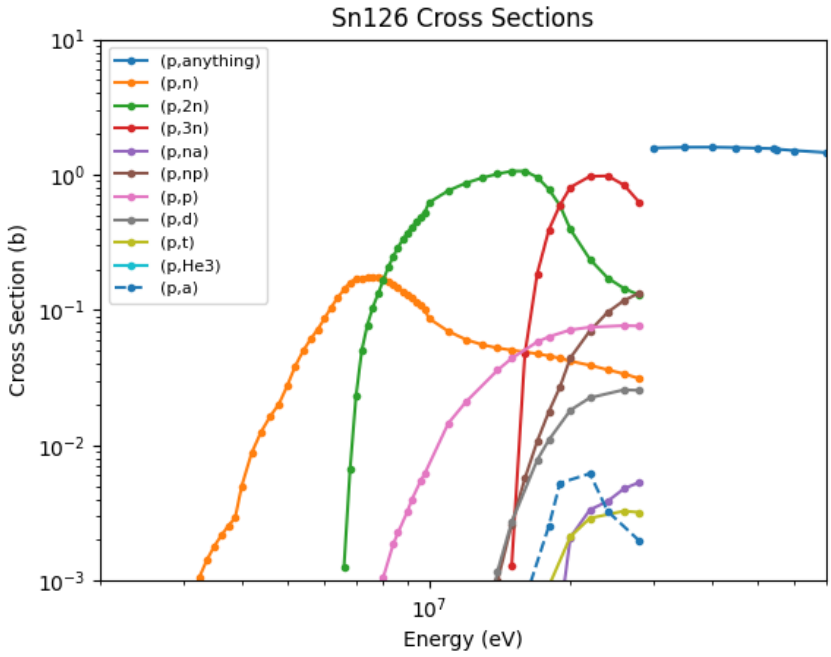

Figure 4.11: TENDL2021 Iodine-129 cross sections from 2-70 MeV, the rough energy range of commercial proton cyclotrons.

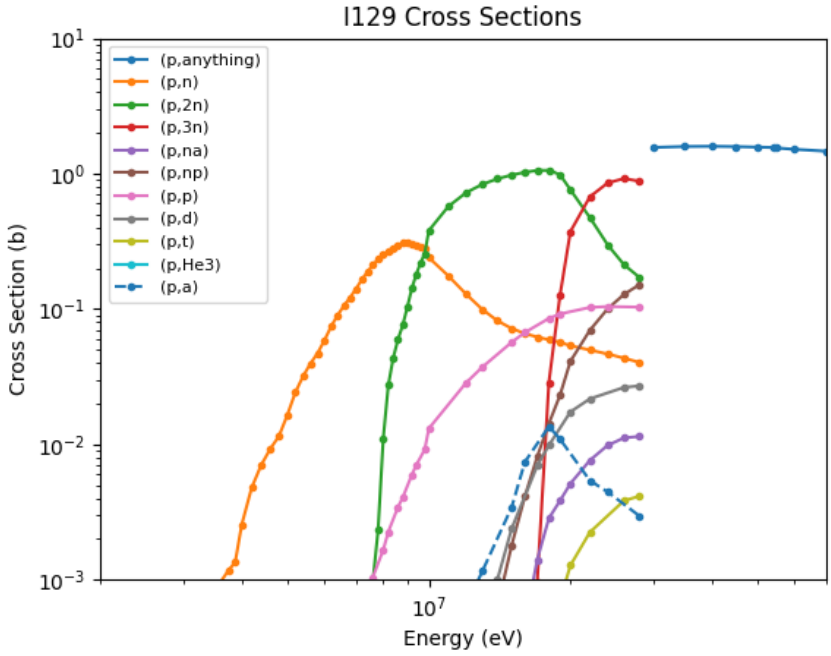

Figure 4.12: TENDL2021 Cesium-135 cross sections from 2-70 MeV, the rough energy range of commercial proton cyclotrons.

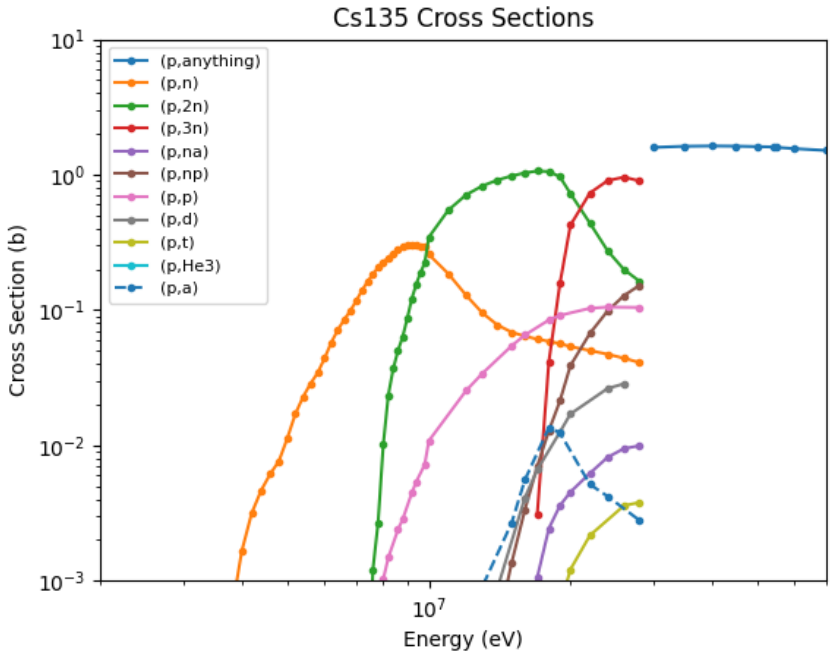

4.1.2 Uncertainty Estimation

Figures 4.13-4.18 show the TASMAN perturbed (p,anything) cross sections from 1-30 MeV generated in work supporting this thesis[17]. Each perturbed cross section is plotted in red, with the average cross section value for each energy plotted in blue. The cross section in this energy regime has values from order 10^{-18} to 10^{-1} barns. Cross section values above 30 MeV are stored in ENDF files 6 and 10, as in the TENDL2021 library, divided into the appropriate production channels. All other cross section channels are perturbed similarly to the (p,anything) cross section shown.

Figure 4.13: Selenium-79 Perturbed (p,anything) Cross Section

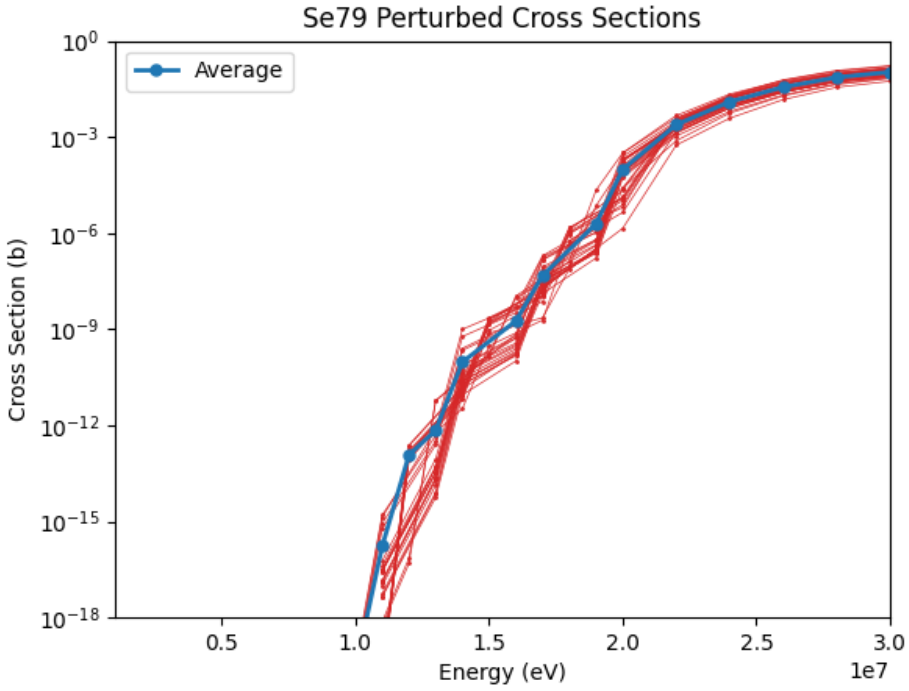

Figure 4.14: Zirconium-93 Perturbed (p,anything) Cross Section

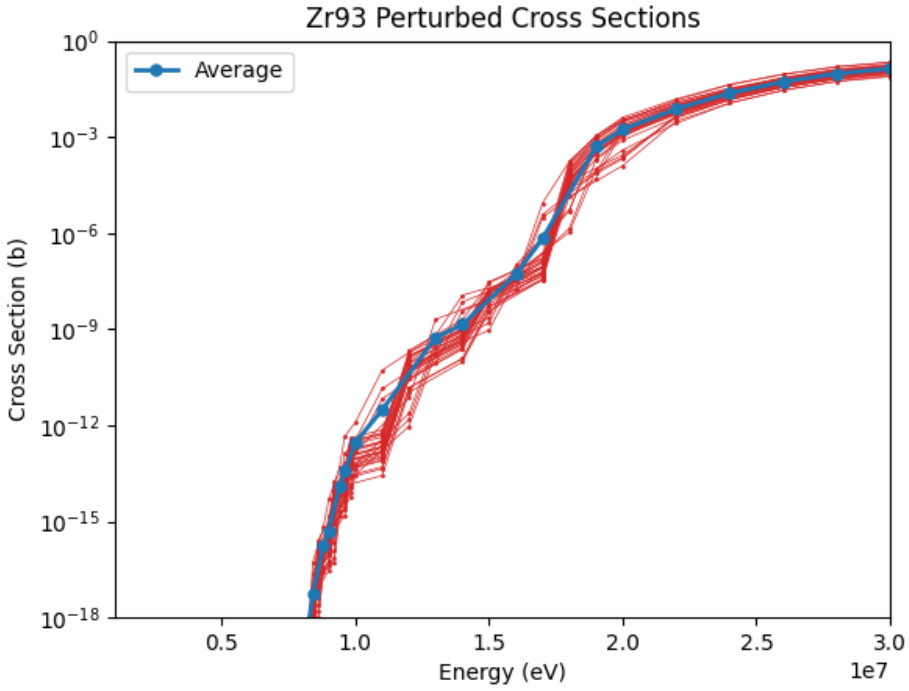

Figure 4.15: Technetium-99 Perturbed (p,anything) Cross Section

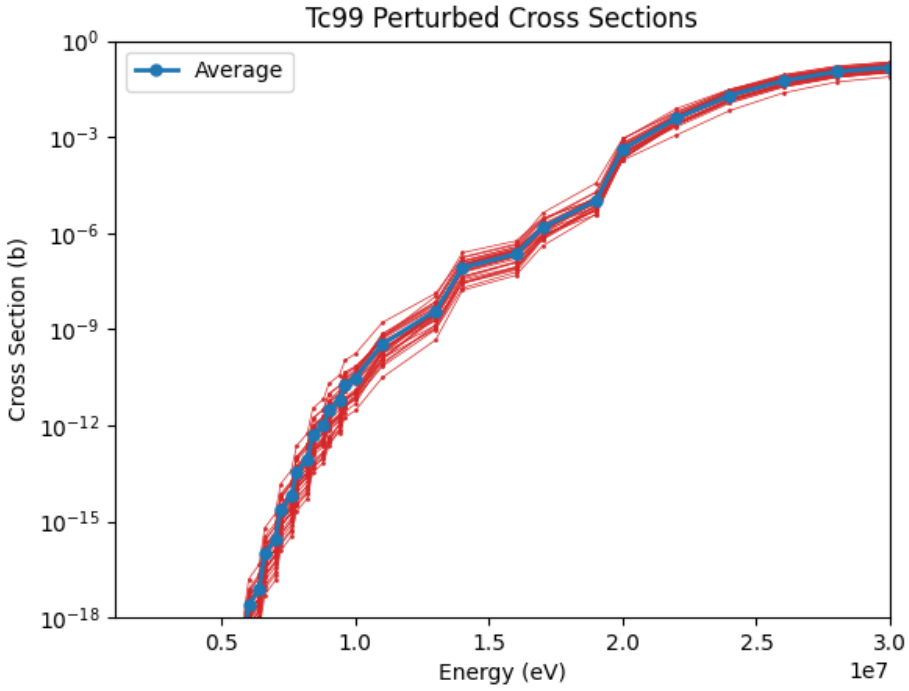

Figure 4.16: Tin-126 Perturbed (p,anything) Cross Section

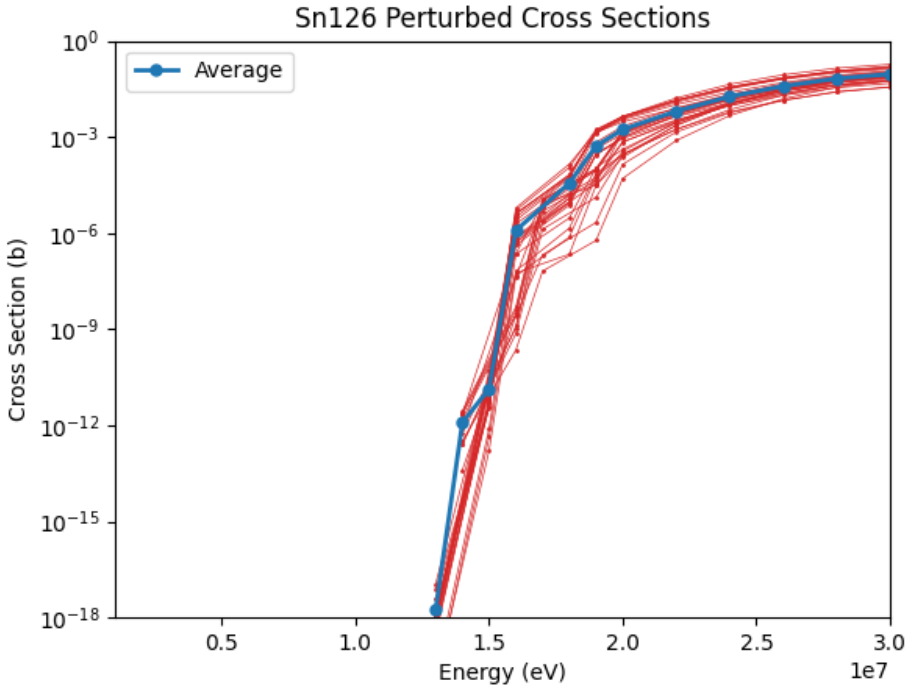

Figure 4.17: Iodine-129 Perturbed (p,anything) Cross Section

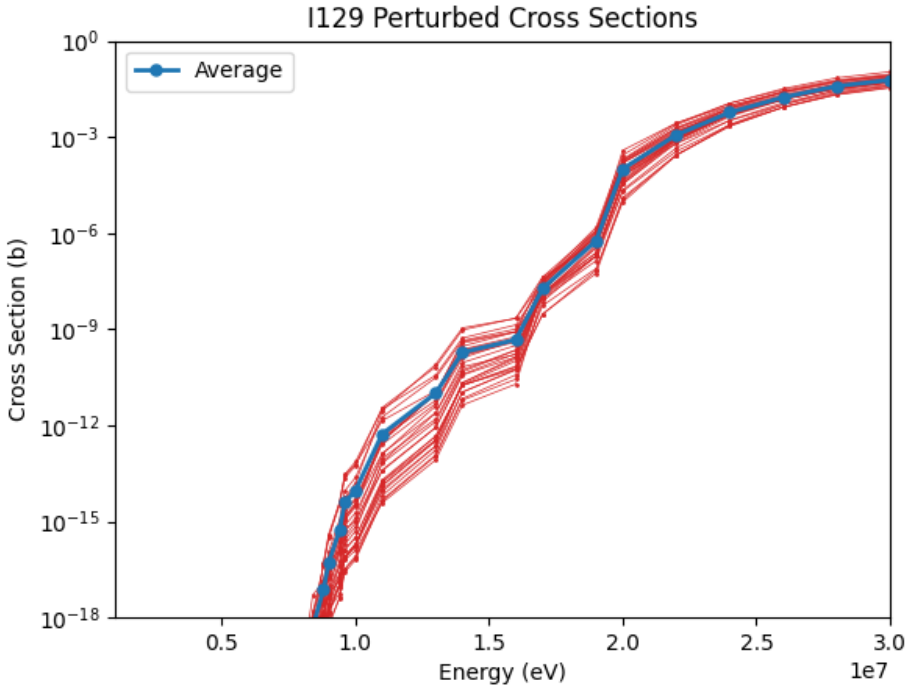

Figure 4.18: Cesium-135 Perturbed (p,anything) Cross Section

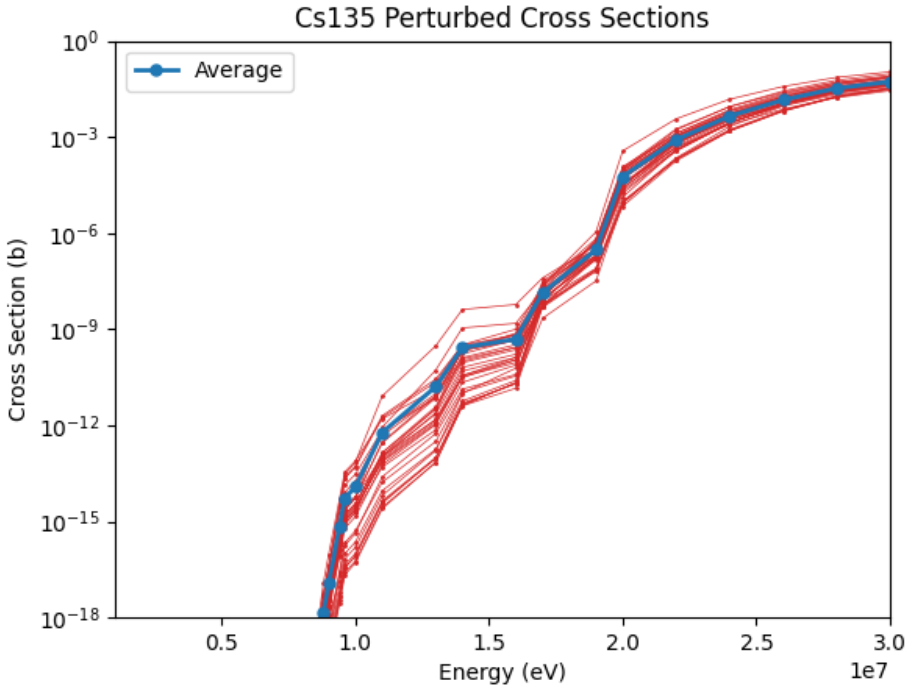

Tables 4.1-4.6 show the average, standard deviation, minimum, and maximum for each cross section value. Perturbed cross section values can range several orders of magnitude, demonstrating the importance of estimating the uncertainty.

Table 4.1: Selenium-79 statistical information for 30 TASMAN perturbed TALYS generated cross sections

Energy (MeV)	**Average (b)**	**SD (b)**	**Min (b)**	**Max (b)**
9.6	7.98×10^{-21}	2.92×10^{-21}	5.55×10^{-21}	1.20×10^{-20}
9.8	9.21×10^{-21}	3.20×10^{-21}	5.18×10^{-21}	1.45×10^{-20}
10	2.37×10^{-20}	1.57×10^{-20}	6.63×10^{-21}	4.80×10^{-20}
11	1.69×10^{-16}	4.18×10^{-16}	1.38×10^{-20}	1.59×10^{-15}
12	1.20×10^{-13}	7.47×10^{-14}	4.92×10^{-17}	2.41×10^{-13}
13	6.98×10^{-13}	1.78×10^{-12}	5.62×10^{-15}	5.97×10^{-12}
14	9.52×10^{-11}	2.13×10^{-10}	3.32×10^{-12}	9.97×10^{-10}
16	1.81×10^{-09}	3.13×10^{-09}	1.02×10^{-10}	1.09×10^{-08}
17	4.73×10^{-08}	5.52×10^{-08}	1.93×10^{-09}	1.96×10^{-07}
19	1.96×10^{-06}	4.90×10^{-06}	1.67×10^{-07}	2.18×10^{-05}
20	9.74×10^{-05}	9.22×10^{-05}	1.41×10^{-06}	3.19×10^{-04}
22	2.41×10^{-03}	9.95×10^{-04}	5.58×10^{-04}	4.67×10^{-03}
24	1.26×10^{-02}	4.65×10^{-03}	3.85×10^{-03}	2.18×10^{-02}
26	3.61×10^{-02}	1.21×10^{-02}	1.47×10^{-02}	6.06×10^{-02}
28	7.28×10^{-02}	2.15×10^{-02}	3.55×10^{-02}	1.19×10^{-01}
30	1.07×10^{-01}	2.89×10^{-02}	5.52×10^{-02}	1.68×10^{-01}

Table 4.2: Zirconium-93 statistical information for 30 TASMAN perturbed TALYS generated cross sections

Energy (MeV)	**Average (b)**	**SD (b)**	**Min (b)**	**Max (b)**
7.8	7.14×10^{-21}	2.13×10^{-21}	5.10×10^{-21}	9.34×10^{-21}
8	2.26×10^{-20}	1.22×10^{-20}	5.27×10^{-21}	4.66×10^{-20}
8.2	3.18×10^{-19}	2.90×10^{-19}	5.42×10^{-20}	8.49×10^{-19}
8.4	5.43×10^{-18}	1.08×10^{-17}	3.63×10^{-19}	5.32×10^{-17}
8.8	1.79×10^{-16}	2.32×10^{-16}	2.70×10^{-17}	6.86×10^{-16}
9	5.05×10^{-16}	9.67×10^{-16}	2.94×10^{-17}	4.95×10^{-15}
9.4	1.19×10^{-14}	1.68×10^{-14}	1.51×10^{-15}	4.89×10^{-14}
9.6	3.72×10^{-14}	8.97×10^{-14}	1.51×10^{-15}	4.57×10^{-13}
10	2.96×10^{-13}	4.37×10^{-13}	2.92×10^{-14}	1.25×10^{-12}
11	3.06×10^{-12}	1.06×10^{-11}	2.70×10^{-14}	5.31×10^{-11}
13	5.47×10^{-10}	6.92×10^{-10}	8.90×10^{-11}	2.06×10^{-09}
14	1.41×10^{-09}	2.53×10^{-09}	9.65×10^{-11}	1.16×10^{-08}
16	5.15×10^{-08}	2.98×10^{-08}	1.75×10^{-08}	1.02×10^{-07}
17	6.78×10^{-07}	1.87×10^{-06}	3.45×10^{-08}	8.70×10^{-06}
19	4.99×10^{-04}	3.02×10^{-04}	5.08×10^{-05}	1.10×10^{-03}
20	1.73×10^{-03}	1.06×10^{-03}	1.28×10^{-04}	4.10×10^{-03}
22	7.49×10^{-03}	3.16×10^{-03}	2.67×10^{-03}	1.54×10^{-02}
24	2.34×10^{-02}	8.15×10^{-03}	1.14×10^{-02}	4.36×10^{-02}
26	5.28×10^{-02}	1.60×10^{-02}	2.82×10^{-02}	9.15×10^{-02}
28	9.52×10^{-02}	2.63×10^{-02}	5.38×10^{-02}	1.57×10^{-01}
30	1.36×10^{-01}	3.55×10^{-02}	7.63×10^{-02}	2.17×10^{-01}

Table 4.3: Technetium-99 statistical information for 30 TASMAN perturbed TALYS generated cross sections

Energy (MeV)	**Average (b)**	**SD (b)**	**Min (b)**	**Max (b)**
6.6	9.90×10^{-17}	1.27×10^{-16}	5.12×10^{-18}	6.22×10^{-16}
7	2.79×10^{-16}	3.61×10^{-16}	1.46×10^{-17}	1.77×10^{-15}
7.2	2.31×10^{-15}	3.03×10^{-15}	1.24×10^{-16}	1.48×10^{-14}
7.6	6.17×10^{-15}	8.12×10^{-15}	3.39×10^{-16}	3.97×10^{-14}
7.8	3.64×10^{-14}	4.82×10^{-14}	2.14×10^{-15}	2.36×10^{-13}
8.2	8.65×10^{-14}	1.15×10^{-13}	5.23×10^{-15}	5.63×10^{-13}
8.4	5.20×10^{-13}	6.99×10^{-13}	3.38×10^{-14}	3.41×10^{-12}
8.8	1.00×10^{-12}	1.34×10^{-12}	6.86×10^{-14}	6.54×10^{-12}
9	3.06×10^{-12}	4.04×10^{-12}	2.25×10^{-13}	1.98×10^{-11}
9.4	5.94×10^{-12}	7.45×10^{-12}	5.91×10^{-13}	3.72×10^{-11}
9.6	1.79×10^{-11}	2.06×10^{-11}	1.75×10^{-12}	1.06×10^{-10}
10	3.04×10^{-11}	3.35×10^{-11}	2.94×10^{-12}	1.73×10^{-10}
11	3.40×10^{-10}	3.11×10^{-10}	3.10×10^{-11}	1.62×10^{-09}
13	3.77×10^{-09}	2.87×10^{-09}	4.66×10^{-10}	1.32×10^{-08}
14	8.39×10^{-08}	5.34×10^{-08}	1.64×10^{-08}	2.45×10^{-07}
16	2.23×10^{-07}	1.31×10^{-07}	4.79×10^{-08}	5.70×10^{-07}
17	1.49×10^{-06}	8.24×10^{-07}	4.01×10^{-07}	4.22×10^{-06}
19	1.04×10^{-05}	6.29×10^{-06}	3.76×10^{-06}	3.65×10^{-05}
20	4.16×10^{-04}	2.01×10^{-04}	1.87×10^{-04}	9.02×10^{-04}
22	3.82×10^{-03}	1.40×10^{-03}	1.14×10^{-03}	7.64×10^{-03}
24	1.97×10^{-02}	6.16×10^{-03}	6.68×10^{-03}	3.07×10^{-02}
26	5.69×10^{-02}	1.62×10^{-02}	2.37×10^{-02}	8.78×10^{-02}
28	1.09×10^{-01}	2.85×10^{-02}	5.20×10^{-02}	1.63×10^{-01}
30	1.50×10^{-01}	3.69×10^{-02}	7.60×10^{-02}	2.18×10^{-01}

Table 4.4: Tin-126 statistical information for 30 TASMAN perturbed TALYS generated cross sections

Energy (MeV)	**Average (b)**	**SD (b)**	**Min (b)**	**Max (b)**
13	1.79×10^{-18}	2.90×10^{-18}	9.33×10^{-21}	1.14×10^{-17}
14	1.23×10^{-12}	1.04×10^{-12}	4.04×10^{-14}	2.85×10^{-12}
15	1.38×10^{-11}	1.38×10^{-11}	1.63×10^{-13}	5.21×10^{-11}
16	1.22×10^{-06}	1.78×10^{-06}	2.24×10^{-10}	6.12×10^{-06}
18	3.63×10^{-05}	4.00×10^{-05}	2.18×10^{-07}	1.43×10^{-04}
19	5.23×10^{-04}	6.14×10^{-04}	5.91×10^{-07}	1.73×10^{-03}
20	1.72×10^{-03}	1.48×10^{-03}	5.10×10^{-05}	4.41×10^{-03}
22	6.39×10^{-03}	4.47×10^{-03}	7.78×10^{-04}	1.64×10^{-02}
24	1.82×10^{-02}	1.05×10^{-02}	4.66×10^{-03}	4.43×10^{-02}
26	3.86×10^{-02}	1.90×10^{-02}	1.38×10^{-02}	8.72×10^{-02}
28	6.68×10^{-02}	2.93×10^{-02}	2.54×10^{-02}	1.41×10^{-01}
30	9.15×10^{-02}	3.78×10^{-2}	3.58×10^{-02}	1.85×10^{-01}

Table 4.5: Iodine-129 statistical information for 30 TASMAN perturbed TALYS generated cross sections

Energy (MeV)	**Average (b)**	**SD (b)**	**Min (b)**	**Max (b)**
7.8	3.53×10^{-20}	3.11×10^{-20}	1.06×10^{-20}	1.19×10^{-19}
8.2	6.82×10^{-20}	9.11×10^{-20}	1.16×10^{-20}	3.92×10^{-19}
8.4	5.02×10^{-19}	9.63×10^{-19}	1.52×10^{-20}	5.14×10^{-18}
8.8	7.31×10^{-18}	1.37×10^{-17}	8.01×10^{-20}	5.12×10^{-17}
9	5.37×10^{-17}	1.075×10^{-16}	5.19×10^{-19}	4.08×10^{-16}
9.4	5.23×10^{-16}	1.10×10^{-15}	3.80×10^{-18}	3.95×10^{-15}
9.6	3.89×10^{-15}	8.02×10^{-15}	2.62×10^{-17}	2.96×10^{-14}
10	9.42×10^{-15}	1.92×10^{-14}	6.41×10^{-17}	7.31×10^{-14}
11	5.39×10^{-13}	1.00×10^{-12}	3.83×10^{-15}	3.59×10^{-12}
13	1.01×10^{-11}	1.93×10^{-11}	8.34×10^{-14}	8.00×10^{-11}
14	1.89×10^{-10}	2.72×10^{-10}	4.28×10^{-12}	1.10×10^{-09}
16	4.72×10^{-10}	5.78×10^{-10}	1.95×10^{-11}	2.21×10^{-09}
17	1.86×10^{-08}	1.09×10^{-08}	2.90×10^{-09}	4.26×10^{-08}
19	5.76×10^{-07}	3.94×10^{-07}	5.54×10^{-08}	1.51×10^{-06}
20	1.02×10^{-04}	8.56×10^{-05}	9.32×10^{-06}	3.84×10^{-04}
22	1.15×10^{-03}	6.68×10^{-04}	2.67×10^{-04}	2.71×10^{-03}
24	5.83×10^{-03}	2.47×10^{-03}	2.17×10^{-03}	1.13×10^{-02}
26	1.74×10^{-02}	6.00×10^{-03}	8.43×10^{-03}	3.22×10^{-02}
28	3.85×10^{-02}	1.17×10^{-02}	2.08×10^{-02}	6.99×10^{-02}
30	6.04×10^{-02}	1.72×10^{-02}	3.41×10^{-02}	1.09×10^{-01}

Table 4.6: Cesium-135 statistical information for 30 TASMAN perturbed TALYS generated cross sections

Energy (MeV)	Average (b)	SD (b)	Min (b)	Max (b)
8.4	3.17×10^{-20}	2.57×10^{-20}	1.06×10^{-20}	1.03×10^{-19}
8.8	1.48×10^{-18}	2.55×10^{-18}	1.63×10^{-20}	1.20×10^{-17}
9	1.16×10^{-17}	2.05×10^{-17}	6.05×10^{-20}	9.59×10^{-17}
9.4	6.89×10^{-16}	1.22×10^{-15}	2.73×10^{-18}	4.90×10^{-15}
9.6	5.28×10^{-15}	9.38×10^{-15}	2.16×10^{-17}	3.52×10^{-14}
10	1.23×10^{-14}	2.20×10^{-14}	5.18×10^{-17}	7.84×10^{-14}
11	5.98×10^{-13}	1.53×10^{-12}	2.51×10^{-15}	8.20×10^{-12}
13	1.61×10^{-11}	5.49×10^{-11}	6.93×10^{-14}	3.01×10^{-10}
14	2.66×10^{-10}	7.61×10^{-10}	4.06×10^{-12}	4.14×10^{-09}
16	4.92×10^{-10}	1.08×10^{-09}	1.45×10^{-11}	5.92×10^{-09}
17	1.35×10^{-08}	8.89×10^{-09}	2.19×10^{-09}	3.99×10^{-08}
19	3.02×10^{-07}	2.33×10^{-07}	3.22×10^{-08}	1.09×10^{-06}
20	5.81×10^{-05}	6.75×10^{-05}	6.94×10^{-06}	3.68×10^{-04}
22	8.17×10^{-04}	6.91×10^{-04}	1.80×10^{-04}	3.69×10^{-03}
24	4.49×10^{-03}	2.82×10^{-03}	1.53×10^{-03}	1.51×10^{-02}
26	1.43×10^{-02}	6.94×10^{-03}	6.37×10^{-03}	3.76×10^{-02}
28	3.30×10^{-02}	1.32×10^{-02}	1.69×10^{-02}	7.26×10^{-02}
30	5.34×10^{-02}	1.94×10^{-02}	2.80×10^{-02}	1.08×10^{-01}

4.1.3 Proton Flux Calculations

FISPACT does not consider the geometry of the target when performing depletion calculations. Therefore, the attenuation of the proton beam as it passes through the target will not be accurately captured. Simulations of LLFP irradiation are run in elemental targets containing all the isotopes of the same element produced in nuclear reactors. Isotope separation is a complex process that is not considered in this thesis. Technetium-99 is the only LLFP irradiated in isolation as it is the only isotope of Technetium found in spent fuel. PHITS is used to determine the beam's penetration depth and flux energy spectrum for each LLFP. Figure 4.19 shows the source normalized flux through an elemental selenium target, and Figure 4.20 shows the flux-energy spectrum in an elemental selenium target. Both figures were generated using PHITS in the work supporting this thesis[19]. This variation in beam flux must be captured to model LLFPs' transmutation accurately.

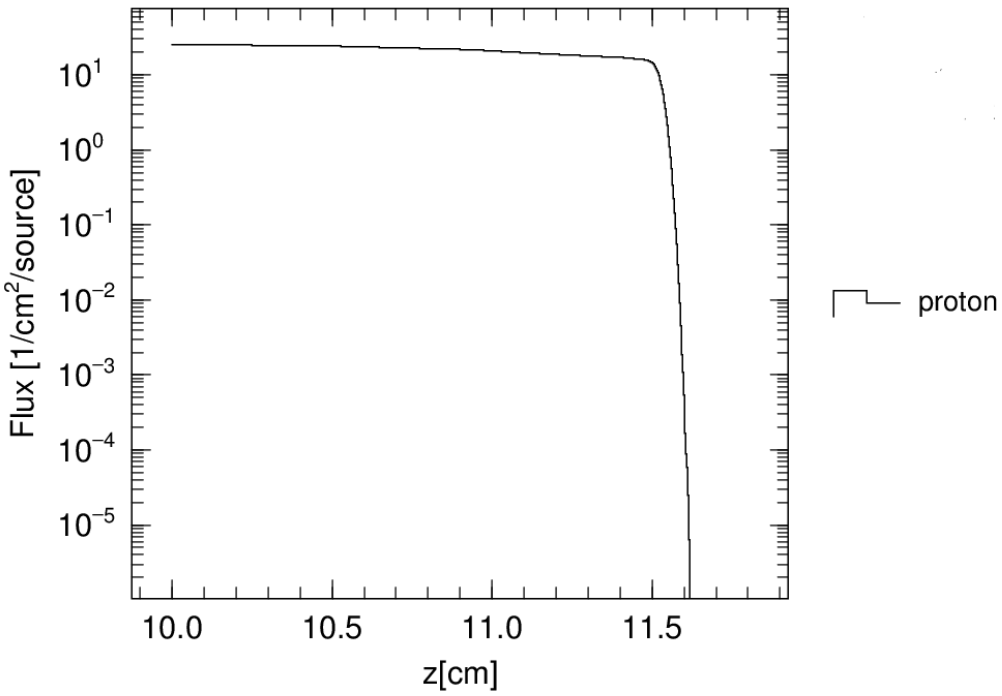

Figure 4.19: The flux of the beam remains approximately constant before dropping sharply at the penetration depth, from work supporting this thesis[19].

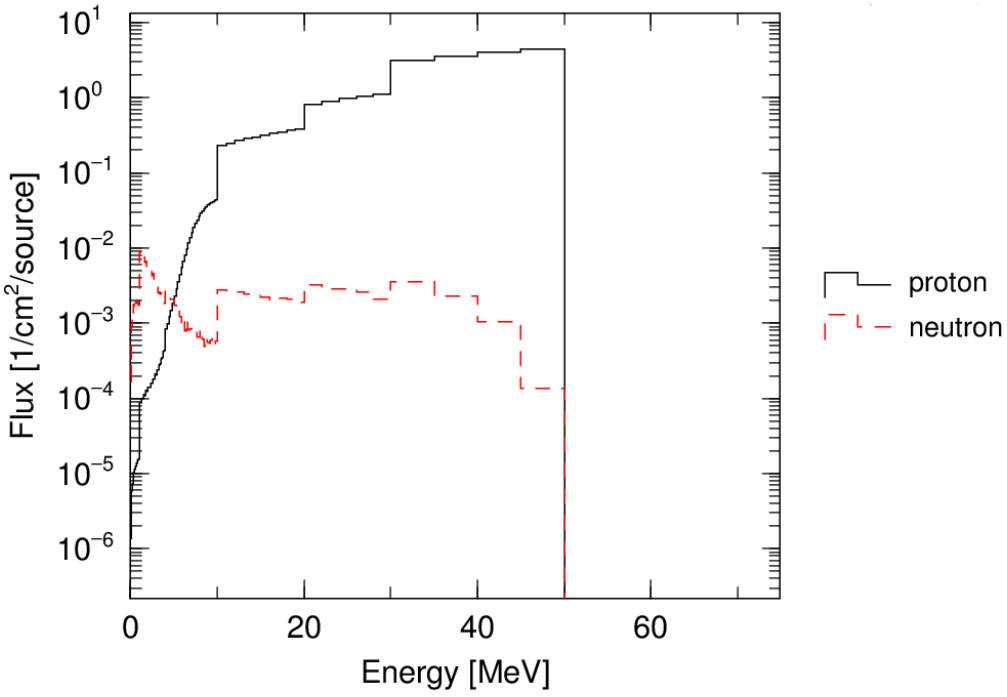

Figure 4.20: Flux-energy spectrum through an elemental selenium target of a 50 MeV proton beam from work supporting this thesis[19].

The penetration depth and density of the target material will be used to calculate the number of target particles irradiated by the incident proton beam. This number of particles will then be used as an input for the FISPACT depletion calculation. Table 4.7 shows the penetration depth of the proton beam for each elemental target. The penetration depth was determined from the distance where the flux of the incident proton beam becomes essentially zero within the target material in the work supporting this thesis [19].

Table 4.7: Target materials and their corresponding PHITS calculated proton penetration depth for elemental targets[19].

Target	**18 MeV**	**23 MeV**	**30 MeV**	**50 MeV**	**70 MeV**
Se	0.075cm	0.159cm	0.304cm	0.862cm	1.617cm
Zr	0.051cm	0.109cm	0.208cm	0.575cm	1.079cm
Tc	0.03cm	0.063cm	0.119cm	0.333cm	0.613cm
Sn	0.055cm	0.115cm	0.218cm	0.596cm	1.112cm
CsI	0.081cm	0.175cm	0.327cm	0.916cm	1.715cm

The number of nuclides exposed to the proton beam before the flux becomes essentially zero was calculated with the following equation:

$$N = \Delta x \frac{\rho N_A}{A} \pi R^2 \tag{4.1}$$

where Δx is the penetration depth, ρ is the density, N_A is Avagadro's Number, A is the atomic mass number, and R is the radius of the proton beam. For this calculation, the radius was assumed to be 0.1 cm.

The number of total nuclides irradiated per elemental target calculated from Equation 4.1 is shown in Table 4.8. This number includes all isotopes present in the elemental target, not just the target LLFP. Table 4.9 shows just the number of LLFP isotopes irradiated by the proton beam.

Table 4.8: Target materials and their corresponding number of nuclides irradiated by the proton beam at various energies[19].

Target	**18 MeV**	**23 MeV**	**30 MeV**	**50 MeV**	**70 MeV**
Se	5.2443×10^{19}	1.13303×10^{20}	2.11714×10^{20}	5.9306×10^{20}	1.11037×10^{21}
Zr	6.72262×10^{19}	1.43679×10^{20}	2.74177×10^{20}	7.57942×10^{20}	1.42229×10^{21}
Tc	6.59912×10^{19}	1.38582×10^{20}	2.61765×10^{20}	7.32502×10^{20}	1.34842×10^{21}
Sn	5.90523×10^{19}	1.23473×10^{20}	2.34062×10^{20}	6.39913×10^{20}	1.19393×10^{21}
CsI	5.2443×10^{19}	1.13303×10^{20}	2.11714×10^{20}	5.9306×10^{20}	1.11037×10^{21}

Table 4.9: Amount of each LLFP isotope within the elemental target irradiated by the proton beam [19].

Isotope	**18 MeV**	**23 MeV**	**30 MeV**	**50 MeV**	**70 MeV**
Se79	1.07308×10^{19}	2.27494×10^{19}	4.34957×10^{19}	1.23333×10^{20}	2.31357×10^{20}
Zr93	1.36763×10^{19}	2.92298×10^{19}	5.5778×10^{19}	1.54194×10^{20}	2.89348×10^{20}
Tc99	6.59912×10^{19}	1.38582×10^{20}	2.61765×10^{20}	7.32502×10^{20}	1.34842×10^{21}
Sn126	1.68617×10^{19}	3.52562×10^{19}	6.68335×10^{19}	1.82719×10^{20}	3.40912×10^{20}
I129	1.92986×10^{19}	4.16944×10^{19}	7.7909×10^{19}	2.1824×10^{20}	4.08605×10^{20}
Cs135	9.72738×10^{18}	2.10159×10^{19}	3.92698×10^{19}	1.10003×10^{20}	2.05956×10^{20}

Although Technetium-99 has the smallest penetration depth, it has the largest number of nuclides irradiated by the proton beam due to a high density of 11.5 g/cm^3 and the target lacking any other isotopes of Technetium. Cesium-135 has the least number of nuclides irradiated by the proton beam. This is most likely because Cesium-Iodine has a low density of 4.3 g/cm^3, and many other isotopes are present within the target, preventing more Cesium-135 from being irradiated. The depletion calculation also includes the impact of competing isotopes in elemental targets, which will be discussed in the next section. Isotope separation could allow for more significant amounts of nuclides to be irradiated by the beam, but it would require a very involved process outside of the scope of this work.

4.1.4 Depletion Calculation

The parameters that have the most significant effect on the amount of transmutation of the target LLFP are the energy of the proton beam, flux of the proton beam, irradiation time, and number of nuclides irradiated. The flux of the beam and the number of nuclides are constrained by the penetration depth of the beam, which is calculated using PHITS. For energy (Figures 4.21-4.26) and irradiation time (Figures 4.27-4.32) of the proton beam, FISPACT simulations were run to determine the parameters that led to the largest transmutation of the target LLFP. Each LLFP was run using an elemental isotopic composition of the element except for Technetium which has no other isotopes produced in spent fuel. Cesium and Iodine were run together in a compound. Although the target was composed of multiple isotopes, only the depletion of the LLFP isotope was plotted and analyzed. The graphs below show the difference between the number of target LLFP nuclides in an unirradiated sample and an irradiated sample of the same initial mass. For different beam energies, the initial masses differ as a higher energy proton beam penetrates deeper into the target material, therefore irradiating more nuclides. For all LLFPs, longer irradiation time led to more significant transmutation. Therefore, in all subsequent analyses, trials are performed using 50 hours of irradiation (0.0057 years). For all LLFPs, except for Selenium-79, a 70 MeV proton beam led to the most significant transmutation. For Se79, a 50 MeV proton beam led to the largest transmutation of the target isotope. This is most likely due to a difference in the cross section of Selenium-79 compared to the other heavier LLFPs. For simulations involving Zirconium-93, Technetium-99, Tin-126, Iodine-129, and Cesium-135, a 70 MeV proton beam is used, while for Selenium-79, a 50 MeV proton beam is used. An

example input file of the FISPACT inventory calculation for elemental Selenium is shown in Listing A.1.

Figure 4.21: Selenium-79 energy optimization for 50 hours of irradiation

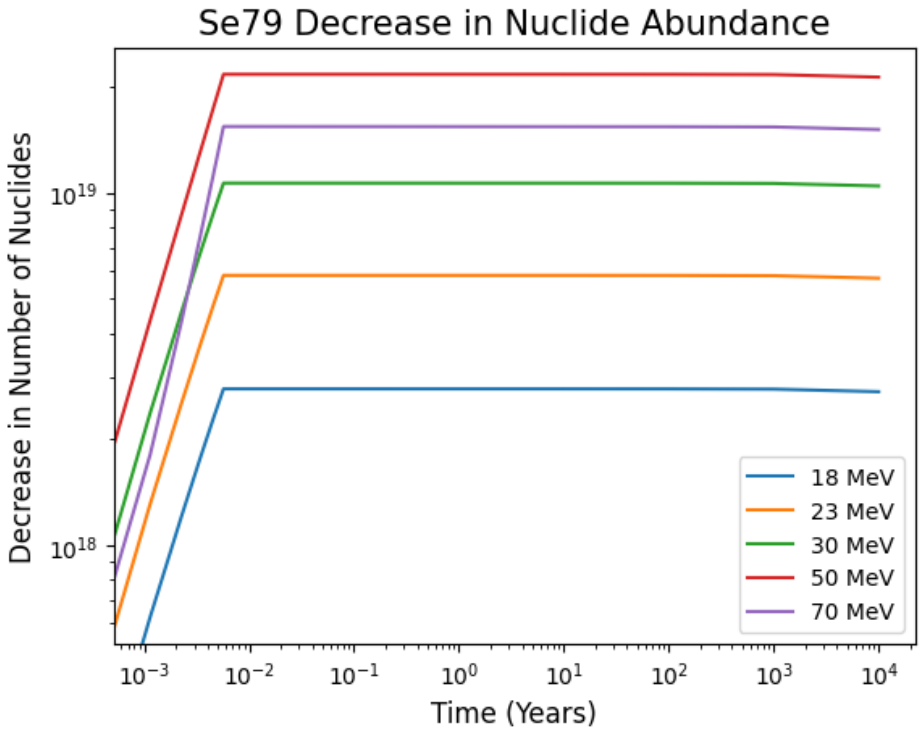

Figure 4.22: Zirconium-93 energy optimization for 50 hours of irradiation

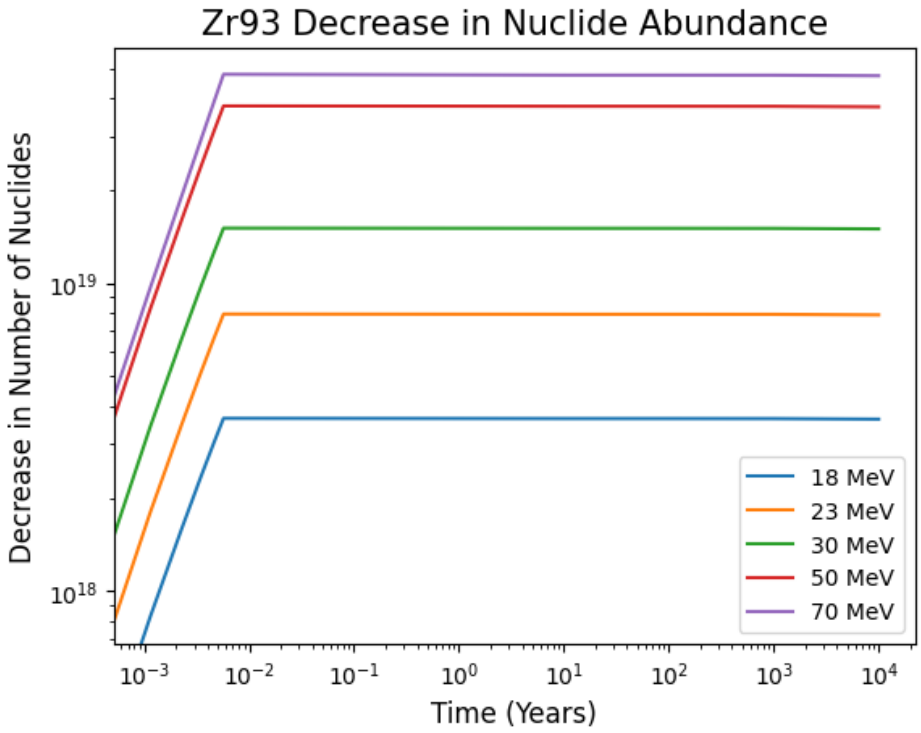

Figure 4.23: Technetium-99 energy optimization for 50 hours of irradiation

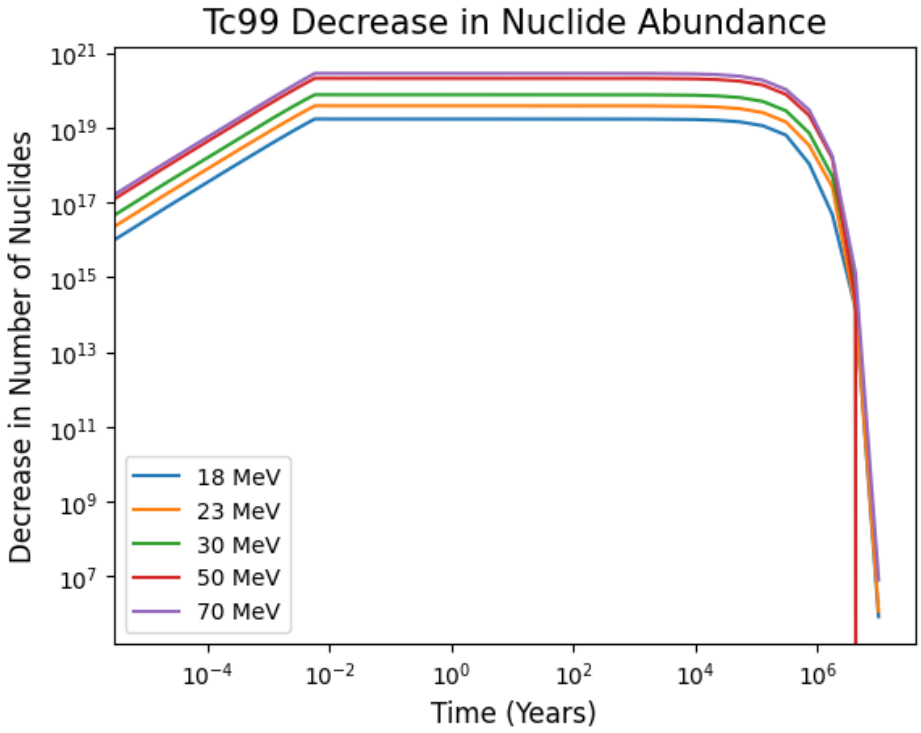

Figure 4.24: Tin-126 energy optimization for 50 hours of irradiation

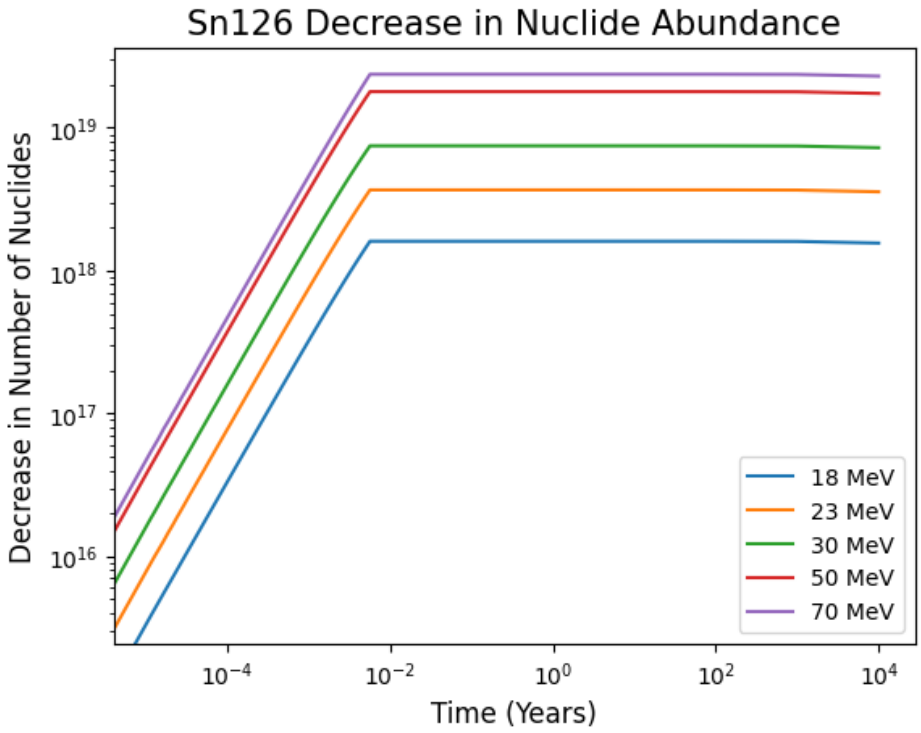

Figure 4.25: Iodine-129 energy optimization for 50 hours of irradiation

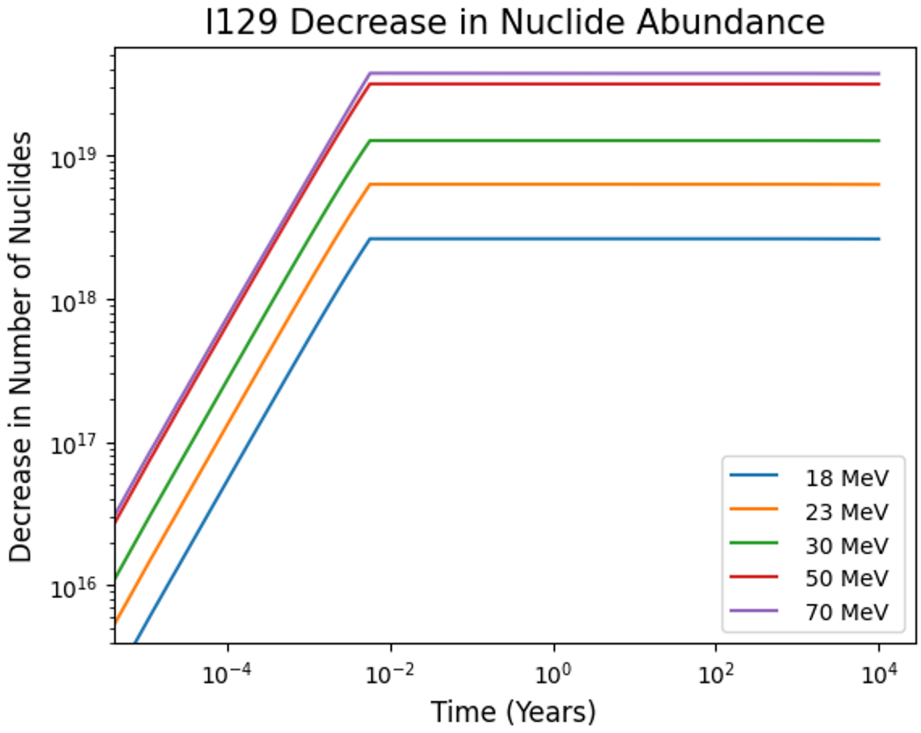

Figure 4.26: Cesium-135 energy optimization for 50 hours of irradiation

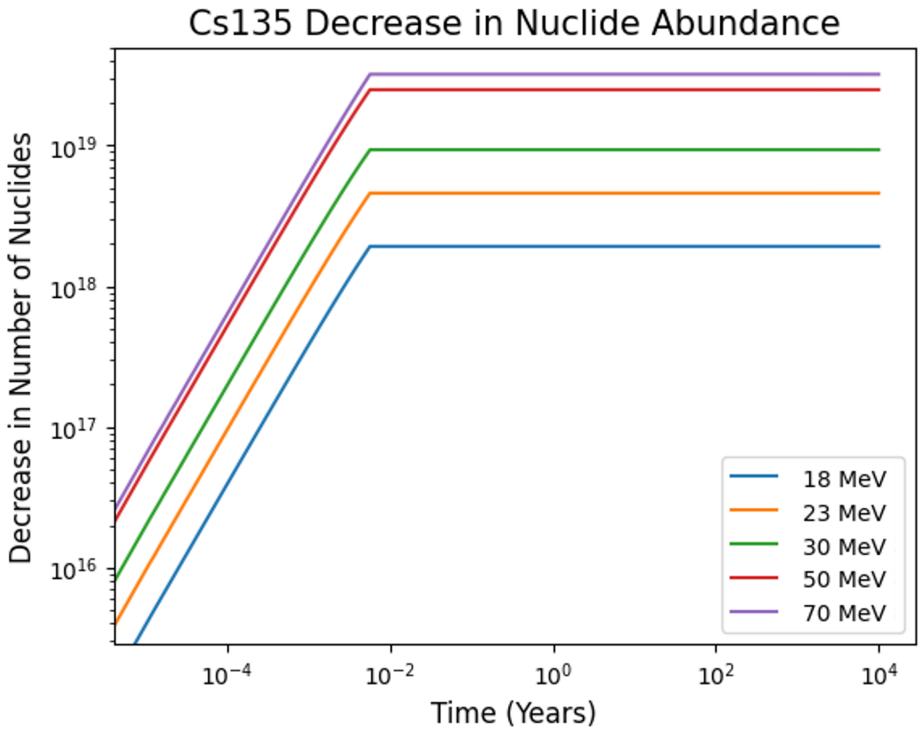

Figure 4.27: Selenium-79 irradiation time optimization for 50 MeV proton beam

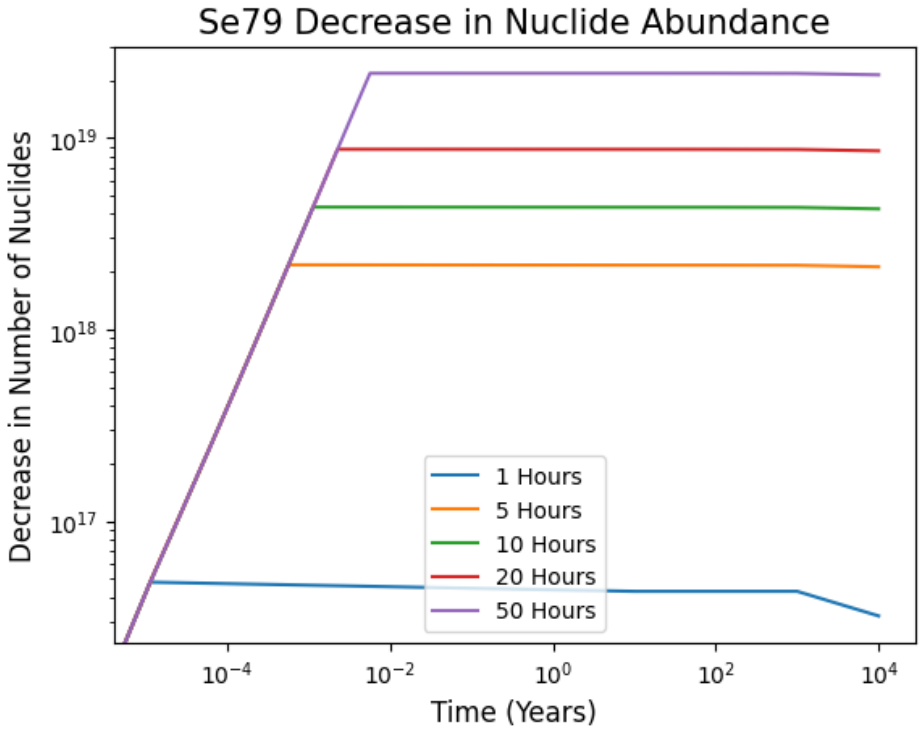

Figure 4.28: Zirconium-93 irradiation time optimization for 70 MeV proton beam

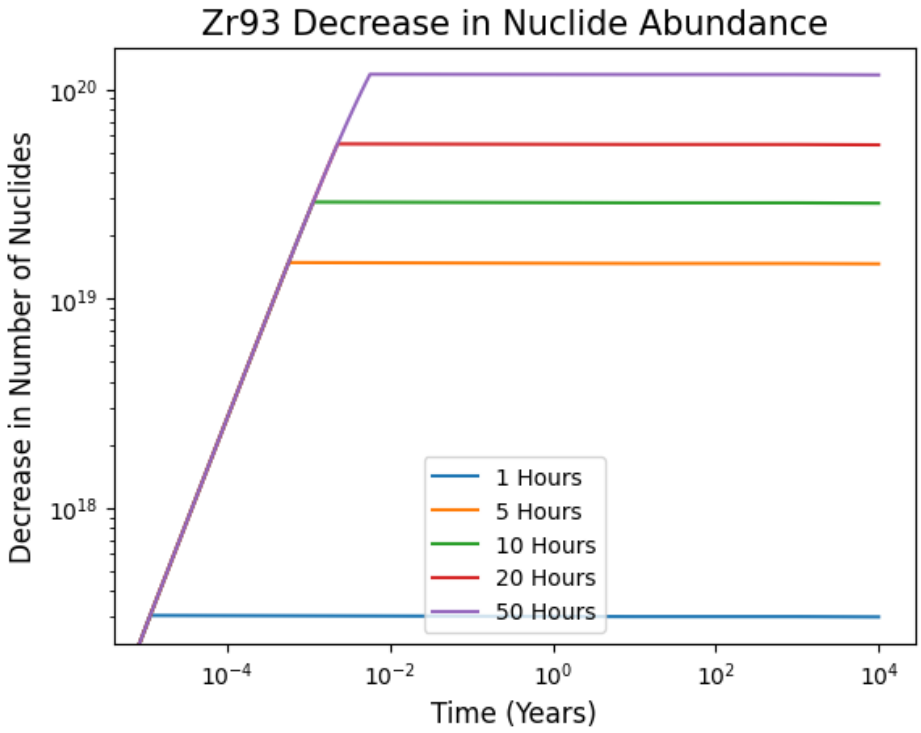

Figure 4.29: Technetium-99 irradiation time optimization for 70 MeV proton beam

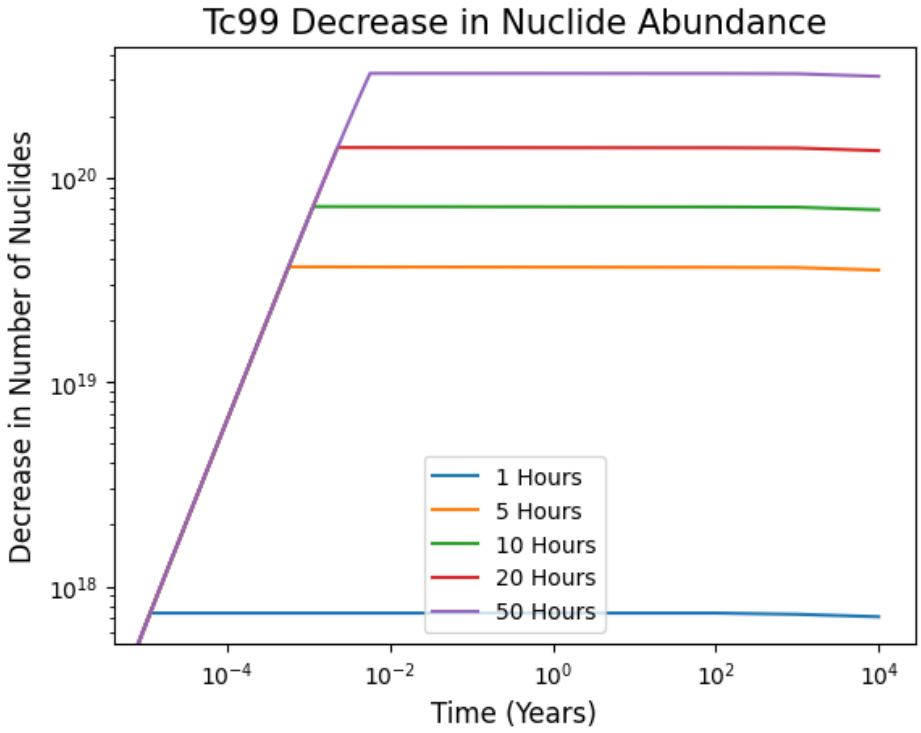

Figure 4.30: Tin-126 irradiation time optimization for a 70 MeV proton beam

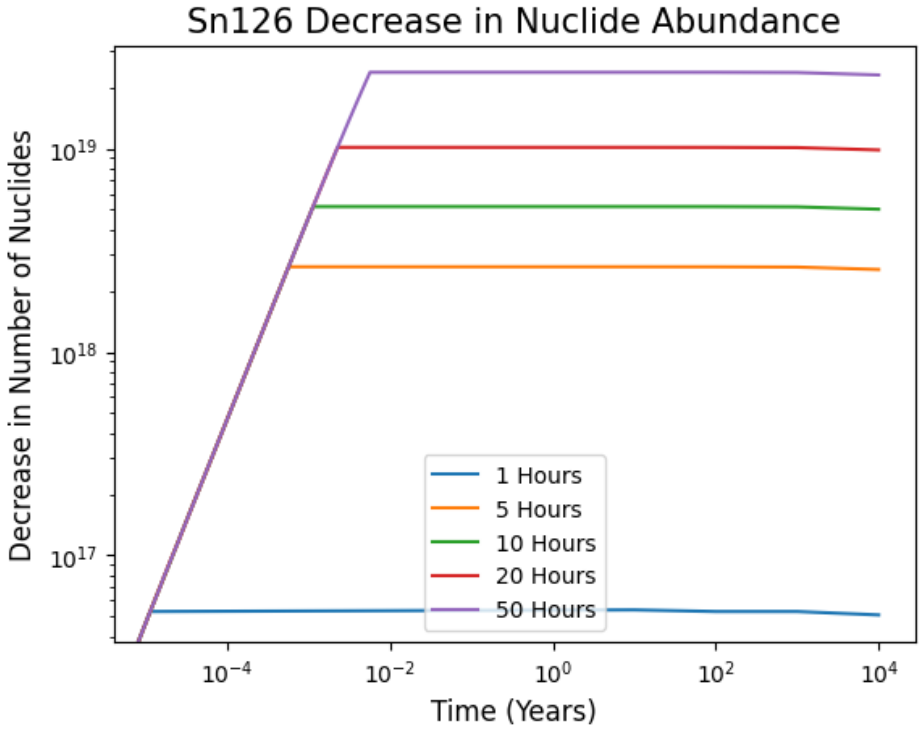

Figure 4.31: Iodine-129 energy optimization for 70 MeV of irradiation

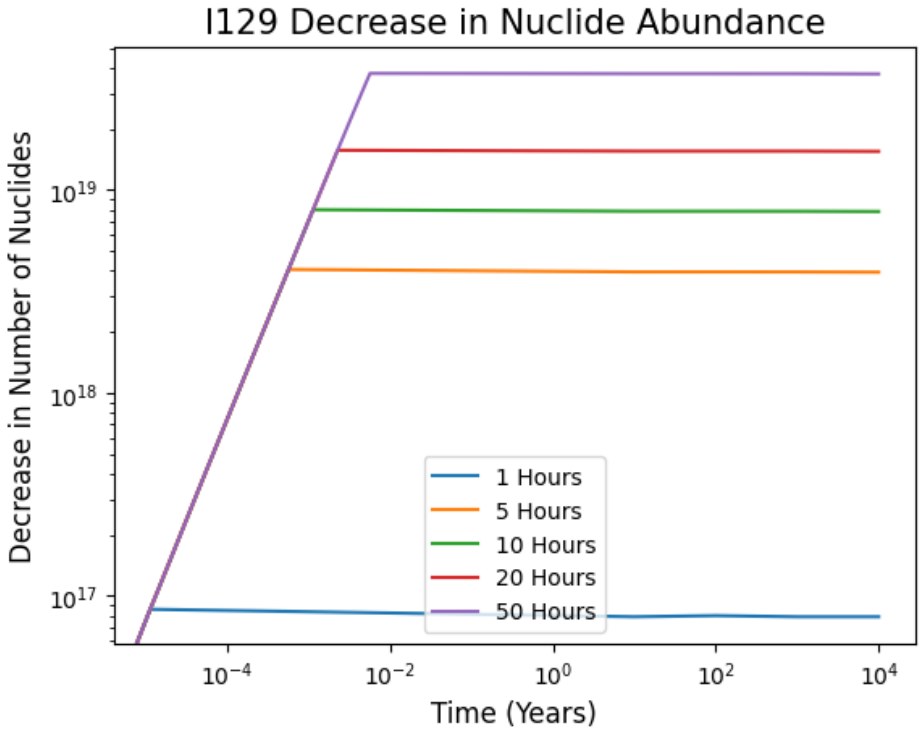

Figure 4.32: Cesium-135 energy optimization for 70 MeV of irradiation

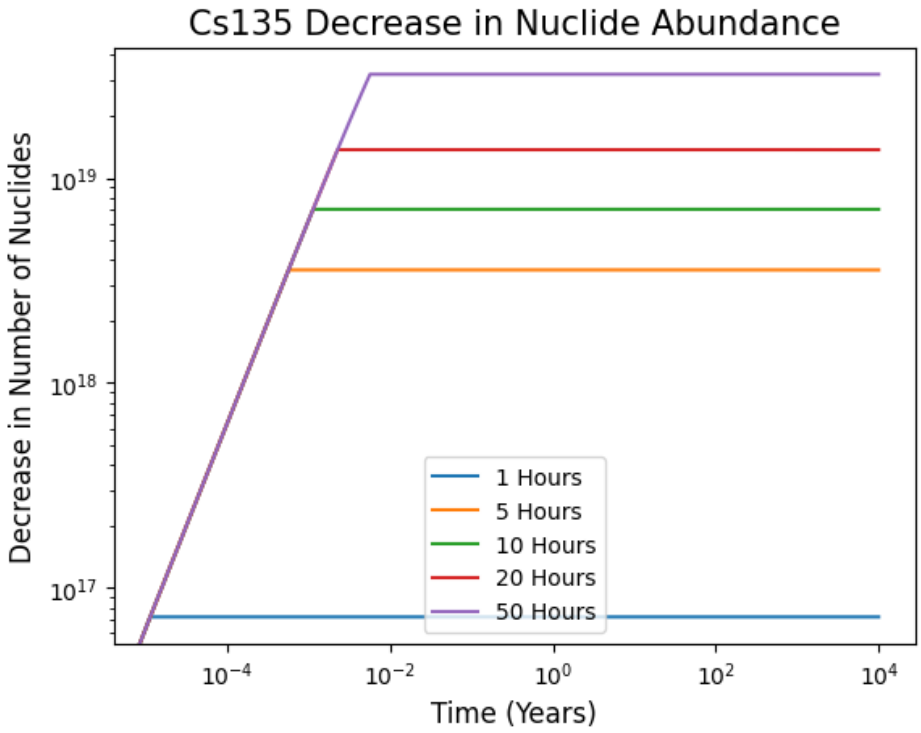

Once the optimal irradiation conditions for each LLFP isotope were determined, the 30 perturbed cross sections were used as inputs for FISPACT depletion calculations. Figures 4.33-4.38 show the number of atoms over time from irradiating elemental targets for each LLFP. FISPACT results for each perturbed sample are plotted in red, the average value for each energy is plotted in blue, and the non-irradiated amount of nuclides is shown with a dashed blue line. Although the irradiation targets consisted of multiple isotopes of each element, only the perturbed cross section for the LLFP of interest was used.

Figure 4.33: Selenium-79 irradiation depletion for 30 TALYS perturbed cross sections

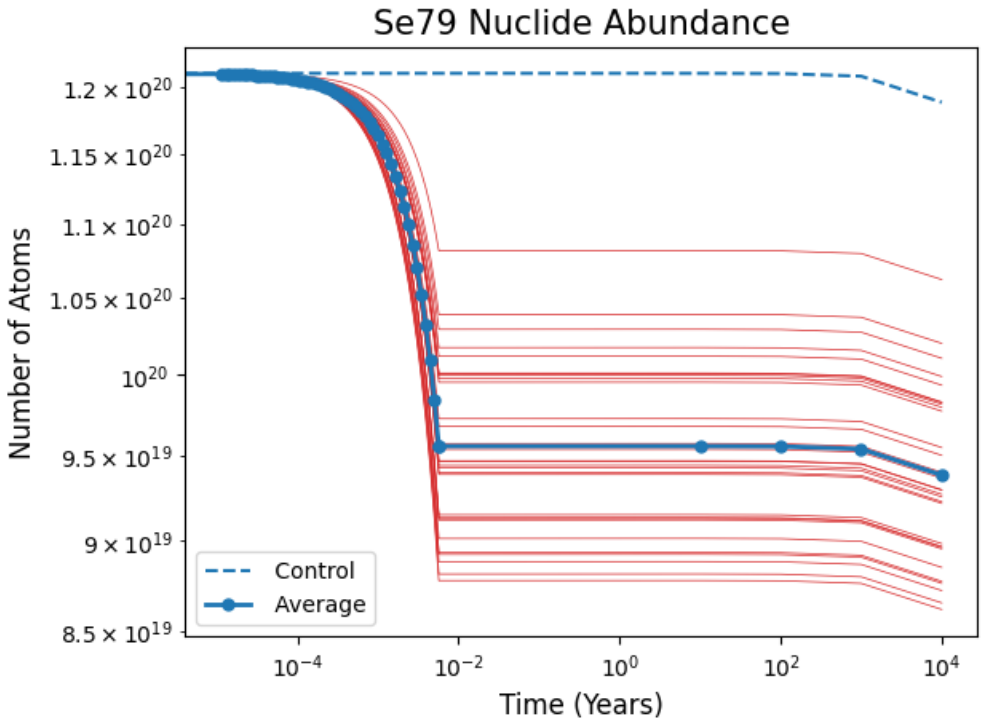

Figure 4.34: Zirconium-93 irradiation depletion for 30 TALYS perturbed cross sections

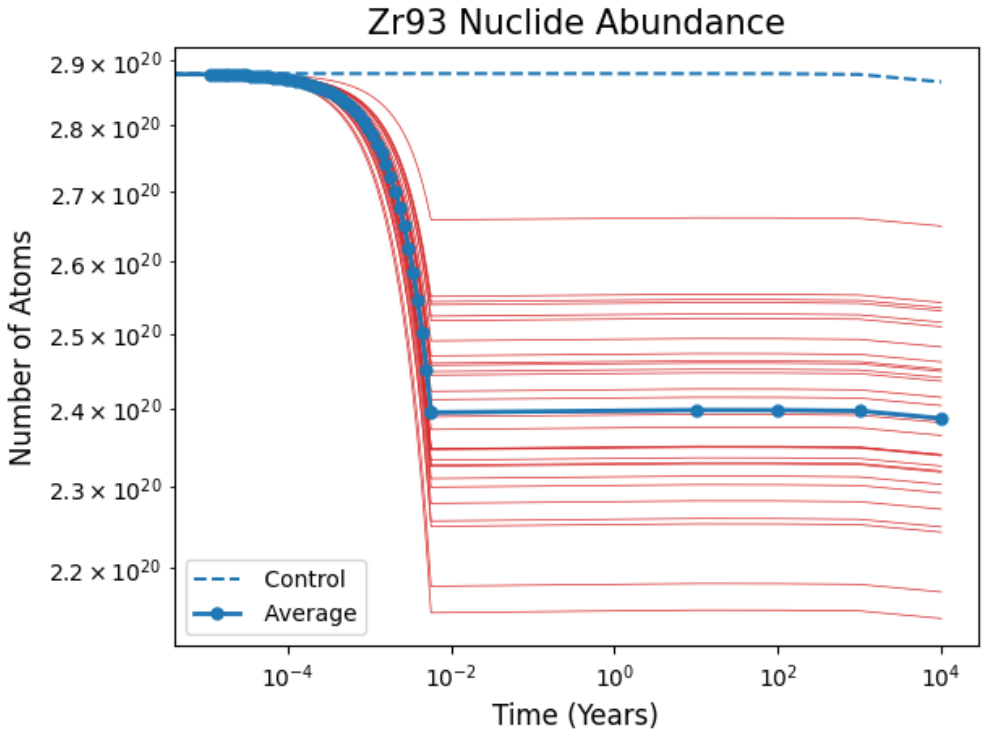

Figure 4.35: Technetium-99 irradiation depletion for 30 TALYS perturbed cross sections

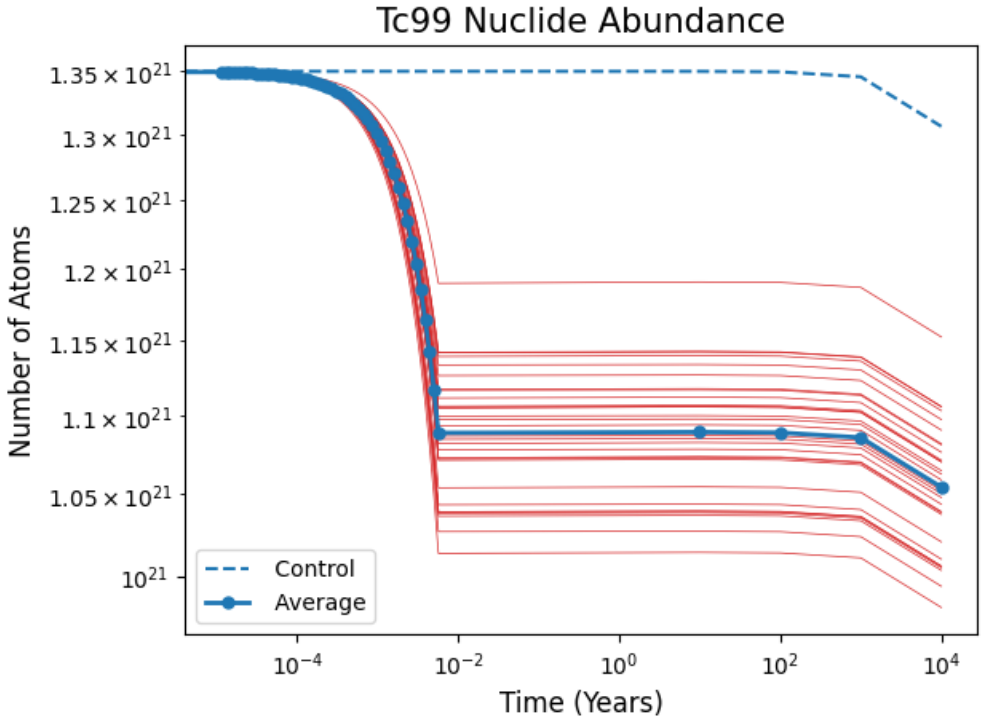

Figure 4.36: Tin-126 irradiation depletion for 30 TALYS perturbed cross sections

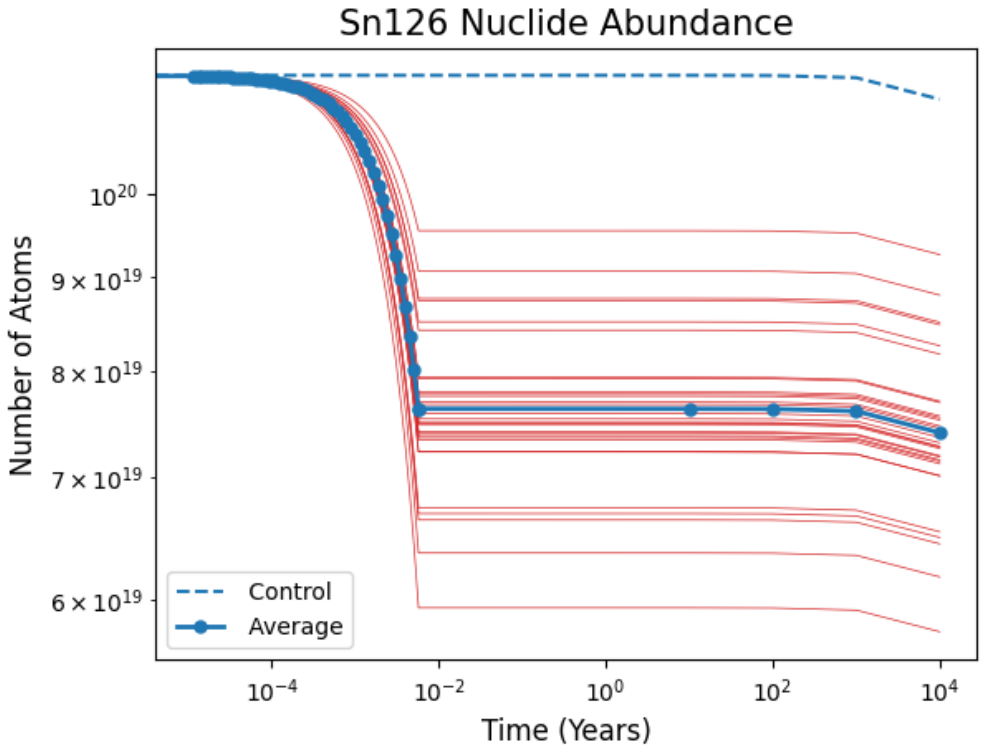

Figure 4.37: Iodine-129 irradiation depletion for 30 TALYS perturbed cross sections

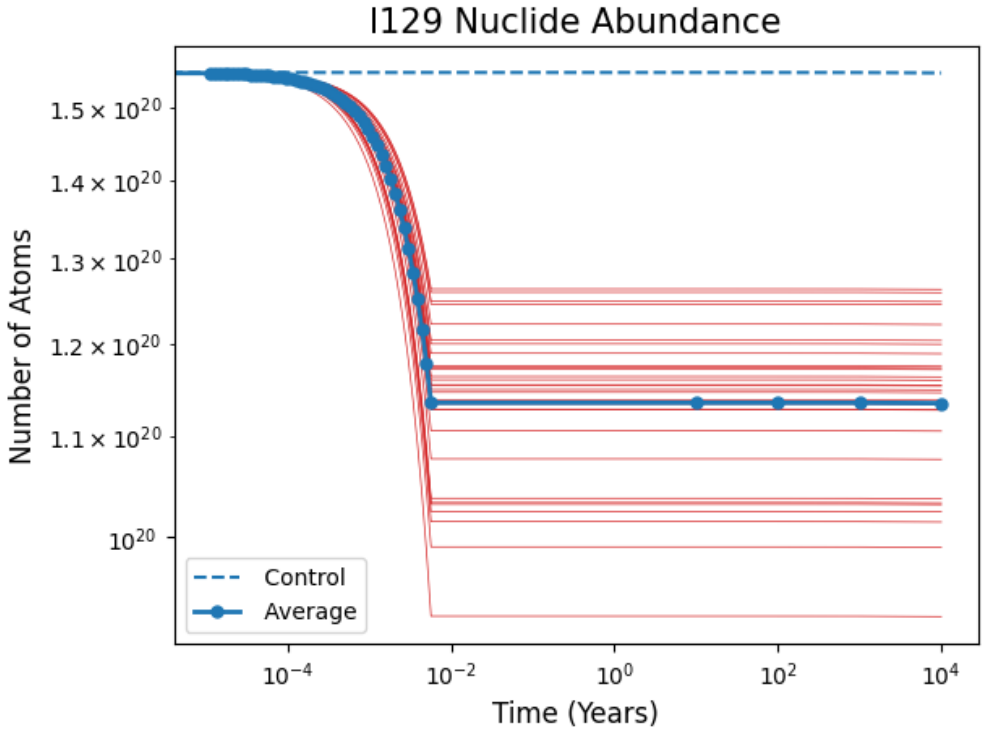

Figure 4.38: Cesium-135 irradiation depletion for 30 TALYS perturbed cross sections

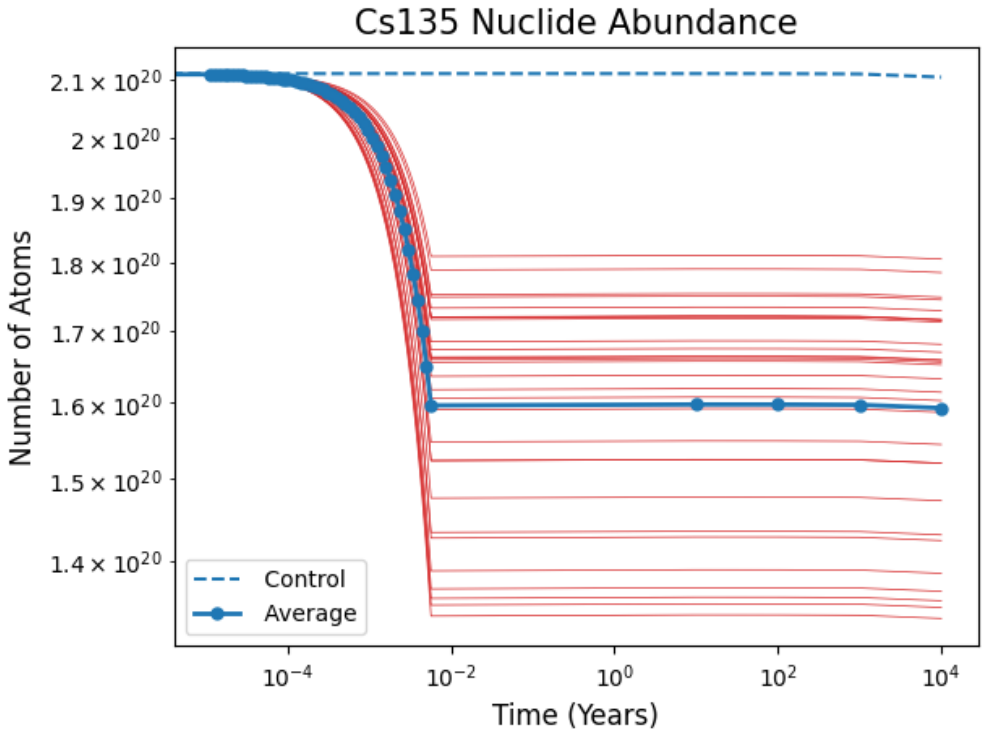

Perturbations in the LLFP TALYS-generated cross section translate to variation in the amount of depletion for all LLFPs. Uncertainty in the amount of activity of the irradiated sample was also quantified, and values are shown in Tables 4.10-4.14.

Table 4.10: Selenium-79 activity post-irradiation with a 50 MeV proton beam

Time (Years)	**Average (Bq)**	**SD (Bq)**	**Control (Bq)**
0	1.06E+15	1.31E+13	7.05E+06
10	1.64E+09	4.96E+07	7.05E+06
100	1.61E+07	5.04E+05	7.05E+06
1000	5.63E+06	3.06E+05	7.04E+06
10000	5.53E+06	3.00E+05	6.29E+06

Table 4.11: Zirconium-93 activity post-irradiation with a 70 MeV proton beam

Time (Years)	**Average (Bq)**	**SD (Bq)**	**Control (Bq)**
0	8.76E+14	6.61E+12	4.14E+06
10	7.76E+09	1.30E+08	5.54E+06
100	1.06E+09	4.77E+07	8.09E+06
1000	4.02E+08	1.92E+07	8.14E+06
10000	1.71E+07	3.20E+05	8.11E+06

Table 4.12: Technetium-99 activity post-irradiation with a 70 MeV proton beam

Time (Years)	**Average (Bq)**	**SD (Bq)**	**Control (Bq)**
0	2.27E+14	2.30E+13	1.40E+08
10	1.19E+09	4.62E+08	1.40E+08
100	1.52E+08	3.34E+06	1.40E+08
1000	1.34E+08	2.28E+06	1.40E+08
10000	1.12E+08	3.89E+06	1.36E+08

Table 4.13: Tin-126 activity post-irradiation with a 70 MeV proton beam

Time (Years)	**Average (Bq)**	**SD (Bq)**	**Control (Bq)**
0	7.96E+14	8.43E+12	2.97E+07
10	1.06E+10	1.34E+09	3.11E+07
100	8.00E+08	8.69E+05	3.11E+07
1000	2.05E+07	2.09E+06	3.10E+07
10000	1.98E+07	2.04E+06	3.02E+07

Table 4.14: Cesium-135 and Iodine-129 activity post irradiation

Time (Years)	Average (Bq)	SD (Bq)	Control (Bq)
0	7.25E+14	1.21E+13	2.47E+11
10	1.16E+11	1.40E+09	1.81E+11
100	1.21E+10	3.13E+06	2.34E+10
1000	1.69E+06	1.38E+05	2.23E+06
10000	1.69E+06	1.37E+05	2.22E+06

All isotopes except for Zirconium-93 show lower activity 10,000 years post-irradiation than an unirradiated sample after the same amount of time. The increase in the activity for the Zirconium-93 case is most likely due to the production of Niobium-92, which has a half-life longer than the initial Zirconium-93 LLFP.

Table 4.15: Amount of LLFPs transmuted per year

Isotope	Average (#)	SD (#)	Average (g)	SD (g)
Se79	2.55E+19	5.25E+18	0.59	0.12
Zr93	4.85E+19	1.17E+19	1.31	0.32
Tc99	2.61E+20	4.13E+19	7.51	1.19
Sn126	3.97E+19	7.83E+18	1.46	0.29
I129	4.15E+19	8.50E+18	1.56	0.31
Cs135	5.13E+19	1.44E+19	2.02	0.53

Technetium-99 is depleted in the largest quantity of 7.51±1.19g/year while Selenium-79 is depleted in the smallest quantity of 0.59±0.12g/year. Technetium-99 had the largest number of nuclides exposed to the proton beam and Selenium-79 had the smallest. This suggests that the main limiting factor for transmutation is the number of atoms exposed to the proton beam.

4.2 Mutli-Particle Comparison

Other options for non-neutron transmutation of LLFPs include deuteron and alpha particles. Transmutation analysis for protons, alpha particles, and deuterons was performed using the TENDL2021 cross section library, SRIM, to calculate the penetration depth for each particle, and FISPACT to perform the depletion calculation. For this analysis, the flux-energy spectrum of the beam is not taken into account, so the absolute number of nuclides will be overestimated. Therefore, direct comparisons to the results of the previous section will not be included. However, if alpha particles or deuterons transmute LLFPs better than protons, a more in-depth analysis will be justified.

4.2.1 TENDL Cross Sections

The TENDL 2021 data library has TALYS-generated proton, alpha, and deuteron cross sections from 0-200 MeV. The cross sections are plotted for the energy range where the cross section values are greater than 10^{-13} b. For alpha particles (Figures 4.39-4.44), this occurs from 2-70MeV. For deuterons (Figures 4.45-4.50), cross section values become significant above 0.1 MeV. TENDL2021 proton cross sections are previously plotted in Figures 4.7-4.12

Figure 4.39: TENDL2021 Selenium-79 alpha cross sections from 2-70 MeV

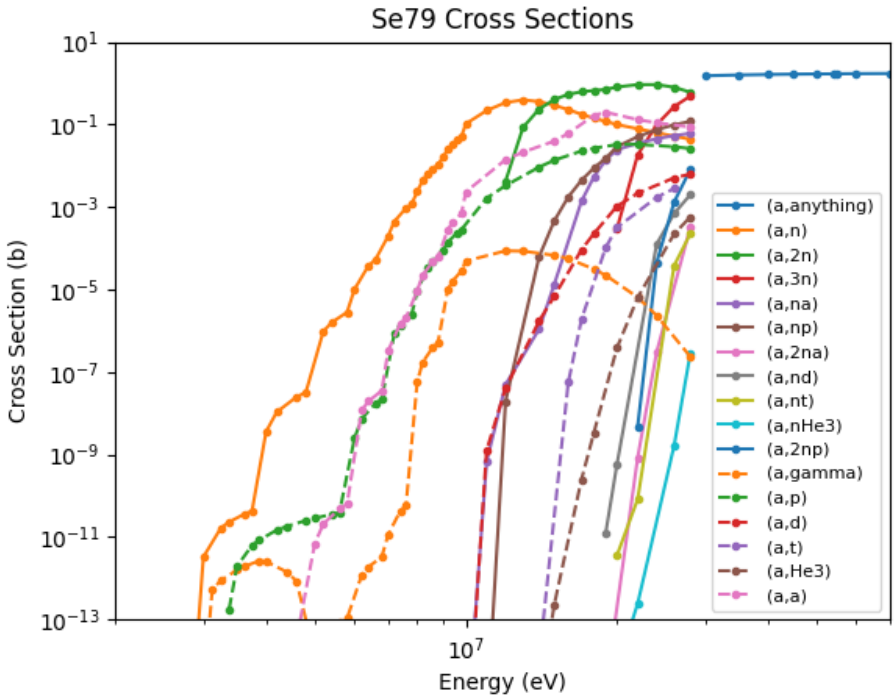

Figure 4.40: TENDL2021 Zirconium-93 alpha cross sections from 2-70 MeV

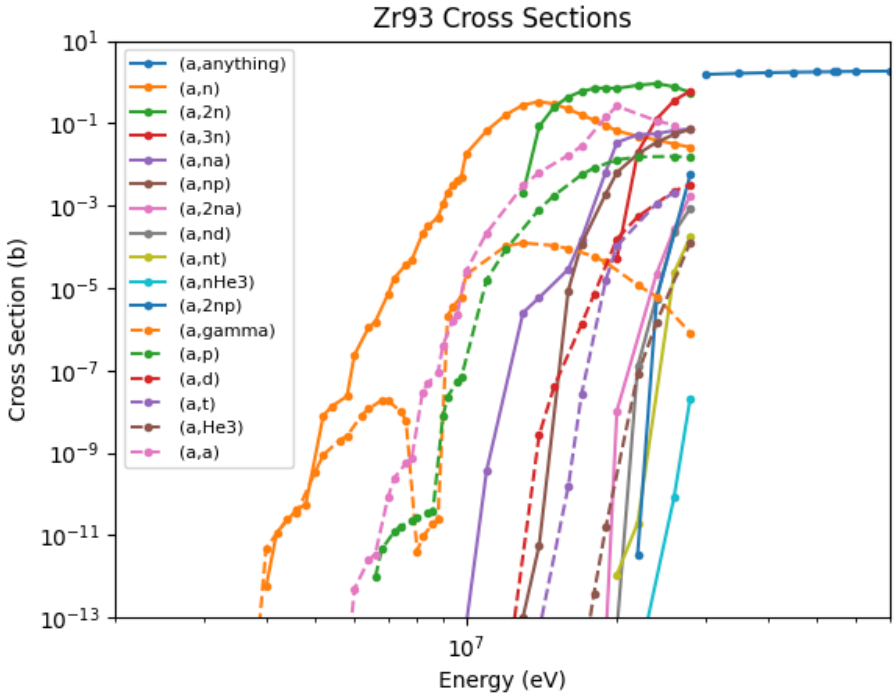

Figure 4.41: TENDL2021 Technetium-99 alpha cross sections from 2-70 MeV

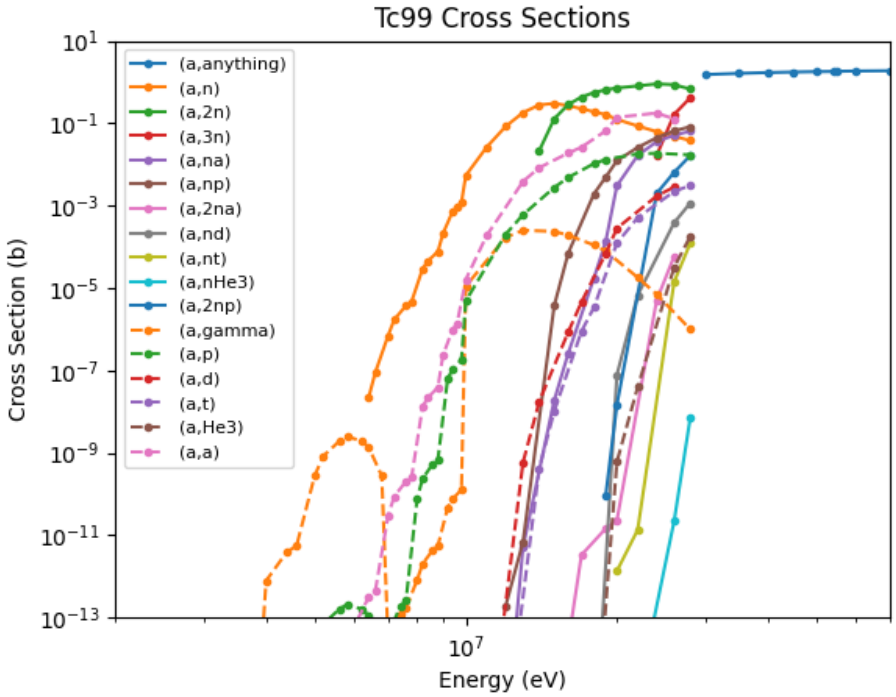

Figure 4.42: TENDL2021 Tin-126 alpha cross sections from 2-70 MeV

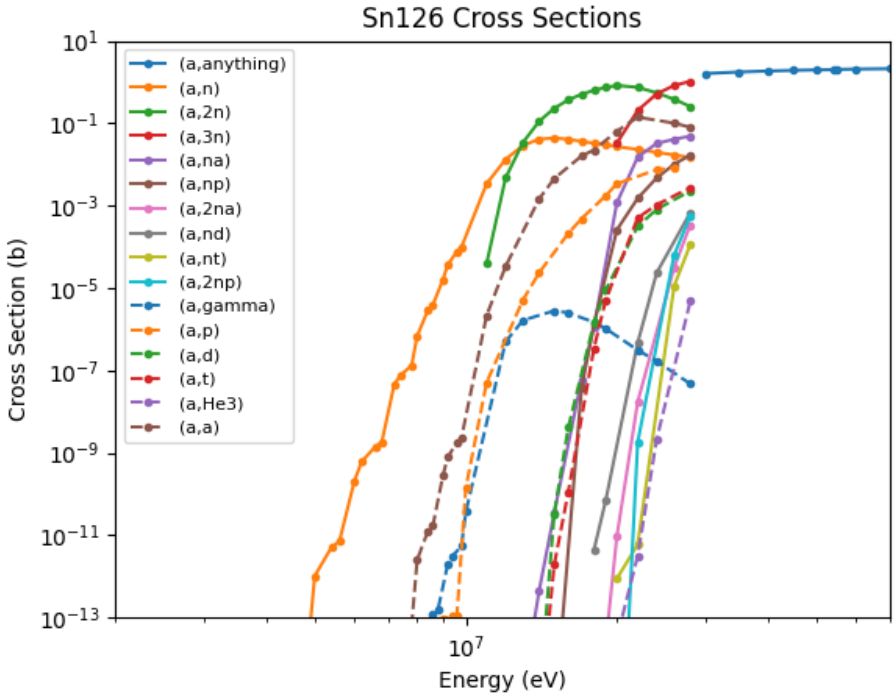

Figure 4.43: TENDL2021 Iodine-129 alpha cross sections from 2-70 MeV

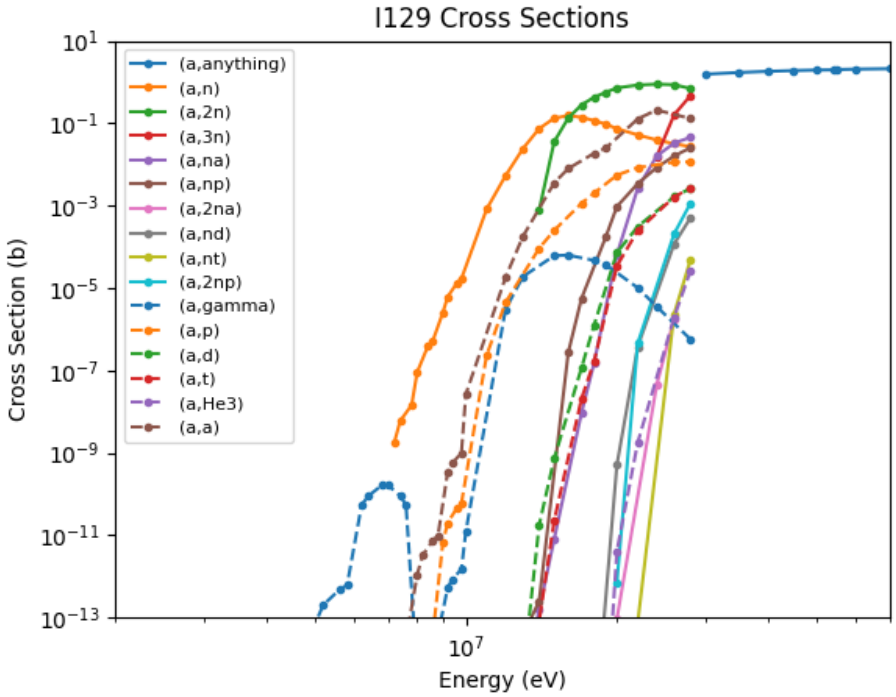

Figure 4.44: TENDL2021 Cesium-135 alpha cross sections from 2-70 MeV

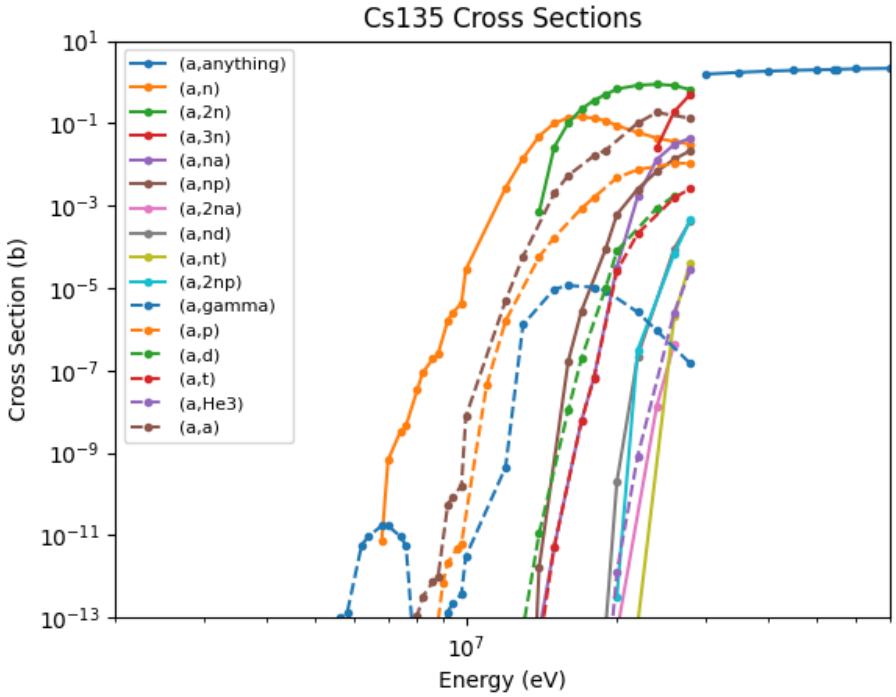

Figure 4.45: TENDL2021 Selenium-79 deuteron cross sections from 0.1-70 MeV

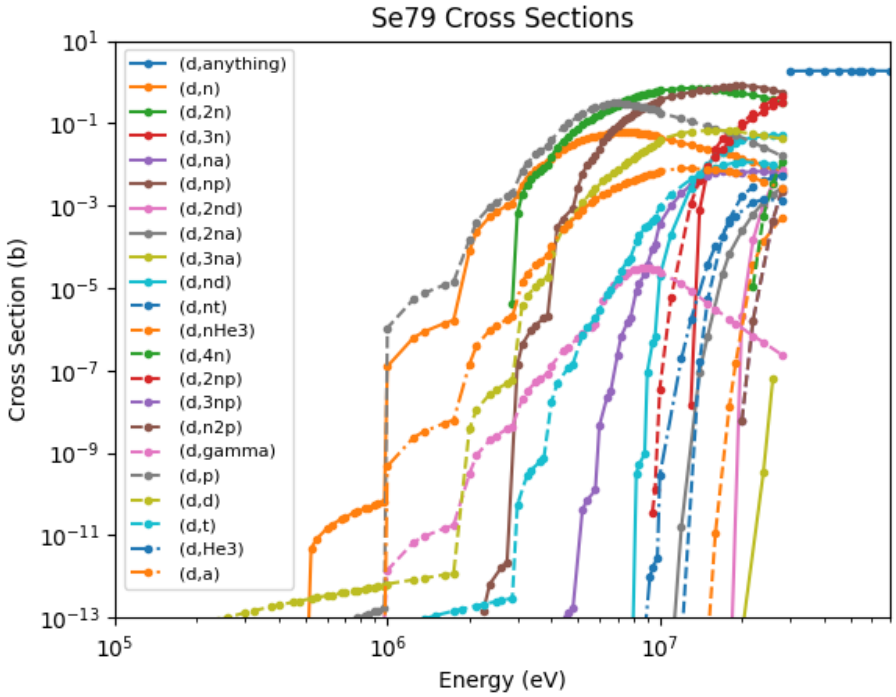

Figure 4.46: TENDL2021 Zirconium-93 deuteron cross sections from 0.1-70 MeV

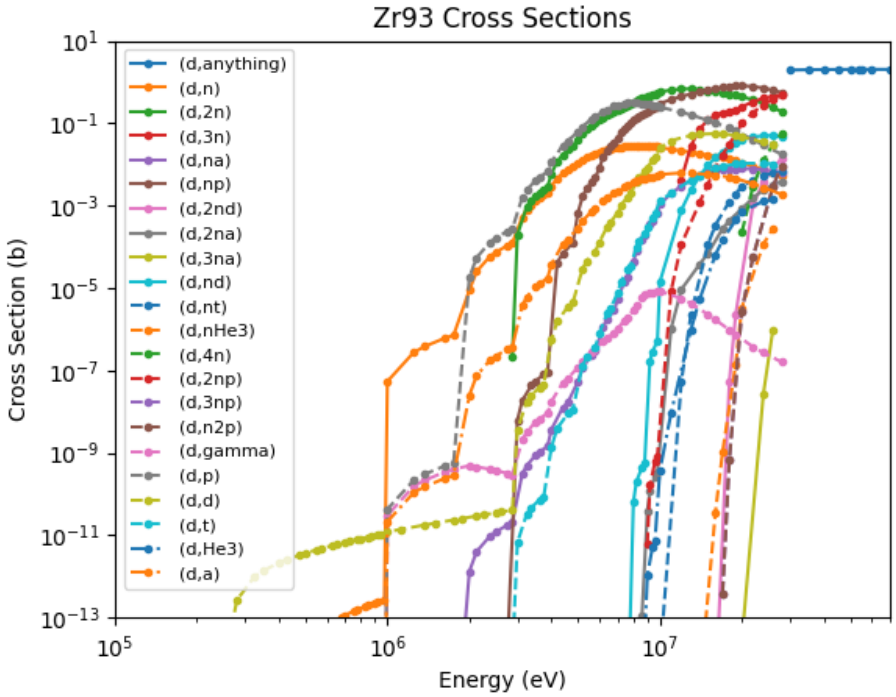

Figure 4.47: TENDL2021 Technetium-99 deuteron cross sections from 0.1-70 MeV

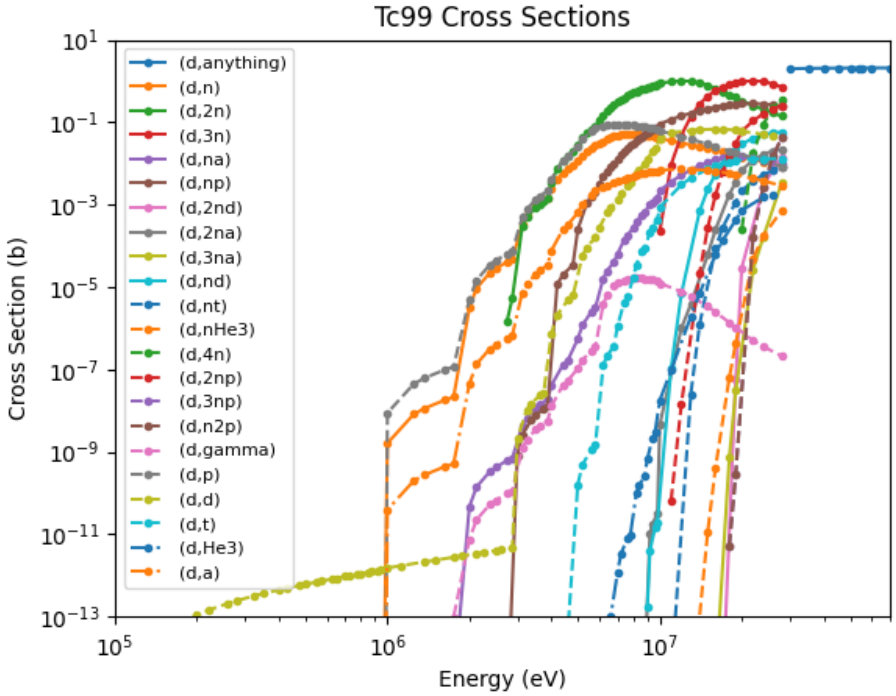

Figure 4.48: TENDL2021 Tin-126 deuteron cross sections from 0.1-70 MeV

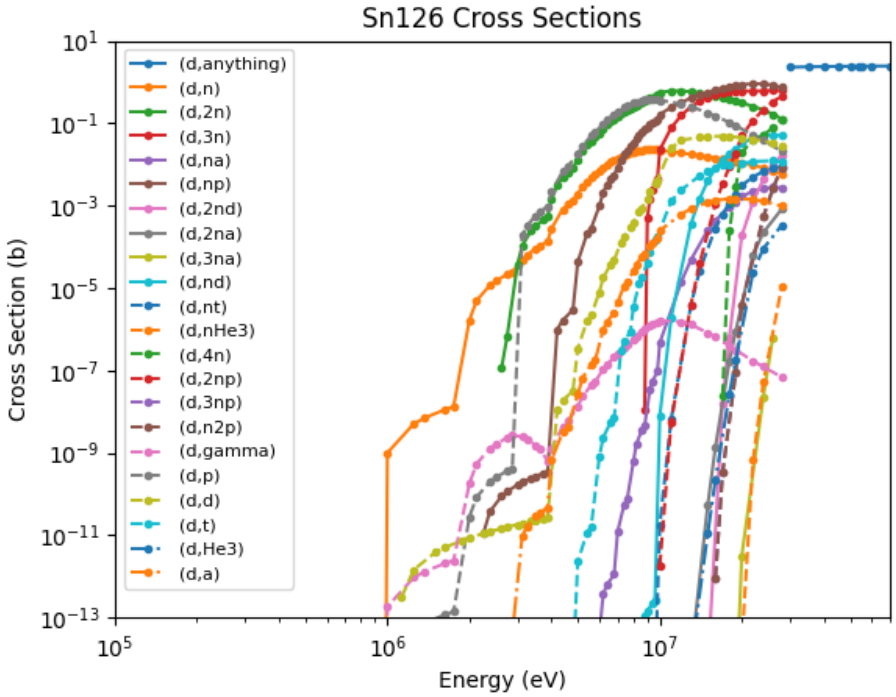

Figure 4.49: TENDL2021 Iodine-129 deuteron cross sections from 0.1-70 MeV

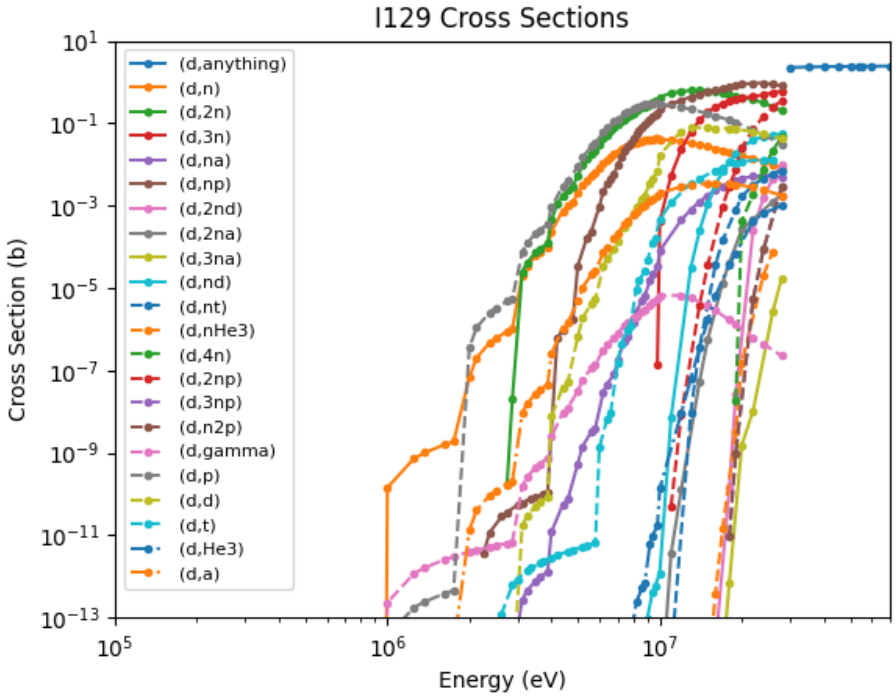

Figure 4.50: TENDL2021 Cesium-135 deuteron cross sections from 0.1-70 MeV

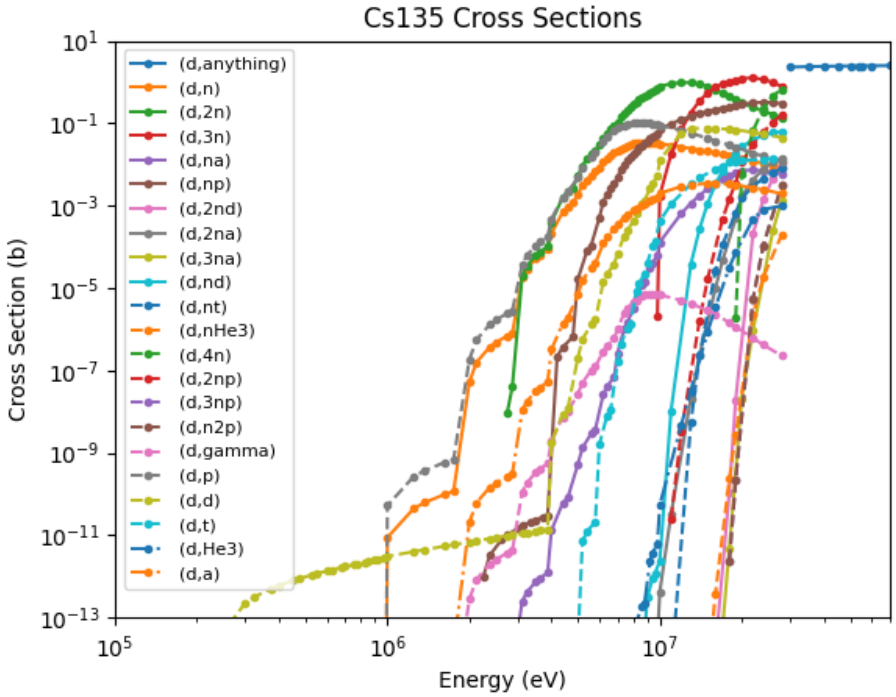

4.2.2 Penetration Depth Calculation

Deuteron reaction cross sections are higher than proton and alpha cross sections for a given energy. Proton and alpha interactions require a specific activation energy to be reached for the reaction to occur. However, the addition of a neutron in the deuteron nucleus, when compared to the lone proton, leads to nuclear reactions with positive Q-values due to the additional mass provided. This means that deuterons result in higher amounts of transmutation than protons and alphas for simulations with the same initial parameters (mass, energy, flux, and irradiation time) not considering penetration depth, as shown in Figures 4.51-4.56.

Figure 4.51: Selenium-79 Proton, Alpha, and Deuteron depletion not considering penetration depth

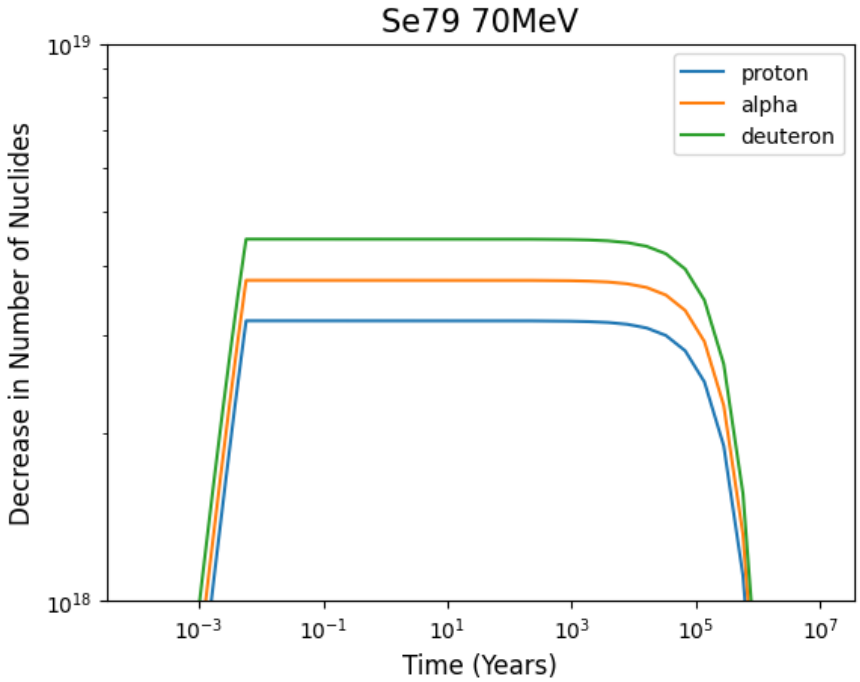

Figure 4.52: Zirconium-93 Proton, Alpha, and Deuteron depletion not considering penetration depth

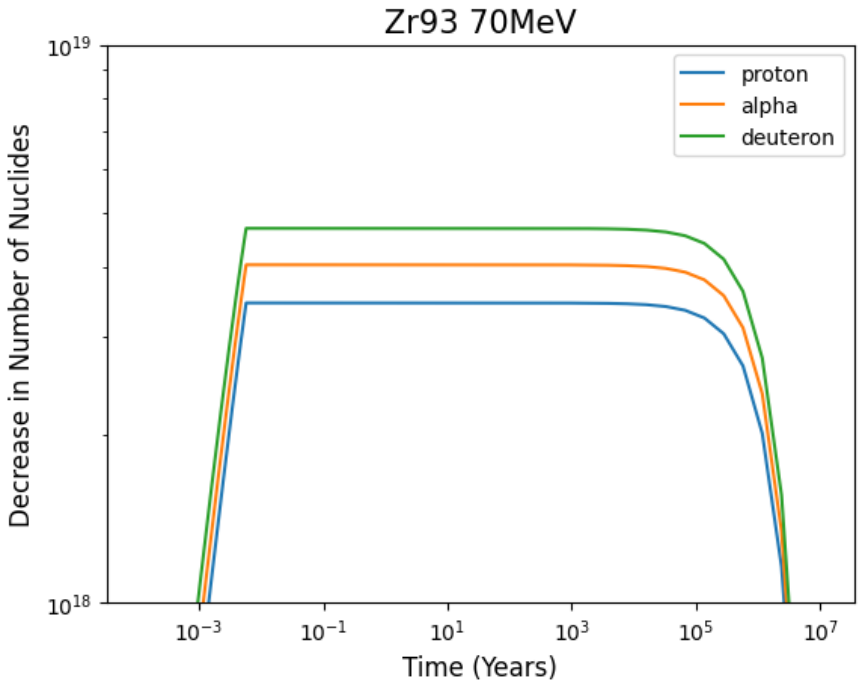

Figure 4.53: Technetium-99 Proton, Alpha, and Deuteron depletion not considering penetration depth

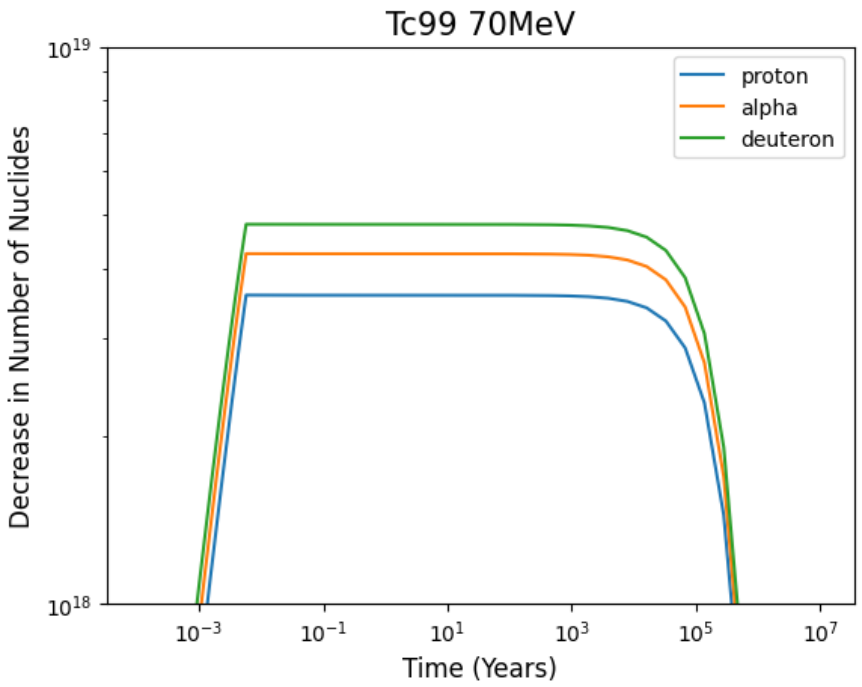

Figure 4.54: Tin-126 Proton, Alpha, and Deuteron depletion not considering penetration depth

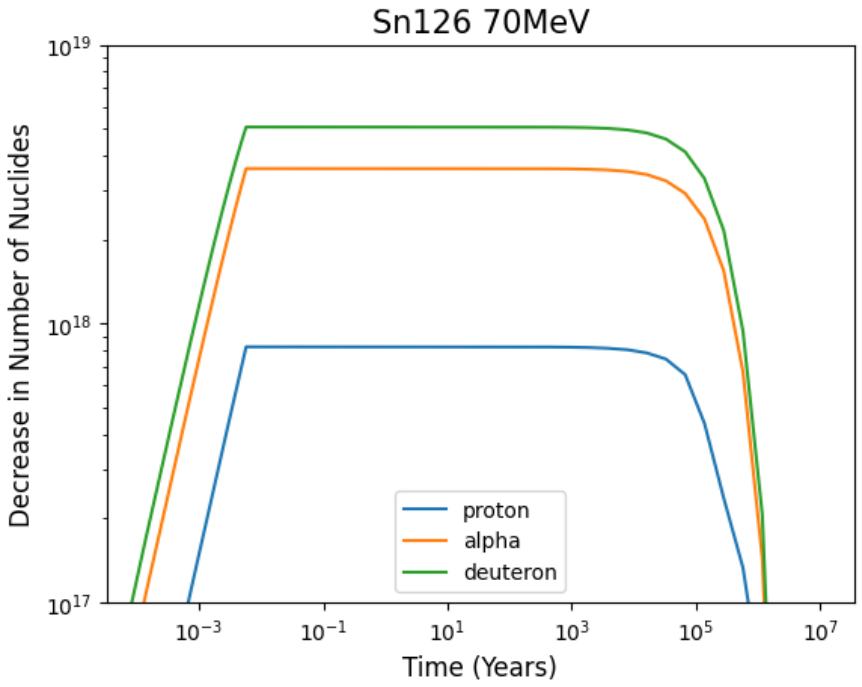

Figure 4.55: Iodine-129 Proton, Alpha, and Deuteron depletion not considering penetration depth

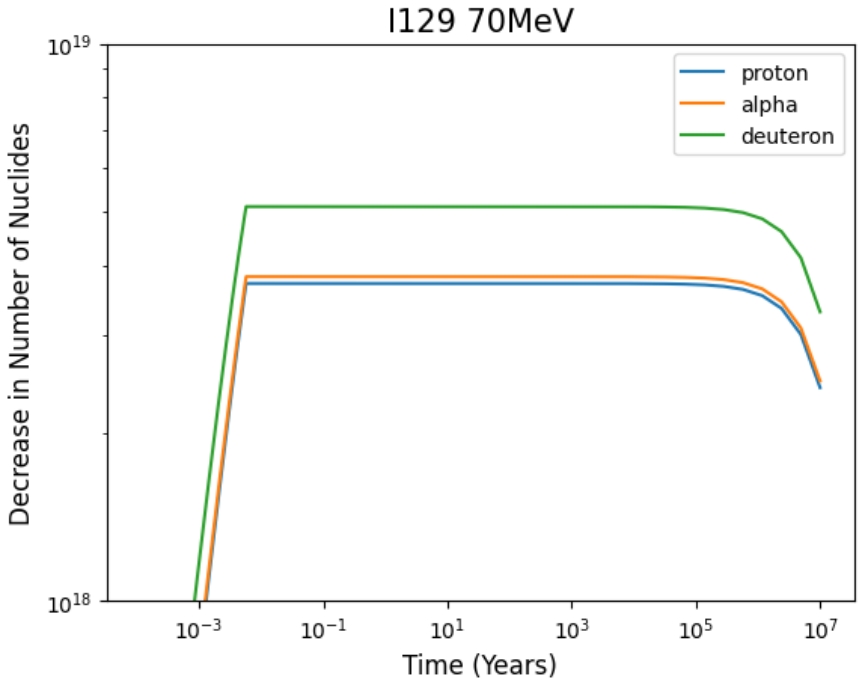

Figure 4.56: Cesium-135 Proton, Alpha, and Deuteron depletion not considering penetration depth

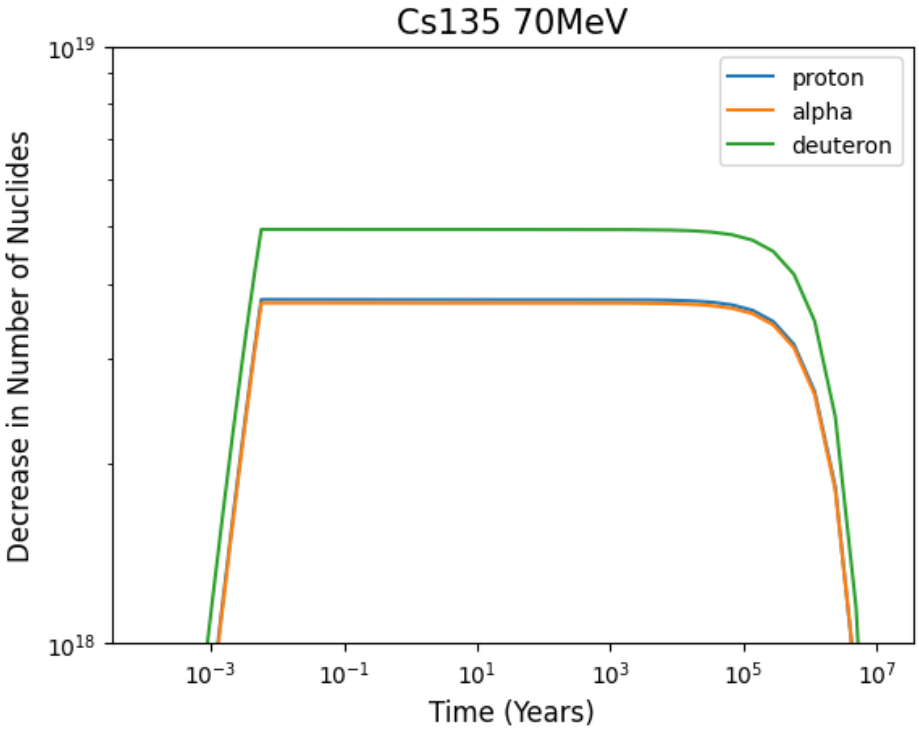

However, the larger deuteron mass will also result in a smaller penetration depth. This lower penetration depth means that deuterons will interact with fewer nuclides than protons. The penetration depth and number of irradiated nuclides for each LLFP were calculated for protons, deuterons, and alphas, and the transmutation results were compared. The penetration depth and number of nuclides are shown in Tables 4.16, 4.17, and 4.18. For the proton irradiation case, the penetration depth determined by PHITS is included for validation. Data for the PHITS analysis was not included for I129 or Cs135 because, in the PHITS analysis, the two isotopes were run as a compound, unlike the SRIM case where individual nuclides were analyzed separately. Comparisons for protons between the results obtained with PHITS and SRIM were in close agreement. The number of nuclides was calculated from the penetration depth in the same way as discussed in the previous section using Equation 4.1.

Figure 4.57: Selenium-79 Proton, Alpha, and Deuteron penetration depth calculated by SRIM

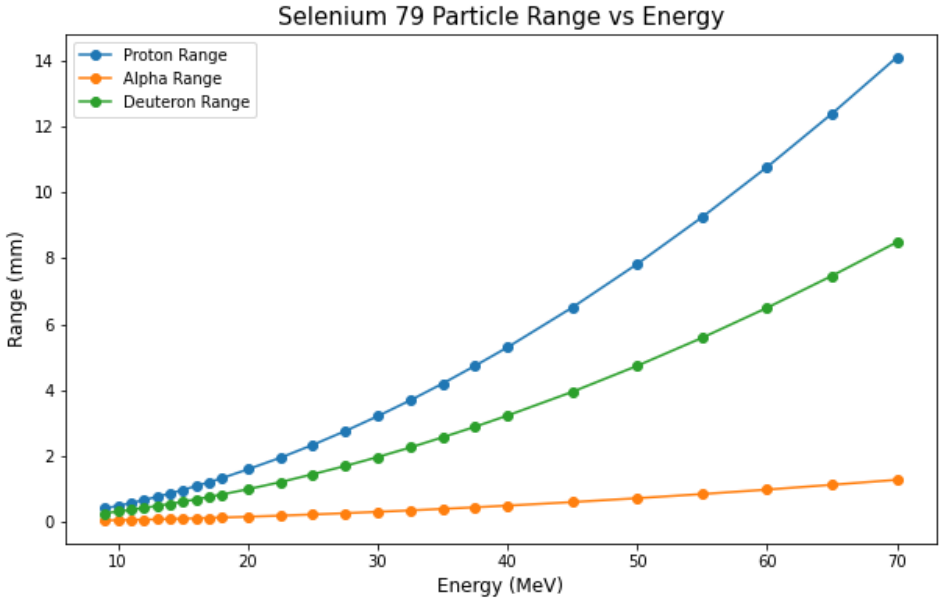

Figure 4.58: Zirconium-93 Proton, Alpha, and Deuteron penetration depth calculated by SRIM

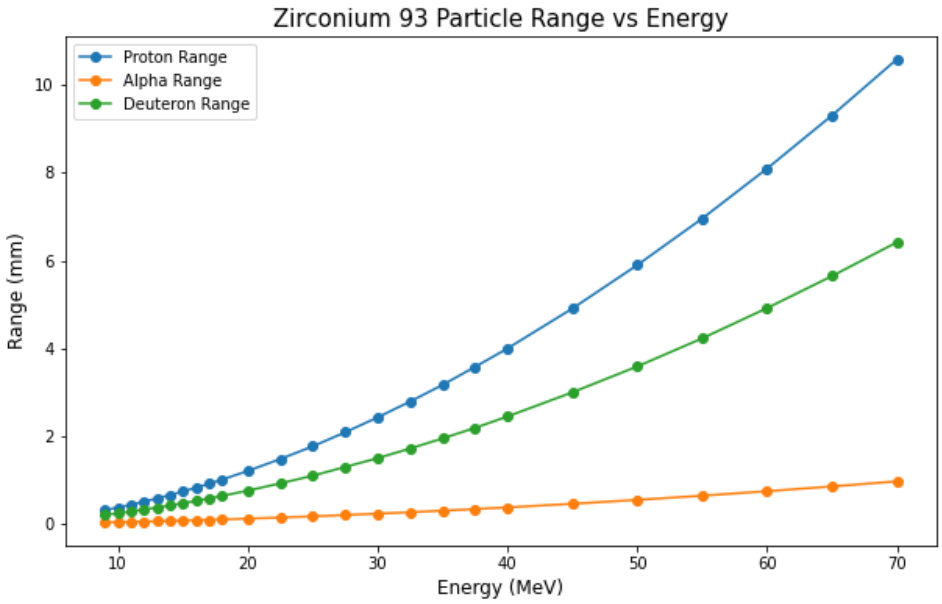

Figure 4.59: Technetium-99 Proton, Alpha, and Deuteron penetration depth calculated by SRIM

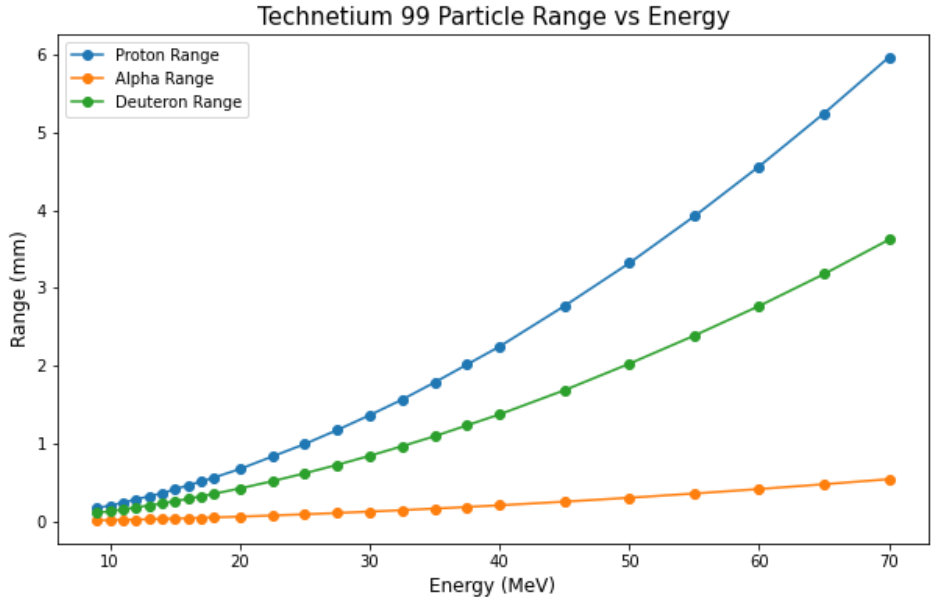

Figure 4.60: Tin-126 Proton, Alpha, and Deuteron penetration depth calculated by SRIM

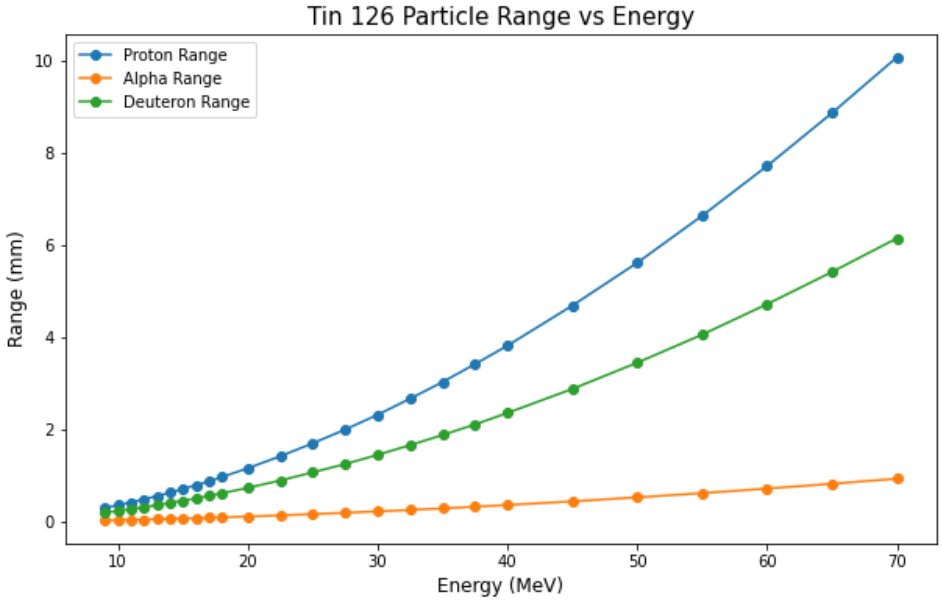

Figure 4.61: Iodine-129 Proton, Alpha, and Deuteron penetration depth calculated by SRIM

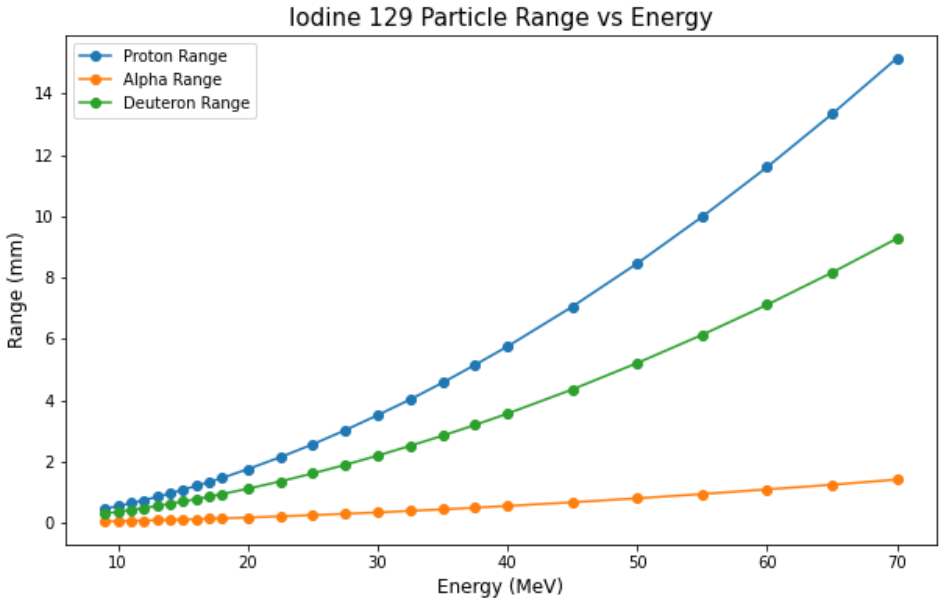

Figure 4.62: Cesium-135 Proton, Alpha, and Deuteron penetration depth calculated by SRIM

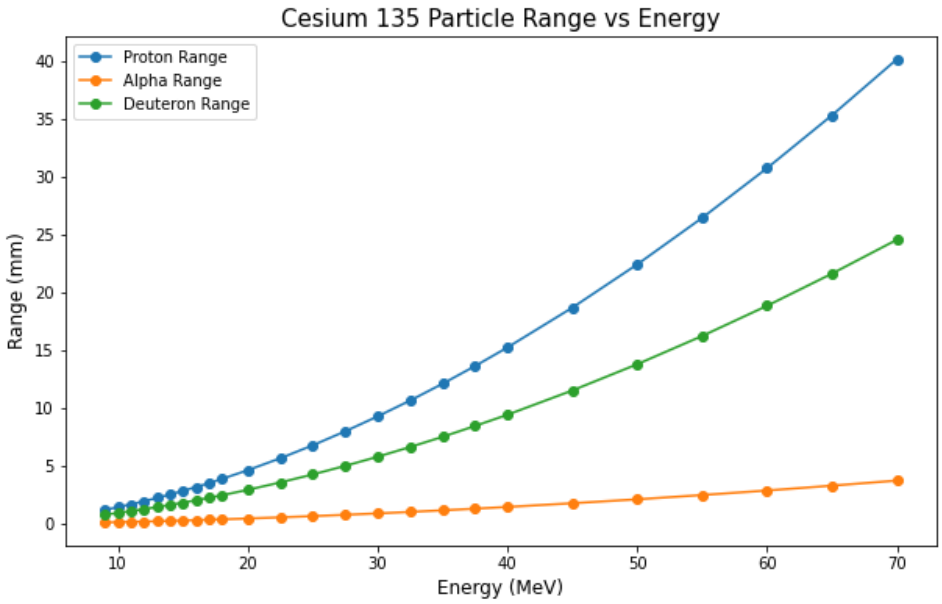

Table 4.16: Penetration Depth of 70 MeV Protons

Isotope	**SRIM Range (mm)**	**PHITS Range (mm)**	**Number of Nuclides**
Se79	14.1	16.17	1.62416×10^{21}
Zr93	10.59	10.79	1.39813×10^{21}
Tc99	5.96	6.130	1.2072×10^{20}
Sn126	10.09	11.12	1.4039×10^{21}
I129	15.16	N/A	1.09772×10^{21}
Cs135	40.18	N/A	1.10693×10^{21}

Table 4.17: Penetration Depth of 70 MeV Alpha Particles

Isotope	SRIM Range (mm)	Number of Nuclides
Se79	1.28	1.47441×10^{20}
Zr93	0.97089	1.28181×10^{20}
Tc99	0.54932	1.2072×10^{20}
Sn126	0.94217	1.31092×10^{20}
I129	1.42	1.0282×10^{20}
Cs135	3.76	1.03586×10^{20}

Table 4.18: Penetration Depth of 70 MeV Deuterons

Isotope	SRIM Range (mm)	Number of Nuclides
Se79	8.49	9.77949×10^{20}
Zr93	6.42	8.47593×10^{20}
Tc99	3.62	7.9554×10^{20}
Sn126	6.16	8.57091×10^{20}
I129	9.28	6.71952×10^{20}
Cs135	24.58	6.77164×10^{20}

4.2.3 Depletion Calculation

For all LLFPs, the greater penetration depth for protons results in a larger overall transmutation rate. The penalty of smaller penetration depth outweighs the benefit gained by the higher deuteron cross section at high energies, as shown in Figures 4.63-4.68. In the case of a very thin target with recirculation and reenergization, deuterons and alphas could outperform protons, but the target might be unfeasibly thin.

Figure 4.63: Selenium-79 Proton, Alpha, and Deuteron depletion considering penetration depth

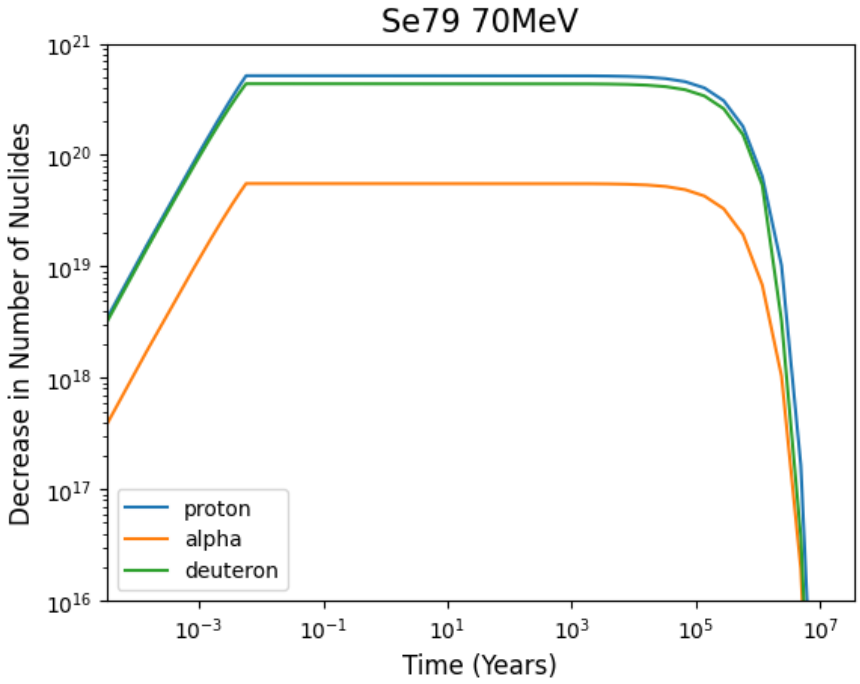

Figure 4.64: Zirconium-93 Proton, Alpha, and Deuteron depletion considering penetration depth

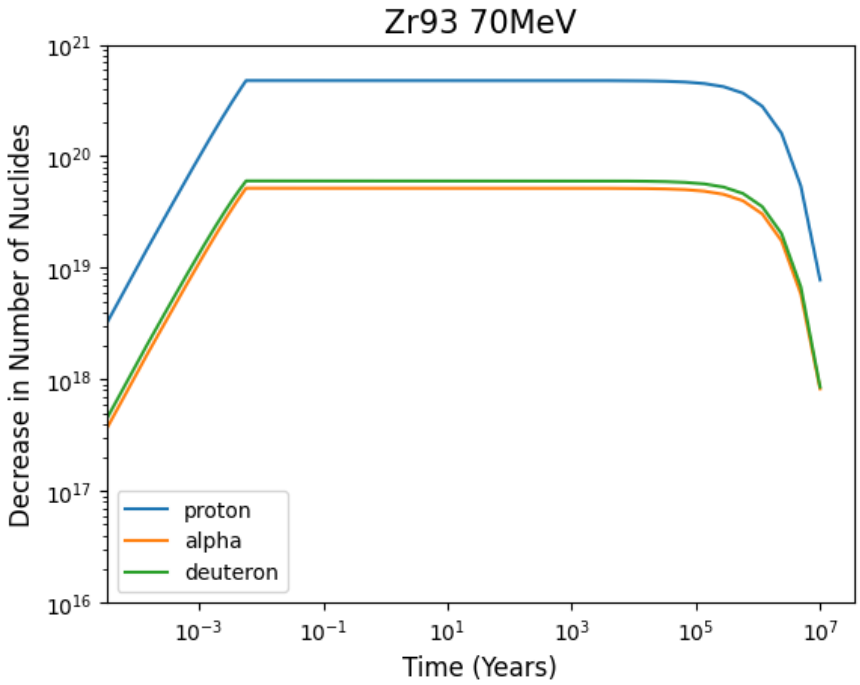

Figure 4.65: Technetium-99 Proton, Alpha, and Deuteron depletion considering penetration depth

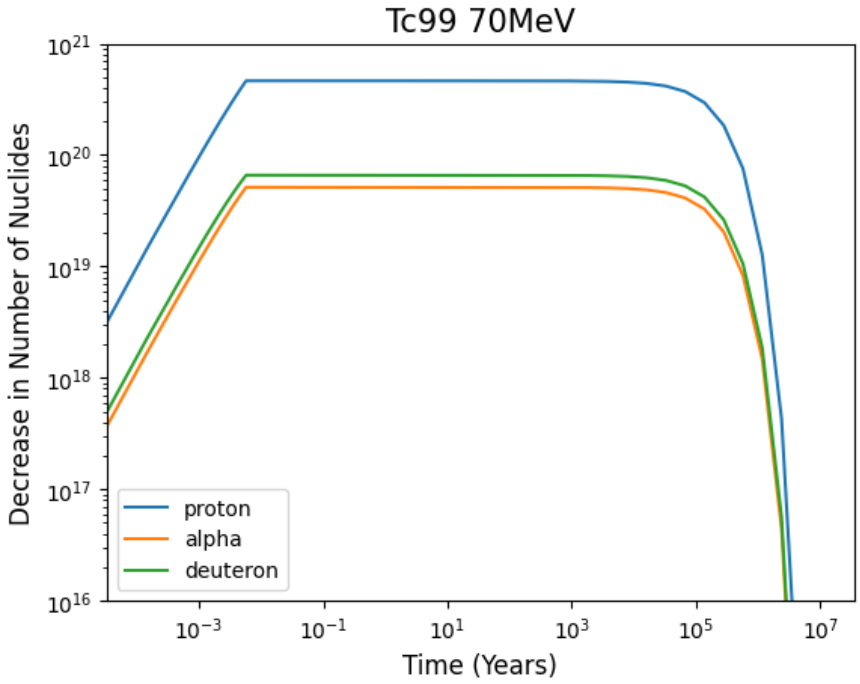

Figure 4.66: Tin-126 Proton, Alpha, and Deuteron depletion considering penetration depth

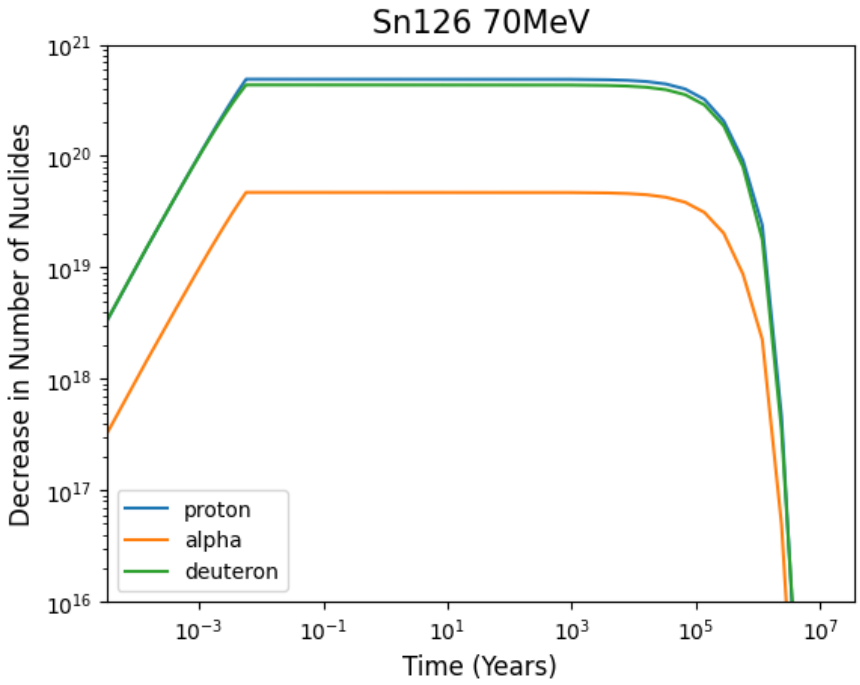

Figure 4.67: Iodine-129 Proton, Alpha, and Deuteron depletion considering penetration depth

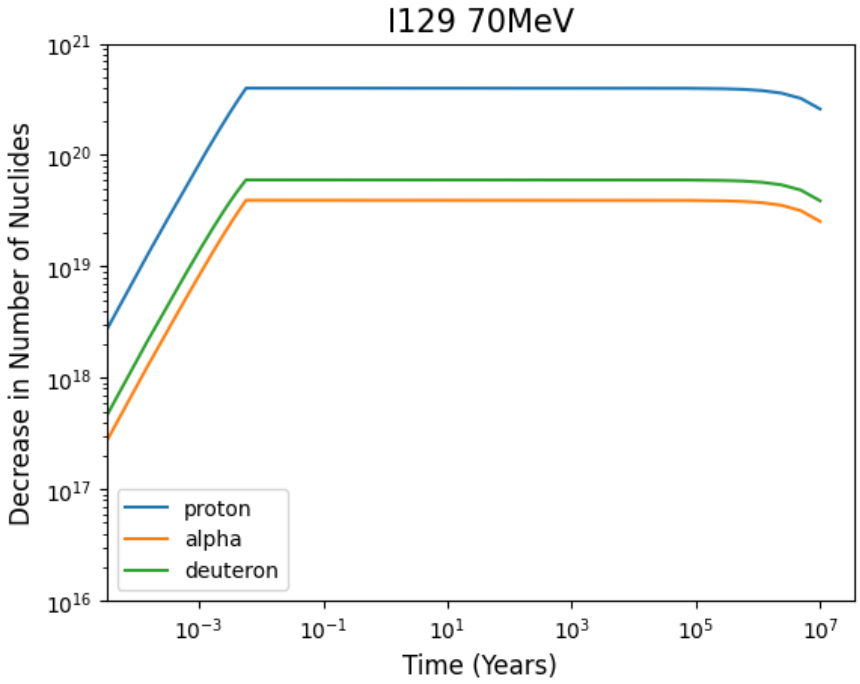

Figure 4.68: Cesium-135 Proton, Alpha, and Deuteron depletion considering penetration depth

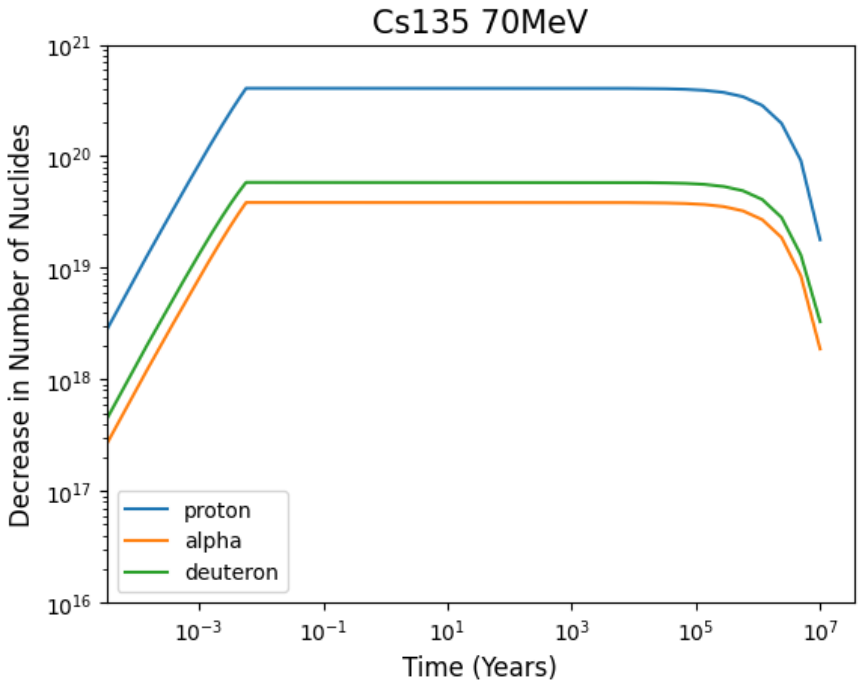

Chapter 5

Conclusions and Future Work

5.1 Conclusions

Table 5.1: Amount of LLFPs transmuted per year compared to production levels

Isotope	**Production (g/GW·yr)**	**Average Transmutation (g)**	**SD (g)**
Se79	66	0.59	0.12
Zr93	8040	1.31	0.32
Tc99	8540	7.51	1.19
Sn126	300	1.46	0.29
I129	1960	1.56	0.31
Cs135	2760	2.02	0.53

The transmutation rates and radioactivity results obtained from transmutation calculations represent an improvement over the natural decay case. However, the magnitude of improvement is lower than desired. The maximum amount of LLFP depletion is only on the order of 1g per year with continuous operation of a proton beam with a 10mA current. Most LLFPs are produced in quantities on the order of 100g - 1 kg per year for a 1 GW (thermal) nuclear reactor. Selenium-79 is the one exception, only 66g are generated per year for 1 GW (thermal) nuclear reactor. Assuming the 0.59 g/year Selenium-79 transmutation rate previously calculated, it would take approximately 100 commercial cyclotrons to transmute a year's worth of Selenium-79. If cyclotron technology or subsequent target design could be improved, then this could be achievable with a smaller number of beams.

Possible ways to increase the transmutation rate are to increase the proton beam flux and/or increase the penetration depth of the proton beam in the material. The beam's current limits the proton beam flux so advances in proton cyclotron technology could significantly impact the transmutation rate. Increasing irradiation time is also dependent on the performance of the proton cyclotrons.

Future work will seek to increase the number of atoms exposed to protons through target design and utilization of higher beam energies. Future experimental validation of the computationally generated cross sections for the materials of interest will be crucial to assess the

validity of the transmutation results for the nuclear reaction models considered in this work and the spallation reactions that will be used in later work.

5.2 Future Work

5.2.1 Neutron and Proton Iteration

The work in this thesis estimated the transmutation rate achievable with current commercial proton cyclotron technology from nuclear reactions alone. Preliminary work has begun to evaluate the impact of spallation reactions on transmutation rates of LLFP irradiation as higher proton beam energies are considered. The inclusion of spallation reactions should increase the transmutation rate through the addition of more reaction channels increasing the total cross section and the production of more secondary neutrons. Initial work has been conducted to facilitate the simultaneous irradiation of protons and neutrons in a FISPACT depletion calculation, and preliminary estimates of spallation transmutation rates have been calculated.

Proton irradiation produces secondary neutrons through (p,n) reactions and spallation reactions at higher energies. As LLFPs have higher neutron cross sections than proton cross sections, the secondary neutrons can be used to transmute additional nuclides even if the flux is lower.

FISPACT can only perform a depletion calculation with a single incident particle at a time. Therefore, an iteration scheme was designed to calculate depletion for simultaneous irradiation of a proton beam and the secondary neutrons produced from proton interactions.

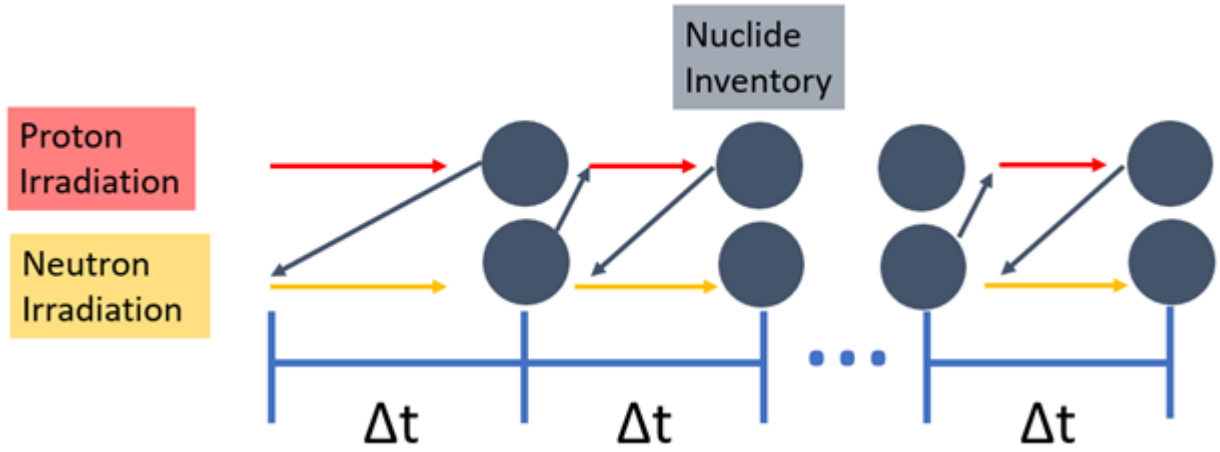

Figure 5.1: A schematic showing the iteration scheme designed to facilitate the simultaneous depletion of an inventory of nuclides with protons and neutrons in FISPACT

The bash script used to run the iteration scheme is included in Listing A.2. For a given time step, a proton and neutron depletion calculation is performed. The initial nuclide inventory in the neutron calculation is the output inventory from the previous proton calculation. The initial proton irradiation step is performed with the user input nuclide information.

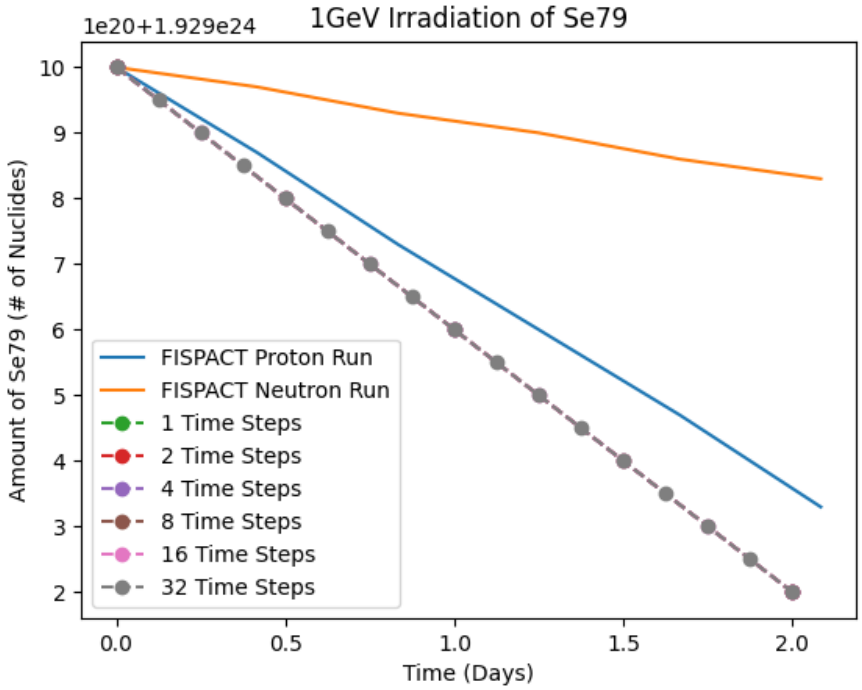

Figure 5.2: Number of Selenium-79 nuclides in a blanket surrounding a Technetium-99 target

Each subsequent proton irradiation uses the neutron output nuclide inventory from the end of the previous time step. The final neutron output inventory is used as the final output inventory for the total irradiation time.

5.2.2 Spallation

Preliminary results using a Technetium-99 spallation target and Selenium-79 blanket show improved transmutation results. The neutron and proton iteration scheme mentioned in the previous section was applied to a 1 GeV incident proton beam. The TENDL2017 library extends the cross section data at 200 MeV to 1 GeV to estimate higher-energy reaction rates and is the library used in this analysis. Additional future work will examine the impact of using the High-Energy Intra-Nuclear Cascade Liège-based Residual (HEIR-0.1) library[20].

The proton and neutron flux spectra and magnitude were calculated using PHITS, and the depletion calculation was performed using FISPACT. After two days of irradiation, 3.65×10^{22} nuclides of Technetium-99 and 8×10^{20} nuclides of Selenium-79 are transmuted. For continuous operation of the proton beam for a year, this corresponds to 1.094 kg of Technetium-99, and 24.02 g of Selenium-79 transmuted. Spallation presents a significant improvement over the commercial accelerator case and will be the focus of future research.

Appendix A

FISPACT

A.1 Inventory Calculation

Listing A.1: FISPACT inventory input file for elemental Selenium irradiation

```
<< -----set initial switches and get nuclear data----- >>
CLOBBER
GETXS 0
GETDECAY 0
FISPACT
* Se 70 MeV
DENSITY 4.3
FUEL 5
Se77 5.61E+19
Se78 1.06E+20
Se79 2.26E+20
Se80 3.48E+20
Se82 8.93E+20
MIND 1E3
UNCERTAINTY 0
HALF
HAZARDS
<< -----irradiation phase----- >>
FLUX 1.6941e+18
ATOMS
TIME 0.1 HOURS
ATOMS
TIME 0.01323467 HOURS
ATOMS
TIME 0.01498623 HOURS
ATOMS
TIME 0.01696961 HOURS
ATOMS
TIME 0.01921548 HOURS
```

```
ATOMS
TIME 0.02175858 HOURS
ATOMS
TIME 0.02463826 HOURS
ATOMS
TIME 0.02789905 HOURS
ATOMS
TIME 0.03159139 HOURS
ATOMS
TIME 0.03577241 HOURS
ATOMS
TIME 0.04050676 HOURS
ATOMS
TIME 0.0458677 HOURS
ATOMS
TIME 0.05193814 HOURS
ATOMS
TIME 0.05881197 HOURS
ATOMS
TIME 0.06659554 HOURS
ATOMS
TIME 0.07540924 HOURS
ATOMS
TIME 0.0853894 HOURS
ATOMS
TIME 0.0966904 HOURS
ATOMS
TIME 0.10948705 HOURS
ATOMS
TIME 0.1239773 HOURS
ATOMS
TIME 0.14038528 HOURS
ATOMS
TIME 0.1589648 HOURS
ATOMS
TIME 0.18000326 HOURS
ATOMS
TIME 0.20382608 HOURS
ATOMS
TIME 0.23080178 HOURS
ATOMS
TIME 0.26134763 HOURS
ATOMS
TIME 0.29593611 HOURS
ATOMS
TIME 0.33510226 HOURS
ATOMS
```

```
TIME 0.37945192 HOURS
ATOMS
TIME 0.42967112 HOURS
ATOMS
TIME 0.48653665 HOURS
ATOMS
TIME 0.55092815 HOURS
ATOMS
TIME 0.62384164 HOURS
ATOMS
TIME 0.70640499 HOURS
ATOMS
TIME 0.79989533 HOURS
ATOMS
TIME 0.9057588 HOURS
ATOMS
TIME 1.02563294 HOURS
ATOMS
TIME 1.16137202 HOURS
ATOMS
TIME 1.31507572 HOURS
ATOMS
TIME 1.48912159 HOURS
ATOMS
TIME 1.68620185 HOURS
ATOMS
TIME 1.90936501 HOURS
ATOMS
TIME 2.16206308 HOURS
ATOMS
TIME 2.44820489 HOURS
ATOMS
TIME 2.77221661 HOURS
ATOMS
TIME 3.13911019 HOURS
ATOMS
TIME 3.55456091 HOURS
ATOMS
TIME 4.02499515 HOURS
ATOMS
TIME 4.55768978 HOURS
ATOMS
TIME 5.16088476 HOURS
ATOMS
TIME 5.84391057 HOURS
ATOMS
<< -----cooling phase----- >>
```

```
FLUX 0.
ZERO
TIME 0 YEARS
ATOMS
TIME 10.0 YEARS
ATOMS
TIME 90.0 YEARS
ATOMS
TIME 900.0 YEARS
ATOMS
TIME 9000.0 YEARS
ATOMS
END
* END
/*
```

A.2 Iteration

Listing A.2: FISPACT proton-neutron iteration scheme

```
#!/bin/bash

# Set initial values for proton and neutron fluxes.
ProtonFluxes=1E18
NeutronFluxes=1E16

# Array of nuclear products and their corresponding densities.
Products=('Tc99' 'I129' 'Cs135' 'Zr93' 'Sn126' 'Se79')
Densities=(11.5 4.93 1.873 6.51 7.31 4.79)

# Array of values for the number of stepsizes taken during the
   irradiation.
Ns=(2 4 8 16 32)

# Loop through each value of N.
for N in ${Ns[@]};
do
    # Loop through values from 1 to N.
    for c in $(seq 1 $N);
    do
        # Loop through each product.
        for p in 0 1 2 3 4 5;
        do
            # Check if c is even.
            if [ $(($c % 2)) -eq 0 ]
```

```
26              then
27                  # Copy files for proton calculation.
28
29          cp collapse.i_proton collapse.i
30                  cp files_proton files
31                  cp lowE_proton_fluxes fluxes
32                  cp COLLAPX_proton COLLAPX
33                  cp ARRAYX_proton ARRAYX
34                  f0=$ProtonFluxes
35                  f1=$NeutronFluxes
36              else
37                  # Copy files for neutron calculation.
38
39          cp collapse.i_neutron collapse.i
40                  cp files_neutron files
41                  cp lowE_neutron_fluxes fluxes
42                  cp COLLAPX_neutron COLLAPX
43                  cp ARRAYX_neutron ARRAYX
44                  f0=$NeutronFluxes
45                  f1=$ProtonFluxes
46              fi
47
48              # If this is the first run, write the first FISPACT
                    inventory script.
49              if [ $c -eq 1 ]; then python3 write_inventory.py ${f0}
                    ${Products[$p]} ${Densities[$p]} ${N}; fi
50
51              # Execute the FISPACT command to calculate the nuclide
                    inventory.
52              fispact inventory
53
54              # Copy the output inventory file to be saved for later
                    analysis.
55              cp inventory.out inventory.out_${N}_$c
56
57              # Take the output of the FISPACT simulation and use it
                    to write the next input file.
58              python3 redo.py inventory.out_${N}_$c ${f1} ${N}
59          done
60      done
61
62      # Copy the final inventory file for each value of N, this final
            value is the end of the irradiation.
63      cp inventory.out final_${N}
64  done
```

References

[1] R. Wigeland *et al.*, "Nuclear fuel cycle evaluation and screening – final report," Idaho National Laboratory, Tech. Rep. INL/EXT-14-31465, 2014.

[2] *Nuclear wallet cards*, Database, from the Brookhaven National Laboratory, 2019. URL: https://www.nndc.bnl.gov/wallet/wallet11.pdf.

[3] B. Savage, *AFCI/GNEP R&D Program*, Presentation for Nuclear Energy Research Advisory Committee (NRAC), Feb. 2007.

[4] M.-T. Jin, S.-Y. Xu, G.-M. Yang, and J. Su, "Yield of long-lived fission product transmutation using proton-, deuteron-, and alpha particle-induced spallation," *Nuclear Science and Techniques*, vol. 32, Sep. 2021. DOI: 10.1007/s41365-021-00933-8.

[5] *Implications of Partitioning and Transmutation in Radioactive Waste Management* (Technical Reports Series 435). Vienna: INTERNATIONAL ATOMIC ENERGY AGENCY, 2004, ISBN: 92-0-115104-7. URL: https://www.iaea.org/publications/7112/implications-of-partitioning-and-transmutation-in-radioactive-waste-management.

[6] W. S. Yang, Y. Kim, R. N. Hill, T. A. Taiwo, and H. S. Khalil, "Long-lived fission product transmutation studies," *Nuclear Science and Engineering*, vol. 146, no. 3, pp. 291–318, 2004. DOI: 10.13182/NSE04-A2411. URL: https://doi.org/10.13182/NSE04-A2411.

[7] A. Nassiri, B. Chase, P. Craievich, A. Fabris, H. Frischholz, J. Jacob, E. Jensen, M. Jensen, R. Kustom, and R. Pasquinelli, "History and technology developments of radio frequency (rf) systems for particle accelerators," *IEEE Transactions on Nuclear Science*, vol. 63, pp. 1–1, Nov. 2015. DOI: 10.1109/TNS.2015.2485164.

[8] Koning, Arjan, Hilaire, Stephane, and Goriely, Stephane, "Talys: Modeling of nuclear reactions," *Eur. Phys. J. A*, vol. 59, no. 6, p. 131, 2023. DOI: 10.1140/epja/s10050-023-01034-3. URL: https://doi.org/10.1140/epja/s10050-023-01034-3.

[9] A. Koning, D. Rochman, J.-C. Sublet, N. Dzysiuk, M. Fleming, and S. van der Marck, "Tendl: Complete nuclear data library for innovative nuclear science and technology," *Nuclear Data Sheets*, vol. 155, pp. 1–55, 2019, Special Issue on Nuclear Reaction Data, ISSN: 0090-3752. DOI: https://doi.org/10.1016/j.nds.2019.01.002. URL: https://www.sciencedirect.com/science/article/pii/S009037521930002X.

[10] J.-C. Sublet, I. Hill, A. Trkov, R. Forrest, B. Mustin, and A. J. Koning, "FISPACT-II: An advanced simulation and inventory code for nuclear research and waste management," *Nuclear Data Sheets*, vol. 148, pp. 305–310, 2018. DOI: 10.1016/j.nds.2018.02.022. URL: https://www.sciencedirect.com/science/article/pii/S0090375218301342.

[11] T. Sato, Y. Iwamoto, S. Hashimoto, *et al.*, "Features of particle and heavy ion transport code system (phits) version 3.02," *Journal of Nuclear Science and Technology*, vol. 55, no. 6, pp. 684–690, 2018. DOI: 10.1080/00223131.2017.1419890. URL: https://doi.org/10.1080/00223131.2017.1419890.

[12] J. F. Ziegler, J. P. Biersack, and M. D. Ziegler, "The stopping and range of ions in matter (srim) code," *Nuclear Instruments and Methods in Physics Research Section B: Beam Interactions with Materials and Atoms*, vol. 268, no. 11-12, pp. 1818–1823, 2010.

[13] A. Koning and J. Delaroche, "Local and global nucleon optical models from 1 kev to 200 mev," *Nuclear Physics A*, vol. 713, no. 3, pp. 231–310, 2003, ISSN: 0375-9474. DOI: https://doi.org/10.1016/S0375-9474(02)01321-0. URL: https://www.sciencedirect.com/science/article/pii/S0375947402013210.

[14] J. F. Ziegler, "Stopping of energetic light ions in elemental matter," *Journal of Applied Physics*, vol. 85, no. 3, pp. 1249–1272, Feb. 1999, ISSN: 0021-8979. DOI: 10.1063/1.369844. eprint: https://pubs.aip.org/aip/jap/article-pdf/85/3/1249/19113956/1249_1_online.pdf. URL: https://doi.org/10.1063/1.369844.

[15] H. Bateman, "The solution of a system of differential equations occurring in the theory of radio-active transformations," *Proc. Camb. Phil. Soc.*, vol. 16, p. 423, 1910.

[16] A. Koning, D. Rochman, J.-C. Sublet, N. Dzysiuk, M. Fleming, and S. van der Marck, "Tendl: Complete nuclear data library for innovative nuclear science and technology," *Nuclear Data Sheets*, vol. 155, pp. 1–55, 2019, Special Issue on Nuclear Reaction Data, ISSN: 0090-3752. DOI: https://doi.org/10.1016/j.nds.2019.01.002. URL: https://www.sciencedirect.com/science/article/pii/S009037521930002X.

[17] J. Yu, personal communication, 2023.

[18] A. Trkov and D. A. Brown, "Endf-6 formats manual: Data formats and procedures for the evaluated nuclear data files," Jan. 2018. DOI: 10.2172/1425114. URL: https://www.osti.gov/biblio/1425114.

[19] G. Tukharyan, personal communication, 2023.

[20] M. Fleming, J. Eastwood, T. Stainer, J.-C. David, and D. Mancusi, "Heir: A high-energy intra-nuclear cascade liège-based residual nuclear data library for simulation with fispact-ii," *Nuclear Instruments and Methods in Physics Research Section A: Accelerators, Spectrometers, Detectors and Associated Equipment*, vol. 908, pp. 291–297, 2018, ISSN: 0168-9002. DOI: https://doi.org/10.1016/j.nima.2018.06.065. URL: https://www.sciencedirect.com/science/article/pii/S0168900218307952.